Øyvind Auestad

The Boarding Control System

Modelling and Control of a Surface Effect Ship for improved accessibility to Offshore Wind Turbines

Thesis for the degree of philosophiae doctor
Trondheim, October 2015

Norwegian University of Science and Technology
Faculty of Information Technology, Mathematics and Electrical Engineering
Department of Engineering Cybernetics

NTNU
Innovation and Creativity

NTNU
Norwegian University of Science and Technology

Thesis for the degree of philosophiae doctor

Faculty of Information Technology, Mathematics and Electrical Engineering
Department of Engineering Cybernetics

© 2015 Øyvind Auestad.

ISBN 978-82-326-0992-5 (printed version)
ISBN 978-82-326-0993-2 (electronic version)
ISSN 1503-8181
ITK Report 2015-3-W

Doctoral theses at NTNU, 2015:168

Printed by Skipnes Kommunikasjon AS

To my dad Sigvald Auestad and my grandfather Jarl E. Fidje, for countless hours of help, support and arrangements in terms of theoretical and practical realization along the way of this project.

Summary

The main contribution of this thesis is to introduce a control system that enables access to offshore wind turbines for operation and maintenance (O&M) in higher sea states than what is possible today, while maintaining an acceptable level of risk. The system is implemented on-board on a Surface Effect Ship (SES) which introduces a new craft-concept to the turbine transfer vessels. Catamarans and Small-water-area twin hulls (SWATHs) are currently dominating the market.

The control system is denoted the Boarding Control System (BCS) which is a control algorithm that utilizes certain sensors and hardware to control air-flow actuators on a SES. The controlled actuators regulates the air cushion pressure to counteract, and compensate against, the vessel motions set up by sea wave propagations. Hence, we perform motion damping in the vertical plane which ultimately improves the accessibility to wind turbines.

The work presented in this thesis influenced the decision to build two vessels of the Wave Craft class, build no. 21 and 22 by Umoe Mandal. The prototype, Umoe Ventus, is currently operating at Borkum Riffgrund 1, a wind-farm in the German sector of the North Sea.

The SES-dynamics related to the BCS is mathematically modelled and a controller is designed. Stability investigations are performed and system performance are given through simulation, model- and full-scale experimental testing.

The performance of the BCS proves that accessibility to offshore-structures is possible in higher seas compared to the case where the system is inactive. Today it is possible to access turbines in up to 1.5 - 1.75m significant wave height (H_s). The SES with the BCS is tested in up to 2m H_s with no sign of reduced safety for offshore personnel while boarding a turbine. The model-test results indicates that access is possible in up to 2.5m H_s and at least 3.2m in long-crested seas (Section 2.5).

Contents

Summary **iii**

Contents **v**

List of figures **vii**

List of tables **ix**

Preface **xi**

1 Introduction **1**
- 1.1 Background and Motivation 2
- 1.2 The SES Concept 6
- 1.3 The SES History 9
- 1.4 Air Cushion Pressure Control 12
- 1.5 Model-testing 15

2 Journal and Conference Papers **23**
- 2.1 Conference Paper 1 25
- 2.2 Conference Paper 2 33
- 2.3 Conference Paper 3 41
- 2.4 Conference Paper 4 49
- 2.5 Journal Paper 49

3 Full-scale Experiments **69**
- 3.1 Classification of the Response of a Servo System - Inner Loop . . . 73
- 3.2 The Boarding Control System - Outer Loop 81

4 Conclusions and Recommendations for Future Work **85**
- 4.1 Conclusions 85
- 4.2 Future work 86

Appendices **89**

A Wave Craft Main Characteristics **91**

B Proof of Remark 1, in Conference Paper 3 (IFAC, World Congress) 93

References 95

List of figures

1.1 Wind farms currently online, under construction and consented (confirmed). Photo taken from [22]. . . . 2
1.2 Annual installed offshore wind capacity in Europe (MW). H1 refers to the first- while H2 denotes the second -half of the current year. Picture taken from [23]. . . . 3
1.3 The Nauti-Craft, picture taken from [3] 4
1.4 Boarding an offshore wind-turbine 4
1.5 Umoe Ventus, by courtesy of Umoe Mandal. 5
1.6 Umoe Ventus on the wind farm Borkum Riffgrund, by courtesy of Dong Energy. 5
1.7 The typically modern SES setup (illustration made by UM). 7
1.8 Hullborne. 8
1.9 Cushionborne. 8
1.10 The U.S. Navy's XR-3. 9
1.11 The SES-100A and SES-100B 10
1.12 The SES 200 11
1.13 The Cirrus series 11
1.14 The Skjold class 12
1.15 The first generation of the RCS Control Unit. Picture is taken from [16]. 13
1.16 RCS performance 13
1.17 Heave accelerations for SES-200 per $1/3$ octave band in low sea state II. Picture taken from [16]. 14
1.18 Signal processing of the sensor signal before entering state space as velocity. f_c denotes the cut-off frequency. 15
1.19 The scaled hull. 16
1.20 The scaled flexible seals. 16
1.21 The location of certain instrumentation. Picture taken in the Ship Model Tank, Sintef Marintek. 17
1.22 Resistance and drag tests in calm water performed in the Ship Model Tank. 18
1.23 Bow and stern seal - seen from the air cushion. 19
1.24 Complete model-test equipment. 20
1.25 Model-test action. 20
1.26 Lift fan test setup. Test performed at Umoe Mandal. 21
1.27 Lift Fan Characteristics 22

3.1 A computer model of Umoe Ventus shown from the side, by courtesy of Umoe Mandal. 70
3.2 The Wave Craft prototype seen from the front. The bow skirt is visible. Photo: Umoe Mandal. 70
3.3 Inner and outer loop control system. 71
3.4 A block diagram of the inner and outer loop system 72
3.5 Test overview. 74
3.6 Vent valve assembly. 74
3.7 Direction of the hydraulic flow. 75
3.8 Feedback system in the frequency domain. 75
3.9 A step response is commanded on the input. 77
3.10 Vent Valve frequency-sweep test 78
3.11 Figure 3.10 zoomed in at the end. 79
3.12 Bode Plot - illustrates the frequency response from the input (Command Pos.) to the output (Measured Pos.). 79
3.13 Valve Command and error signal. 80
3.14 Umoe Ventus in operation 81
3.15 Time series plot of the bow acceleration. The BCS is initially on and turned off at $t = 290$s. 82
3.16 PSD plot of the bow acceleration with, and without, the BCS active. . 82
3.17 Time series with and without ($t = \{53, 1356\}$s) the BCS active. . . . 83
3.18 Bow acceleration PSD plot with, and without, the BCS active. 84
3.19 CG acceleration PSD plot with, and without, the BCS active. 84

A.1 One-pager - UM Wave Craft 92

List of tables

1.1 Model-test instrumentation 17

2.1 Article overview 24

3.1 Inner loop notation 75

Preface

This thesis is submitted in partial fulfilment of the requirements for the degree of philosophiae doctor (PhD) at the Norwegian University of Science and Technology (NTNU).

My supervisors have been Professor Jan Tommy Gravdahl (Department of Engineering Cybernetics, NTNU), Professor Asgeir Johan Sørensen (AMOS, NTNU) and civil engineer Trygve Halvorsen Espeland (Umoe Mandal).

My research position was funded by *Umoe Mandal* (UM) and the *Research Council of Norway under the arrangement of an Industrial Ph.D. scheme (ES488888)* and partly by the Centres of Excellence funding scheme, project number 223254 - *AMOS*. I have been an employee of Umoe Mandal during the candidate period. The bench-test, model-tests and part of the full-scale instrumentation was sponsored by *Regionale forskningsfond Agder*, *The Norwegian Research Council under the MAROFF program* and *Carbon Trust's Offshore Wind Accelerator (OWA) Access Competition*. The OWA is one-third funded by the *UK department of Energy and Climate Change* and two-third funded by commercial partners which includes *Dong Energy, e-on, Mainstream Renewable Power, RWE, Scottishpower Renewable, SSE Renewable, Statkraft, Statoil* and *Vattenfall*.

All model-tests were conducted in Trondheim, Norway, either in the Marine Cybernetics Lab (AMOS, NTNU) or the Ship Model Tank (Marintek, SINTEF).

During my Ph.D. studies I worked with Professor Thor Inge Fossen and Professor Tristan Perez which led to two conferences- and one journal -paper. I worked with Bill McFann and Tim Pannone from Island Engineering which supplies the full-scale Wave Craft with control system hardware and software. For several months I worked at Marintek (SINTEF/NTNU) while building, developing and testing the model-test craft that will be introduced later. RG-seasight sponsored the model-test craft with a scaled bow fender.

Acknowledgments

I would like to thank my girlfriend and family: Line, Linn, Grete, Sigvald, Rigmor, Jarl, Inghild and Martin. A great thank you is handed out to all of my friends and colleges both at the Department of Engineering Cybernetics and at Umoe Mandal! Thanks to Umoe Consulting for providing me an office in Oslo.

A special greeting goes out to Trygve H. Espeland for all support and help both technical and non-technical. This thesis would not exist without your willingness, innovative, arrangement skills! A special thank also goes out to Jan Gunnar Røyland for his impressive expertise within hydraulics, electrics, instrumentation and actuators and for always taking the time to help out, even in very hectic times.

I would like to thank Bill McFann and Tim Pannone in Island Engineering for the endless: work-hours, email conversations, jokes and phone calls which all have proven to be necessary in order to set up the integrated, comprehensive motion control system on the Wave Craft. I hope you guys seek comfort in Tim's continually fund-increasing, offshore bank account. Working close with you on practical matters, using control system theory, have certainly triggered the motivation to continue working with marine control systems. Also, thank you for your great hospitality in Piney Point, for sharing data and information.

A major part of the candidate period took place at Tyholt Marintek, Trondheim when building, arranging and testing the model test craft. I would like to thank the nice people at the Sintef and NTNU division and particular Egil Jullumstrø and Torgeir Wahl for great hospitality and technical support. Thanks to Dong Energy and the Umoe Ventus captains from Valling Ship Management for good times in Norddeich and at Borkum Riffgrund 1.

I would like to thank my supervisor Prof. Jan Tommy Gravdahl for his experience and expertise within automatic control systems and for all the great hangouts we have had on our conference trips. I am also grateful and privileged to get the opportunity to have AMOS director and prof. Asgeir Johan Sørensen as co-supervisor with his contribution to ride control systems on a SES and ship motion control systems in general. Thank you Prof. Tristan Perez for your great contribution on the journal paper on bow-to-turbine modelling. The same goes to Per Sondre Sodeland for co-developing and implementing this model in Simulink, I am looking forward to continue our work as your co-supervisor!

Chapter 1

Introduction

> We are convinced that new innovative solutions, like Wave Craft will provide significant cost savings to the offshore wind industry and we are delighted to see another of the Offshore Wind Accelerator supported concepts reach the market.
>
> Jan Matthiesen, Director Innovation at the Carbon Trust

> There are no other specialized service vessels for wind turbines that can sail at such high speed with good comfort for technicians as the Wave Craft. Safe transit and access in higher sea-states is important for us in order to optimise turbine availability and electricity production. Improved access to wind farms in harsher areas and further offshore can defend a higher vessel cost.
>
> Anders Wikborg, Marine Operations Manager, Offshore Wind Energy, Statoil

> The future does not belong to the largest or the strongest, but those who can adapt quickest.
>
> Jens Ulltveit-Moe, owner of Umoe Mandal and Umoe Wind

Chapter 2 include conference papers and a journal article written during the period of the Ph.D. studies. The remaining part, Chapter 1, 3 and 4 is written to enrich and supplement the articles while trying to repeat as little as possible. The exception is the inevitably description of the SES concept which is described in each article.

1.1 Background and Motivation

The wind farm service Surface Effect Ship (SES) concept, referred to as the Wave Craft project, was initiated by Trygve H. Espeland at Umoe Mandal in 2010/2011 as a spin-off from another SES concept, the T-Craft [21] [13]. The Wave Craft is a Crew Transfer Vessel (CTV). The author of this thesis joined the development during the summer of 2011 to explore the potential of vertical motion damping by manipulation of the air cushion pressure. This evolved into a master thesis ([6]) which again led to the work covered in this Ph.D. thesis. The control system that performs vertical motion damping, or reduction, is referred to as the Boarding Control System (BCS).

The Carbon Trust is an independent company for contributing to a more sustainable future through carbon reduction. The Offshore Wind Accelerator (OWA) [4] is a joint industry project involving nine offshore wind developers including the four largest (Dong Energy, Vattenfall, e-on and RWE) [22]. The OWA is Carbon Trust's flagship collaborative Research, Development and Demonstration programme. This program supports and helps commercialising innovative solutions and aims to reduce offshore wind costs by 10%. To do so, the OWA announced in 2010, a turbine access competition, aimed to identify and develop new access systems to dramatically improve the availability of turbines and the safety of people during the transfer to turbines. The turbines were assumed accessible in up to 1.5m significant wave height (H_s) [2]. The Wave Craft with the BCS was one of the winners of this competition. The reason for this is that the BCS reduce vessel motions so that turbine access is possible in up to 2.5m H_s hence the possible annual access days are increased, leading to increased turbine uptime which again results in decreased offshore wind costs.

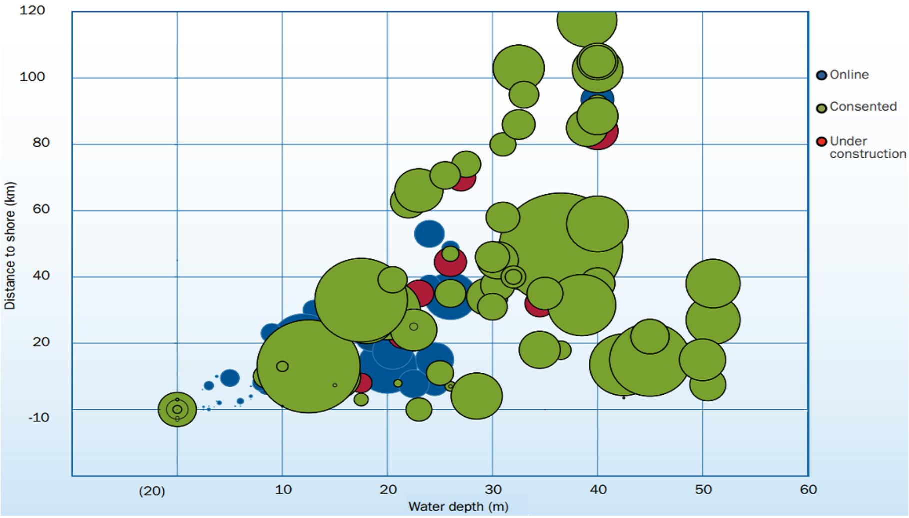

Figure 1.1: Wind farms currently online, under construction and consented (confirmed). Photo taken from [22].

Figure 1.1, taken from a report written by the European Wind Energy Association [22], indicates that the wind farms of tomorrow are located further from shore and into deeper waters. As a result, an increased wind farm transit distance and higher sea states are two direct consequences of this. Traditionally, the SES is known to offer very high speed with high comfort in various sea states. The Wave Craft with the BCS can potentially solve the turbine access requirement for tomorrows turbine without resorting to aids such as helicopters. It is revealed in [22] that at the end of 2014 the average distance to shore was 32.9 km, compared to 3.3 km in 2000.

Europe is the dominant world leader in offshore wind power. Figure 1.2 proves that the annual installed offshore wind capacity is significantly increasing.

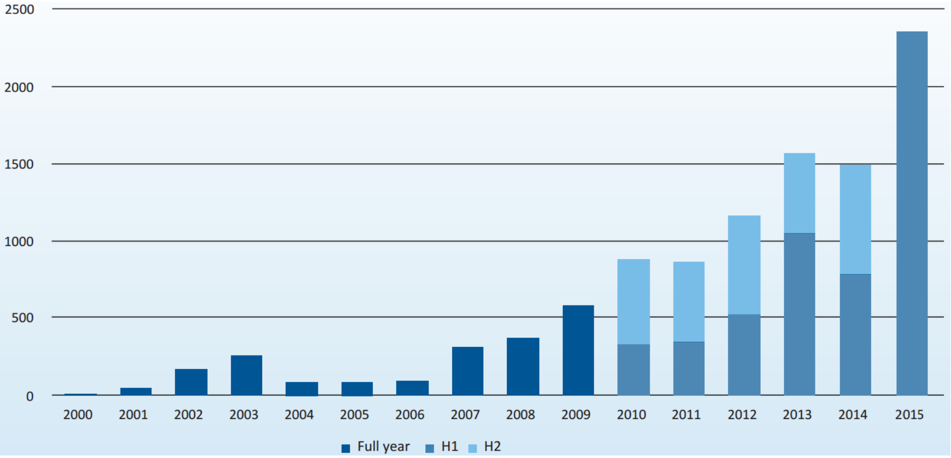

Figure 1.2: Annual installed offshore wind capacity in Europe (MW). H1 refers to the first- while H2 denotes the second -half of the current year. Picture taken from [23].

Operation and maintenance (O&M) costs constitute a sizeable share, around 20-30%, of total annual costs of an offshore wind farm [32]. In fact, the two most important issues to be addressed for good economics are minimisation of maintenance requirements and maximisation of access feasibility. A study indicates that as much as 47% of average downtime is due to high sea conditions [38] denying conventional CTVs to access the turbines.

Several other innovative access design are currently under development [3] such as the hull design of Fjellstrand's Windserver. The design results in a motion stable and fuel-efficient vessel. The Nauti-Craft is a another new vessel design where the hulls are separated from the deck (and superstructure) via a 'passive reactive' hydraulic suspension system. This system allows the hulls to stick to the ocean surface while the rest of the vessel compensates against the sea waves, see figure 1.3.

Also, several modular transfer system that can be placed on an arbitrary CTV are under development and testing. These designs are essentially motion compensated gangways and include Otso Ltd's Autobrow, BMT & Houlder Turbine Access System (TAS) Mark II, Momac Offshore Transfer System (MOTS) and Knude Hansen's Wind Bridge [3].

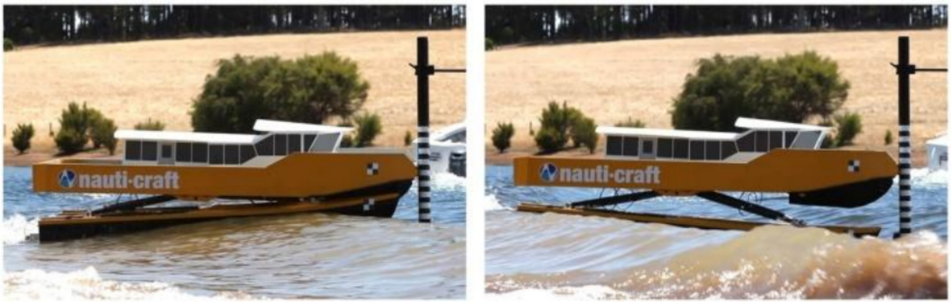

Figure 1.3: The Nauti-Craft, picture taken from [3]

Another motivating factor behind the work covered in this thesis, is that the BCS on a SES is not exclusively restricted to deal with wind farm docking but it is in fact relevant for all offshore applications where the following are key factors:

- Safe transfer of personnel and equipment to and from an offshore station.
- Reduction of vertical motion at the wave frequency in zero, or low, speeds, such as reducing sea-sickness incidents.

These items applies for installation, transport and O&M. As a side note, this work would not mind brushing some dust off the SES concept which had quite an upswing during the seventies and throughout the early nineties.

During the end of the Ph.d. studies, and as a consequence of it, the Wave Craft prototype as seen in Figs. 1.4, 1.5 and 1.6, was constructed by Umoe Mandal, sold to Umoe Wind and chartered to Dong Energy in March, 2015. The prototype Umoe Ventus, is currently acting as a CTV on the wind farm *Borkum Riffgrund 1*. The wind farm consists of 78 turbines and provides 320,000 German households with renewable power.

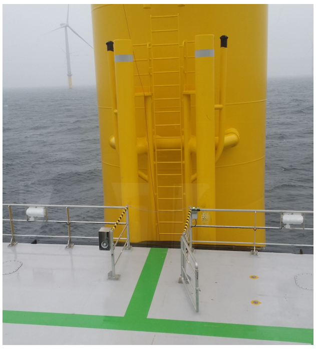

Figure 1.4: Boarding an offshore wind-turbine, by courtesy of Umoe Mandal.

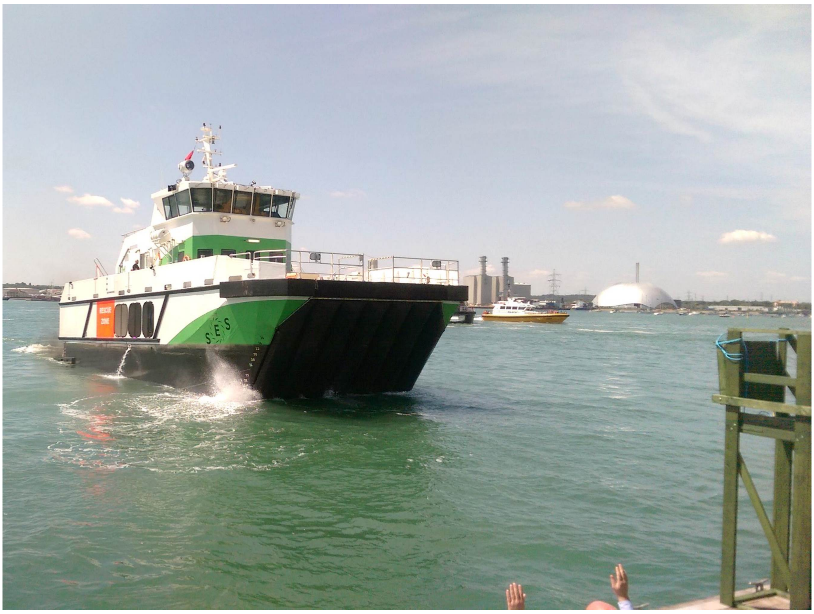

Figure 1.5: Umoe Ventus, by courtesy of Umoe Mandal.

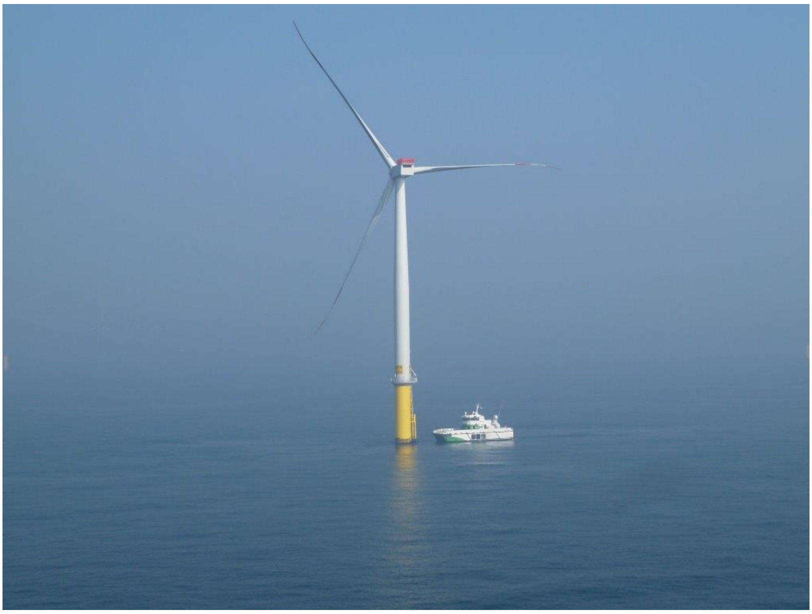

Figure 1.6: Umoe Ventus on the wind farm Borkum Riffgrund, by courtesy of Dong Energy.

1.1.1 Research objective and paper content

The overall objective of this thesis is to control the air cushion pressure so that turbine access is possible in high waves.

The first step towards such a task is to understand the physics and the response of the air cushion coupled with vessel motions. Section 2.1 presents the first paper in this thesis, which describes a mathematical, non-linear process plant model of a free floating SES with a controller that reduces vertical bow motion. Simulation results are presented.

A SES experience some vibrations in the hull due to the air cushion dynamics. Therefore, any sensor mounted on the hull needs proper signal processing before it is sent to an actuator. The control objective consist of reducing vertical motion, therefore it is desired to have vertical acceleration, velocity and position available in the control law. The paper presented in Section 2.2 estimates heave velocity and heave position based on sensor readings from an inertial measurement unit (IMU) on a SES. Heave motion is estimated using a real-time fast fourier transform (FFT), peak detection of the FFT, an observer and motion transformation principles.

The paper in Section 2.3 also deals with a free floating SES. A linear control plant model is presented with a controller that guarantees Global Exponential Stability for the closed-loop state space system. The performance of the controller is given through model test results showing reduced bow motions.

Section 2.4 and 2.5 present a journal paper with mathematical modelling of a SES towards a wind turbine. A controller is presented to increase accessibility to the turbine. The performance is given through simulation and experimental testing on a model-scale and a full-scale vessel.

1.2 The SES Concept

This section includes literature mainly gathered from Butler [16], Faltinsen [24] and Kaplan et al. [27]. The former two citations also presents mathematical modelling of a SES.

The SES rides on a pressurized air cushion enclosed by side-hulls and flexible seals. The cushion can lift up to 80% of the vessel mass using lift fans and stern bag boost fans. The lift fan blows air into the air cushion and pressurizes it. The stern bag boost fan ensures that air does not leak under the stern seal bag. A study on the dynamics of the seals are given in [19] and [31]. There exist two extreme modes of SES operation: cushionborne with maximum lift-ratio and hullborne with zero lift-ratio and zero air cushion (excess) pressure. The lift ratio can be changed as desired according to what is beneficial for the current situation. For instance, the BCS operates in the middle of these two modes, hence in 'partly cushionborne' configuration. In general, it only takes seconds to change between different operational modes. A typical, modern SES is shown in Fig. 1.7.

Before studying the two typical SES modes, some general notes are given. The SES lift ratio is very sensitive to weight and trim in order to achieve low drag force and low fuel consumption. A correct trim angle is important for bypassing the hump speed and entering the high-speed regime. The hump speeds of a vessel occur when the water resistance reaches local maximums. On a SES, the air cushion

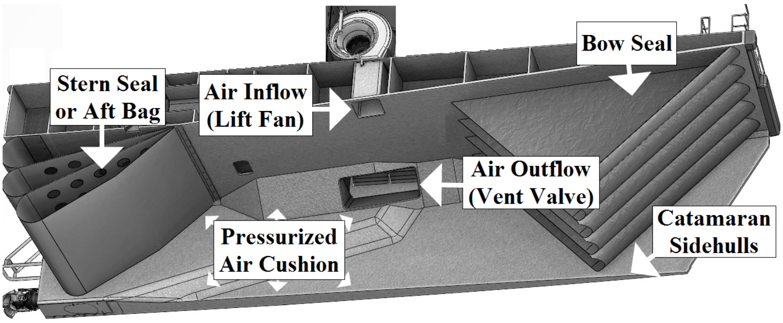

Figure 1.7: The typically modern SES setup (illustration made by UM).

pressure also introduces a drag force. Very high air cushion pressure in slow speeds is usually a bad idea. Therefore one must consider the air cushion pressure versus speed when successfully operating a SES. When a SES manages to bypass the hump speed, positive acceleration and a corresponding "jump" in forward velocity is immediately observed. When the hump is passed, the maximum speed is achieved when the air cushion pressure is maximized.

Other important factors of the SES that the designers of the vessel must carefully consider are the air cushion length to breadth (l/b) ratio, the desired top speed, the seal geometry, the propulsion properties and the suitable location of the center of gravity versus the location of the center of pressure. These key factors play a crucial role in terms of the stability and the performance of the vessel.
Typical drawbacks of the SES include an increased price tag, typically 25% more than an equivalent catamaran. This is mainly due to air flow actuators, mechanics and seals. The bottom of the bow finger seals (Fig. 1.7) experience vibrations, or flagellations, up to 50-150 Hz during head sea-, high-speed-, cushionbourne -operation. The wear and tear of the seals limit the operational life and in some cases, the life length is less than the vessel's drydock cycle. However, offshore seal-replacement is possible given a suitable mounting design.

The off-cushion (Fig. 1.8) and on-cushion (Fig. 1.9) modes are shown and characterized on the next page.

Off-cushion / hullborne:

- The lift fans and the bag fan are turned OFF which enables SWATH- or catamaran-mode.
- Full displacement side-hulls.
- Fuel efficient at low speeds.
- The bow and stern seals ensure that the cushion volume acts as a passive motion-damping accumulator that significantly reduces motions in large seas (also effective during partly cushionborne) [16].
- The side-hulls design can be optimized for low-speed resistance, in contrast to most mono-hulls whose shape must compromise drag force for low and moderate speeds.

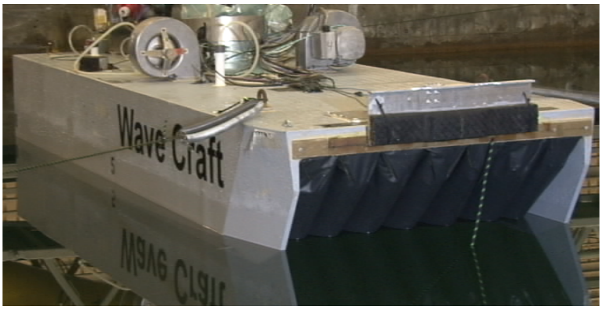

Figure 1.8: Hullborne.

On-cushion / cushionborne:

- Lift fans and bag fan are turned ON and the vent valves are closed.
- The air cushion is pressurized which support the majority of the weight.
- The natural heave and roll periods are shorter compared to an equivalent catamaran.

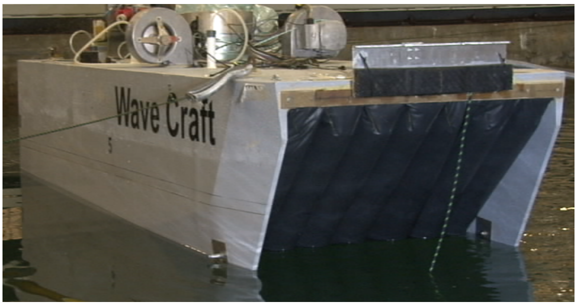

Figure 1.9: Cushionborne.

- The pressurized air-cushion lifts the major part of the hull out of the water which leads to:
  - ✓ Low drag force and very high speeds, up to 100 knots.
  - ✓ The small draft permits sailing in shallow water.
  - ✓ Decreased damage effect by underwater explosions and therefore ideal as a minehunter/minsesweeper, such as the Norwegian Armed forces MCMV Oksøy class or the former U.S. Navy's MSH.
  - ✓ Lower chance of sea waves hitting the water-deck (slamming).
  - ✓ Excellent stability and seakeeping abilities in all seas since the air cushion acts as a mass-spring-damper system both in the passive and actively controlled configuration. [16].
- The air flow out of the vent valves, when directed in the transverse direction, can be used as side-thrusters. This has been successfully proven on the Oksøy MCMV class and a vent valve DP system is currently under development [36].

1.3 The SES History

This and the following section are based on some central SES articles written by Butler [16], Lavis and Spaulding [29], Lavis [28], Chaplin [17] and Clark et al. [18]. Also, verbal conversations with Mr. Bill McFann are used who also acts as a reviewer in these two sections.

There have been constructed over 50 different modern SES prototypes and most of them lead to a series production. In Scotland, 1961, William Denny & Brothers launched the first commercial SES, the D1. The vessel had a maximum speed of 17.6 knots, was built of out wood and had a l/b ratio of 7. Denny launched its successor one year later, the D2, which did 34 knots and was the first SES passenger ferry.

Meanwhile in the U.S., Mr. Allen Ford and his team designed the first military SES, the XR-1. The construction phase started in 1960 and it was launched two years later at the Naval Air Experimental Center for the U.S. Navy. The craft had 4 x 40 000 hp gas-turbine engines driving water jet propulsion which lead to a top speed of 80 knots, measured in the Delaware River in 1964. Dr. Harvey R. Chaplin brought Mr. Ford to the David Taylor Naval Ship Research and Development Center in 1965 which led to a series of manned SES crafts. Ford's SES division consisted of Mr. Stephen Chorney on *Stability and Maneuverability*, Mr. William Richardson on *Structures and Materials*, Mr. John Adams of Maritime Dynamics on *Seakeeping* while *Propulsion* was covered by Mr. Robert Etter.

The historical evolution can best be divided into three periods. The first phase included the XR-1 with its first two successors (the XR-2 and the XR-3), the SES 100A and the SES 100B.

The XR-3, as seen in Fig. 1.10, was launched in 1967 at the David Taylor Model Basing in Maryland. Bill Harry and Marty Fink both acted as development engineers and test-pilots. After serving in a test program on the Severn River, Maryland, the craft was used for training at the U.S. Navy Post graduate school in Monterey.

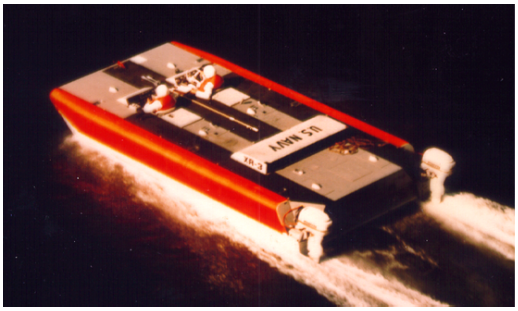

Figure 1.10: The U.S. Navy's XR-3.

In 1969, the U.S. Navy awarded separate contracts to Aerojet General and Bell Aerospace Textron for designing and building the SES-100A and the SES-100B. These two vessels weighed around 100-ton, are approximately 24m long and are shown in Fig. 1.11. The SES 100A was equipped with steerable water jets and a propulsion and lift fan engine (4-TF 35GT) with 15 000hp. The SES 100B was equipped with approximately same engine power but had twin super-cav rudders as propulsion system.

These first phase vessels served as design crafts for developing the U.S. Navy's 3K SES program. The goal of this program was to construct a 3000-ton, 80-90 knot craft. The program ran over 14 years, included a price-tag exceeding $500 million with hundreds of contractors, consultancies and universities involved. The 3K SES was never realised due to a political decision in 1979, most likely due to the national oil crisis. This was three weeks prior to the start-up of the hull construction. However, these prototypes which were characterized by a low length-to-beam ratios (l/b = 2) and relatively thin side-hulls, proved impressive performance. The SES-100B did a speed record of 93.4 knots in flat seas and it did 35 knots in 1.8-2.4m waves. The developed SES design proved to be a great success and was adopted several years later for industrial passenger-ferries. The literary footprints from this era served, and still serves, as a design base for new prototypes.

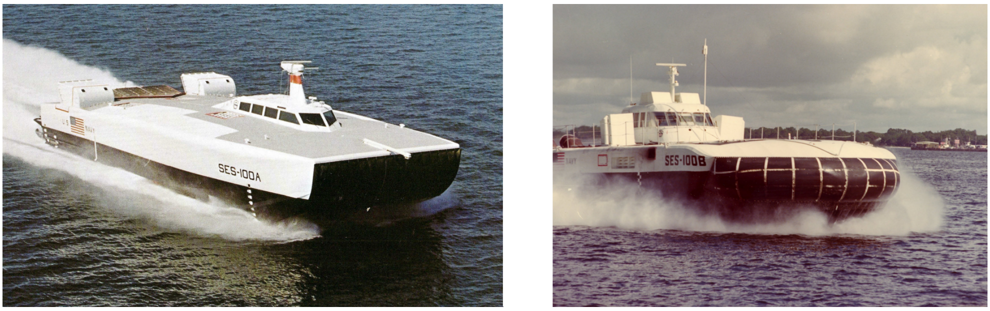

Figure 1.11: The SES-100A (131 ton) and SES-100B (93.4 ton), from left to right. Top speed: 80 and 94 knots, respectively.

The second generation of SES, such as the U.S. Navy XR-5, had high l/b ratio which favour efficiency in terms of fuel and costs due to a low-speed drag characteristic. The private marked in Russia also built some high ratio l/b SES which did 25-knots and acted as river transport "buses".

The third generation enabled the SES to not just operate efficiently during cushionborne and high speeds, but also in hullborne and low speeds. The XR-5A, BH-110 and SES-200 initiated this generation and had modified catamaran sidehulls to provide extra buoyancy. The SES had now an overall high efficiency as it could sail as a true a catamaran in low speeds and switch to cushionborne mode to obtain high speeds.

In 1985, when Butler's paper [16] was published, the state of the art was the U.S. Navy MSH which was a minesweeper with a high l/b ratio. The craft utilized the low submergence to reduce the effect of underwater explosions (Fig. 1.12). The hull experienced 60 to 80% less shock than a monohull.

Several passenger ferries were built during the 80s and early 90s, and these years served as the big commercial SES-era. The SES ferries were popular since they offered great comfort and minimized the transfer time due to their high speed. Some of these ferries included the Cirrus series built by Brødrene Aa, Eikefjord

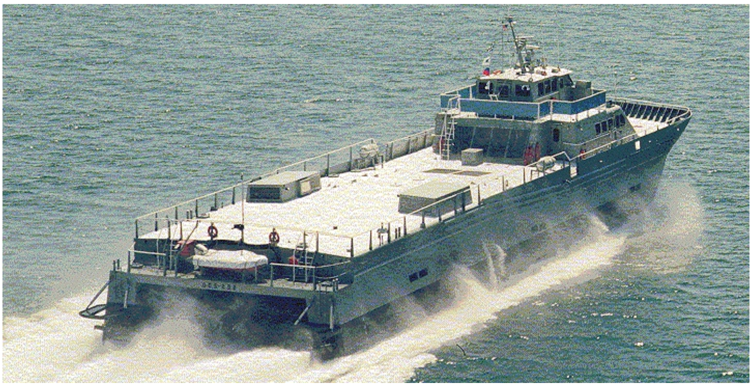

Figure 1.12: The SES 200 had a range of 3000 miles at 25-30 knots without having to refuel.

Marine and Ulstein group. Figure 1.13 shows three of these crafts.

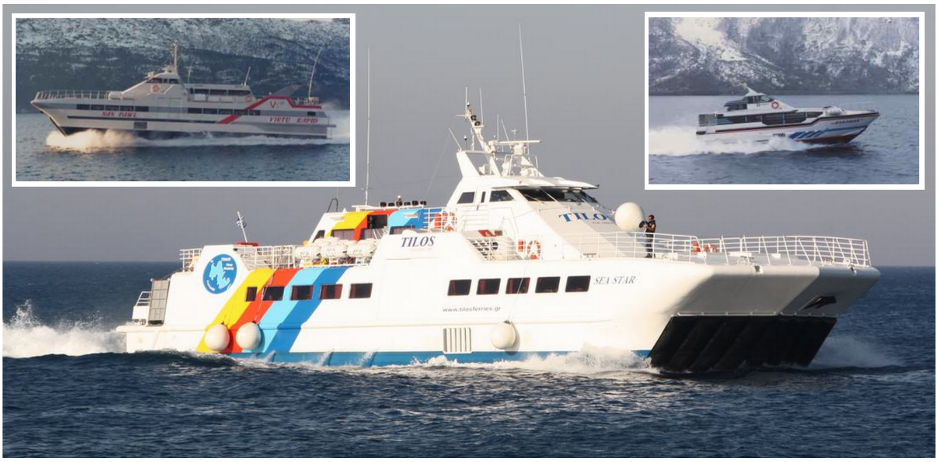

Figure 1.13: The Cirrus series, from left to right, San Pawl, Sea Star (Nissho) and Harpoon. The Sea Star is still operating today. Photo: Refvik and Island Engineering.

From the mid 90s and up to this date, Umoe Mandal is currently the only shipyard that launch operational SES. Four minehunters and five minesweepers were delivered during 1994-1997. In 1999 the motor torpedo boat Skjold (Fig. 1.14) was delivered followed by a series of five with the last craft delivered in 2012. The Wave Craft prototype, delivered early in 2015, introduced the yard to the civil marked.

Figure 1.14: The Skjold class, maximum speed of 60 knots+ and overall extreme performance, by courtesy of UM.

1.4 Air Cushion Pressure Control

The air cushion pressure control during transit is referred to as the Ride Control System (RCS) and aims at reducing wave-induced pressure fluctuations in the cushion and, hence, the vertical motion of the vessel.

An un-stabilized SES vessel will 'bounce' at its natural spring mass damper frequency [27], and also can excite its various acoustic modes [34]. Various opinions call these collectively the 'cobblestone effect' - Bill McFann (Island Engineering, former Maritime Dynamics).

The cobblestone effect [37], [35] is traditionally dealt with using cushion pressure feedback control. The RCS consists of a number of electrical, hydraulic, and mechanical parts and constitutes the SES systems together with the bag fan, lift fans, the fore- and stern seal.

There are several ways of (indirectly) controlling the air cushion pressure. The most commonly used air-flow-actuator is the vent valve. Each vent valve assembly is fitted with a number of vanes, also called louvers that can rotate around their own centerline. The rotation results in changes of cushion pressure by venting the air cushion to ambient air. The (rotating) position of the louvers are maintained by hydraulic servos. The servos are fed with a position command which is the output of the RCS, or the BCS control law. To be noted, the BCS presented in this thesis utilizes the same physical vent valves used for the RCS during transit; however the control law and sensor input differ.

Other strategies for controlling the air cushion pressure includes the fan blade angle control scheme. This scheme deals with automatic control of the pitch angle of the lift fan blades. During fan operation, this controls the air flow out of the fan. Another approach is to control the inlet or outlet area of the lift fan which works well for centrifugal lift fans. This can be done by installing a set of controllable louvers that controls either the inlet or the outlet area of the fan. In fact, the Wave Craft possess such a variable area scheme in the duct between the fan outlet and the air cushion. This control strategy is not further discussed. Another successfully verified approach is to control the position of a cone in and out of the fan (inlet) impeller house. When the cone is located inside the impeller house, the fan is choked or throttled, but when the cone is positioned outside the impeller house, maximum air flow out from the fan is achieved.

The RCS have been successfully demonstrated on small and large SES. It is an integrated part of the SES and are used full time during cushionborne transit operations as it significantly increases ride comfort. The first functional RCS, with a satisfactory performance, were implemented on the first SES generations by Maritime Dynamics, now NAIAD Dynamics (see Fig. 1.15).

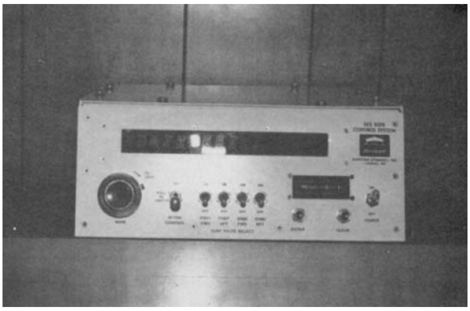

Figure 1.15: The first generation of the RCS Control Unit. Picture is taken from [16].

There are several ways of indicating the performance of the RCS. The most intuitive approach is to use time series as seen in Fig. 1.16.

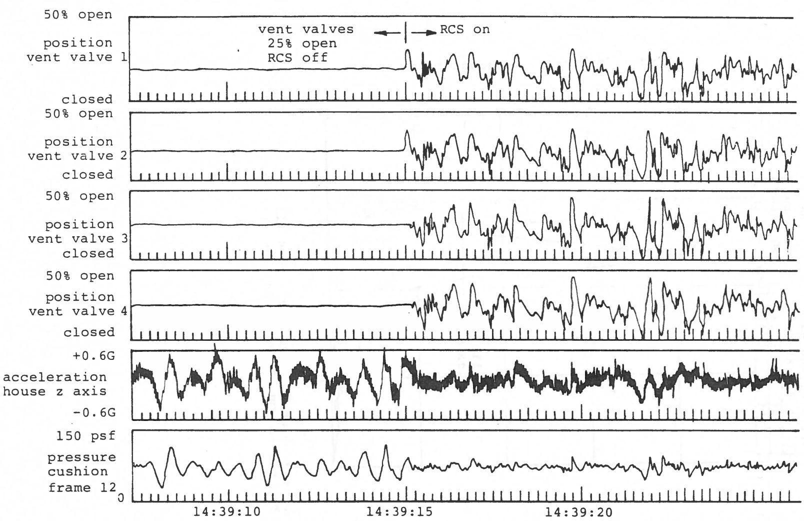

Figure 1.16: RCS turned ON at 14:39:15. Head sea, 3ft waves, 100-ton craft (SES-100A or SES-100B) in 35 knots. Picture taken from [26].

Figure 1.17 illustrates the more traditional approach in order to investigate RCS performance. The figure shows heave acceleration as a function of frequency at the passengers cabin, plotted in a 1/3rd octave band format for RCS on and off together with the acceleration limits given in ISO-2631-1:1997 [1]. ISO-2631 present certain upper bound acceleration limits, as a function of exposure time and incident wave frequency. Thus, if the experienced accelerations are lower than the ISO-limit: sea-sickness and human-fatigue are not likely to occur in the current sea-state.

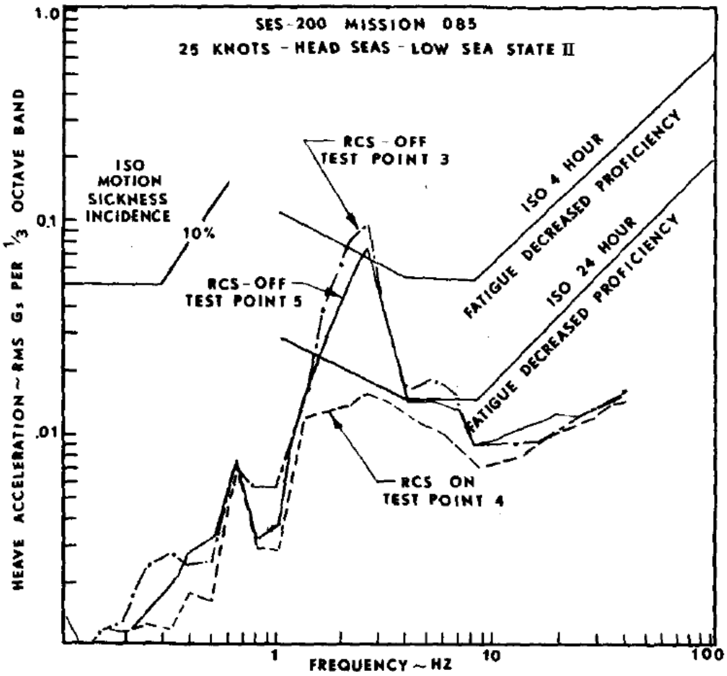

Figure 1.17: Heave accelerations for SES-200 per 1/3 octave band in low sea state II. Picture taken from [16].

The most important literary contributions on RCS are discussed further in Section 2.5 and include articles written by Kaplan et al. [27], Adams et al. [5], Sørensen and Egeland [34] and Bertin et al. [14].

Similar to the BCS, Basturk and Krstic [13] focus on damping wave induced motion in low-speeds where they are reducing the motion of a ramp between a SES and a large, medium-speed, roll-on roll-off (LMSR) vessel. Also, Sodeland [36] investigated the potential of combining dynamic position and vertical motion damping on a SES. The combined controller uses optimal control to reduce vertical motion (based on the BCS) while simultaneously minimizing sway motion. This is done by directing the pressurized air-cushion air-flow out through starboard and/or port vent valves. Utilizing the vent valves as a thruster in sway has successfully been proven on the MCMV Oksøy class, but only with a fixed vent valve leakage configuration where the cushion leakage is either directed through starboard or port side vent valve duct.

1.5 Model-testing

Constructing and testing of the vessel model, lead to a deeper and practical understanding of the SES. Three different craft models were built, each with a slightly different hull and seal geometry design for optimizing the overall performance. Over 350 unique test-runs were performed during the comprehensive model test phase.

1.5.1 Signal processing

The articles presented in Chapter 2 include several model-test data figures which indicates the performance of the automatic control system. The raw accelerometer sensor signal needs processing before entering state space as velocity ($y(t)$). This signal processing is illustrated in Fig. 1.18. The high-pass filter removes potential sensor signal drift while the low-pass filter performs signal smoothing. The two filters combined with proper parameter handling, represent a band-pass filter which defines the controller bandwidth. The next filter is a numerical integrator which transfers the signal from acceleration to velocity, which is shown stable in our closed loop system given in Section 2.5. The control system was written in Simulink, compiled to C and uploaded to a Can-bus PLS node. The applied numerical integrator is taken from the Simulink standard library.

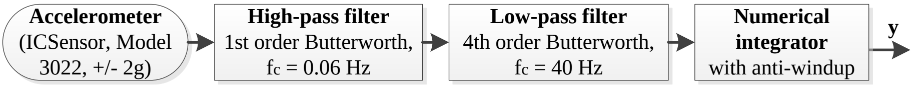

Figure 1.18: Signal processing of the sensor signal before entering state space as velocity. f_c denotes the cut-off frequency.

1.5.2 Construction and test-setup

The shape of the hull was designed as a 3D-model and cut-out, using a cutting-robot, from a square box of divinycell. A layer of plastic (fiber/resin) was applied utmost to reinforce the hull form. Finally, the wetdeck cut-outs were made for the lift fans, vent valve and pressure sensor assembly. See Fig. 1.19 taken at Umoe Mandal together with UM personnel Knut Aamodt on the left side.

Figure 1.20 illustrates the third set of the flexible seals, including seven finger seals and one three-loop aft bag. The design and suspension of the model-test bow seal was designed, cut and sewed by Jarl Egil Fidje and the thesis's author. Mounting help given by Sigvald Auestad.

Table 1.1 lists the instrumentation used on the model-test craft. Figure 1.21 indicate the location of some of them. The bow rubber fender and the turbine column can be seen in the front of the vessel.

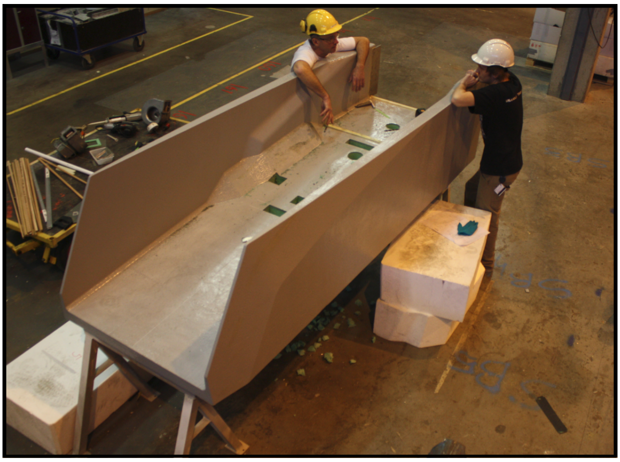

Figure 1.19: The scaled hull.

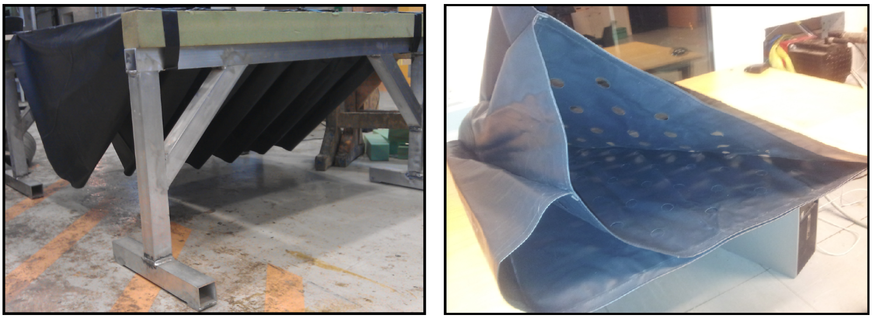

Figure 1.20: The scaled flexible seals.

Table 1.1: Model-test instrumentation

#	**Type**	**Function**
3	Gauge pressure sensor (Measurement Specialities, MS1451)	Two in the cushion and one in the aft bag.
2	Load cells (Lozosc, LPL7161-A)	Measure horizontal and vertical bow fender forces. Unsuccessfully tried as control system input signal.
2	Accelerometers (ICSensor, 3022, +/− 2g)	Monitoring and control system input signal.
1	6-DOF Position Device (Qualisys, Oqus 3+)	Monitoring and measure motions in 6-DOF in real-time.
1	Wave generator (AWACS, DHI)	Generates regular and irregular waves.
2	Lift fans	Pressurize the air cushion.
1	Bag fan	Pressurize the aft bag.
1	Servo motor	Actuator for the vent valve.
1	Core controller (any computer)	Runs the control law.
1	Can-bus node	Servo PLS for inner-loop vent valve control for converging commanded and actual vent valve position.
2	Cameras	Real-time video of the bow and stern seal seen from the wet-deck.

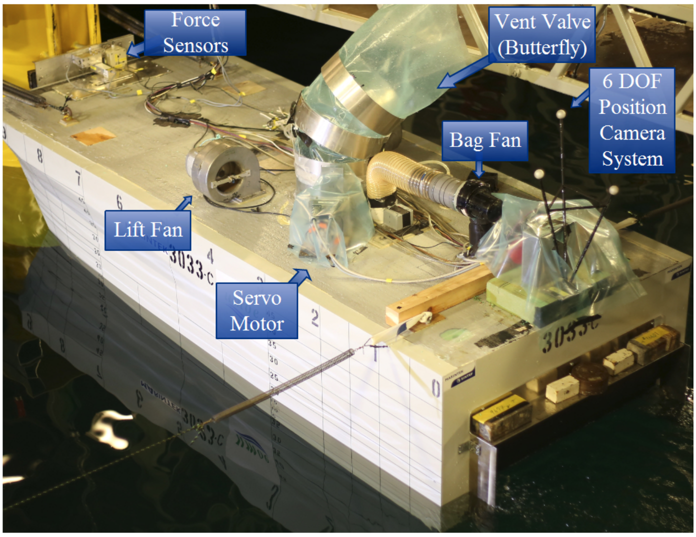

Figure 1.21: The location of certain instrumentation. Picture taken in the Ship Model Tank, Sintef Marintek.

Resistance and drag tests were performed in the Ship Model Tank, Marintek. The upper photo in Fig. 1.22, with colleague Christian Fagereng, indicate the scale of the craft while the lower photo shows a 45 knot, calm water run. The low draft minimizes the hull-area exposed to hydrostatic drag forces while submerging the water jets.

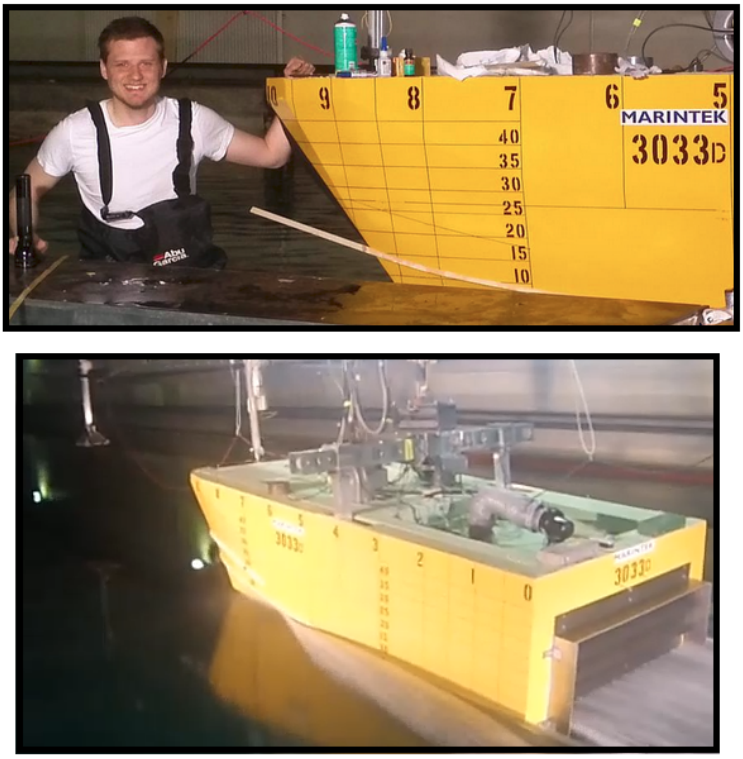

Figure 1.22: Resistance and drag tests in calm water performed in the Ship Model Tank.

Figure 1.23 shows the air cushion during boarding mode. The photos are taken with two cameras mounted on the wet-deck for monitoring purposes. The real-time video played a crucial role when deciding upon suitable lift fan air-flows and vent valve behaviour. Ultimately, these videos played a crucial role when designing the full-scale lift fans and the necessary vent valve leakage area.

Figure 1.24 illustrates the required instrumentation, cabling and hardware needed for the model-test.

The model test results indicates safe turbine access up to 2.5 m significant wave heights (see Chapter 4). The typical wave limit for accessing turbines today are 1.5 m [2]. Figure 1.25 shows the system in boarding mode.

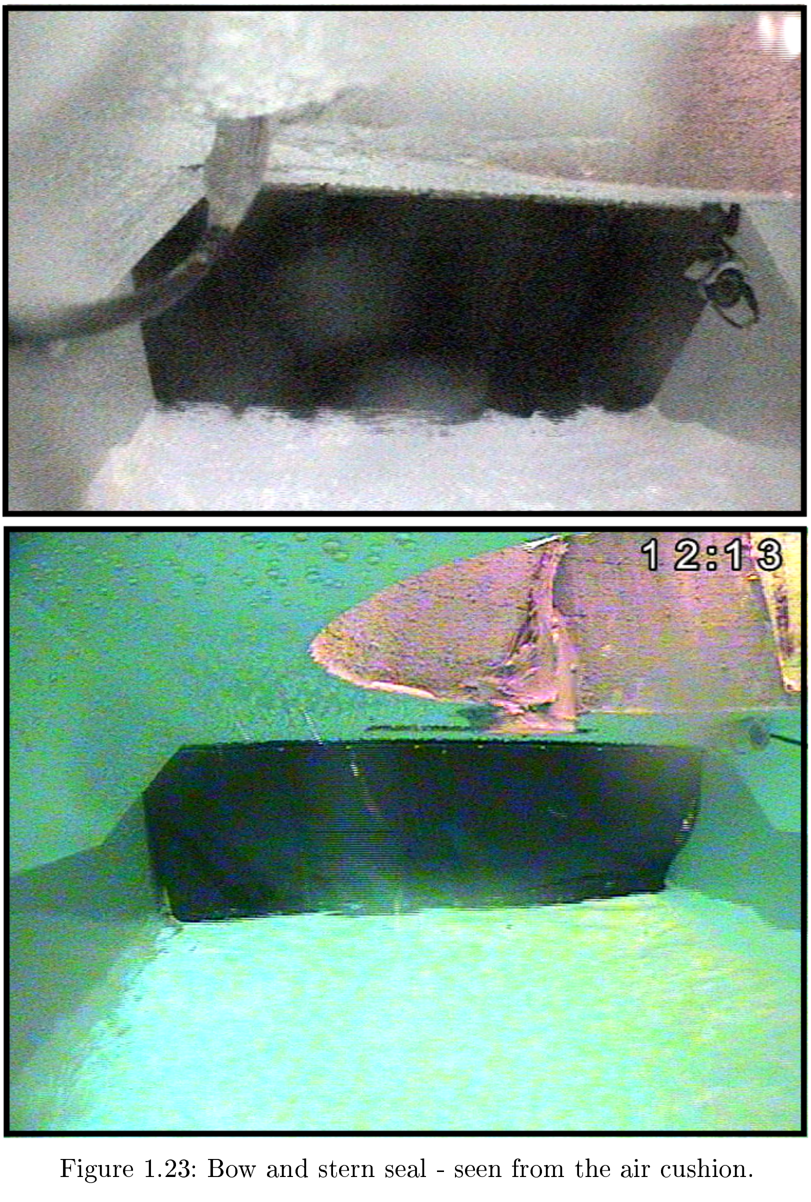

Figure 1.23: Bow and stern seal - seen from the air cushion.

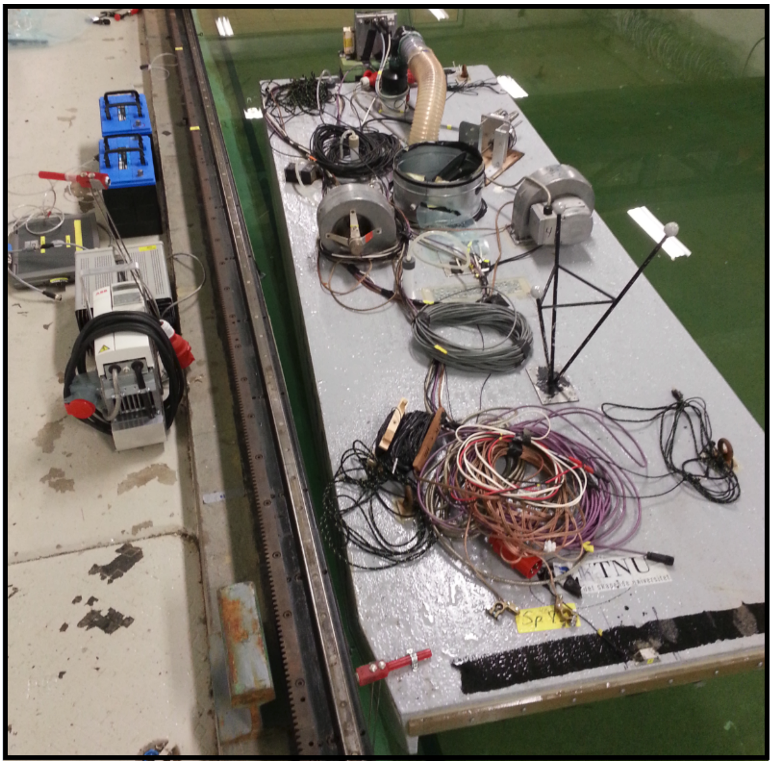

Figure 1.24: Complete model-test equipment.

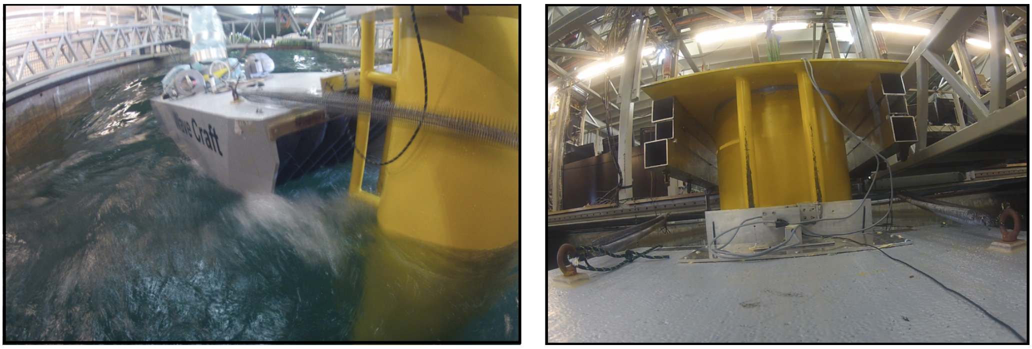

Figure 1.25: Model-test action.

1.5.3 Lift fan validation: model versus full scale

The model-test lift fans are powered by a three-phased 400V AC voltage source and the frequency of this signal can be adjusted to control the fan speed (rpm) which ultimately affects the lift fan characteristics. The lift fan characteristic is given as the fan-flow Q versus the cushion counter pressure P. In general, the more air inflow one could obtain the more effective the BCS would be. A suitable frequency, hence fan speed, was found using the trial and error approach, when the performance of BCS was satisfactory. This criterion was bounded by two constraints:

- There had to be sufficient air flow to make the BCS so effective so that one could safely board a turbine in up to 2.5m significant wave heights.
- The lift fan, running at this certain speed, had to be buildable in the full-scale domain in terms of physical size and weight.

After finding a suitable fan speed, it was then important to find the actual flow-pressure characteristic for this specific frequency so that the full-scaled lift fan was built accordingly with a positive flow margin to account for potential model-scale-effects. This section shows how the model-test lift fan characteristic was found. The test-setup is shown in Fig. 1.26.

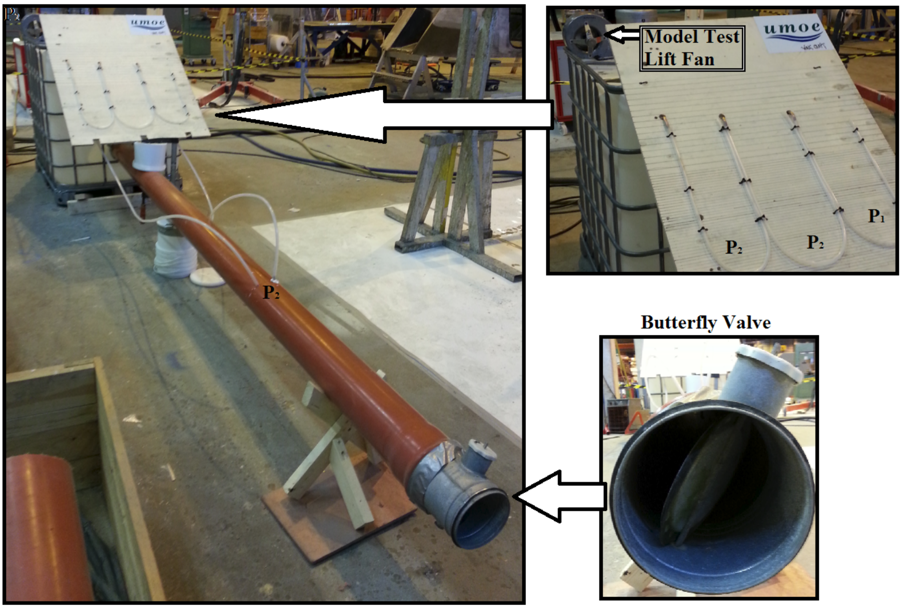

Figure 1.26: Lift fan test setup. Test performed at Umoe Mandal.

Note that the pressure measurement readings P_2 in Fig. 1.26 was implemented to validate and check a digital airflow meter.

The stationary flow of the lift fan Q, (or Q_{in} as denoted in the articles given in Chapter 2) are given according to:

$$Q = Av, \tag{1.1}$$

where the plastic tube area $A = 0.0177\left[m^2\right]$, and $v\ \left[\frac{m}{s}\right]$ is the velocity of the air flowing through the tube near the measurement location of P_2 in Fig. 1.26. The maximum air velocity (v_{max}) will be measured when locating the airflow meter probe in the middle of the tube. Since it is the average velocity that is of interest, we determined this by using the method of [15], page 41, with a plastic tube flow factor $n = 7$. Hence,

$$v = \frac{2n^2}{(n+1)(2n+1)}v_{max} = 0.8167v_{max}, \tag{1.2}$$

Using Bernoulli's principle, the counter pressure data are given according to:

$$P = P_1 + \rho_{air}\frac{1}{2}v^2, \tag{1.3}$$

where the density of air, $\rho_{air} = 1.23\ [\frac{kg}{m^3}]$ and P_1 is the measured pressure inside the tank given in $[Pa]$.

Test procedure: Vary the leakage area out from the Butterfly valve, typically from closed to fully open in 20 steps. For each step, measure P_1 and v_{max} (near the location of P_2 on the tube). Insert the measured values into equation (1.1) - (1.3).

The characteristic for the model test lift fan, and the full scale fan are shown in Fig. 1.27. Note that the full scale lift fan was intentionally built with stronger capacity to ensure a safe margin. The lift fan characteristic curves given in Fig. 1.27 have unified values on the x and y axis due to Umoe Mandal proprietary rights.

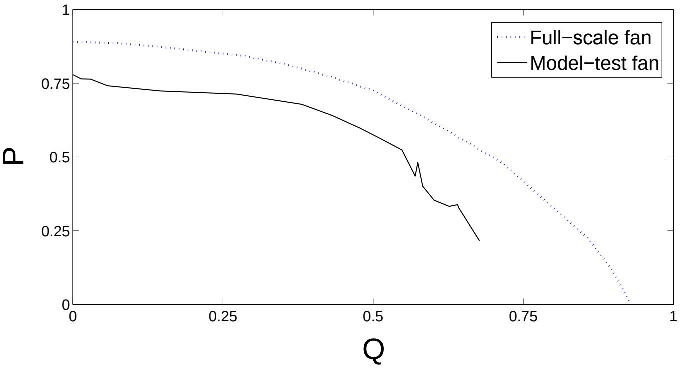

Figure 1.27: Lift Fan Characteristics. The actual full-sized, optimal speed, Wave Craft fan are intentionally designed with a safety margin in terms of air flow capacity.

Chapter 2

Journal and Conference Papers

This chapter presents four conference papers [7], [8], [9], [12] and one journal article [10] which is an extension of [12].

The articles deal with a SES both in- and not in-contact with an offshore wind-turbine structure. The presented articles deal with different phases and approaches regarding the BCS. Table 2.1 summarises the content of each article.

Note 1: The article that exclusively deals with the no-contact mode, is partially titled 'free floating'.

Note 2: Model-test and simulation results given for the no-contact mode has the control system input sensor longitudinally located at the bow tip. For the in-contact mode, the sensor is located around CG.

Table 2.1: Article overview

Section/Article	Title	Description
2.1 / Conference paper I [8]	Simulator and Control System Design for a Free Floating Surface Effect Ship at Zero Vessel Speed	No-contact mode. The focus is to set up a simulation plant model that is validated using real experimental model-test results.
2.2 / Conference paper II [7]	Heave Motion Estimation on a Craft Using a Strapdown Inertial Measurement Unit	The results are given in a no-contact mode but the estimation algorithm is valid for both modes. Estimating heave position is often expensive and requires proper filtering. The article uses an already developed algorithm and uses experimental marine-craft results to assess the performance of the heave estimator.
2.3 / Conference paper III [9]	Motion Compensation System for a free floating Surface Effect Ship	No-contact mode. The article presents a control plant model with a controller that minimizes vertical bow tip motion. A stability analysis is given together with experimental model test results.
2.4 / Conference paper IV [12]	Boarding Control System - for Improved Accessibility to Offshore Wind Turbines	Deals with both in- and not in-turbine-contact mode. The article presents the mathematical modelling of a SES while docking with a turbine and the control system design with results given both from simulations and experimental model-tests.
2.5 / Journal paper [10]	Boarding Control System for Improved Accessibility to Offshore Wind Turbines: Full-scale testing	This article is an extension of conference paper IV. It adds a deeper literature review, a stability investigation and full-scale experimental data of the BCS on-site in an operative wind farm.

2.1 Conference Paper 1

Ø. F. Auestad, J. T. Gravdahl, A. J. Sørensen, and T. H. Espeland. Simulator and control system design for a free floating surface effect ship at zero vessel speed. In *Proceedings of the 8th IFAC Symposium on Intelligent Autonomous Vehicle, Gold Coast, Australia, 26-28 June, 2013.*

Simulator and Control System Design for a Free Floating Surface Effect Ship at Zero Vessel Speed

Øyvind F. Auestad [*,**] **Jan T. Gravdahl** [*]
Asgeir J. Sørensen [***] **Trygve H. Espeland** [**]

[*] *Dept. of Eng. Cybernetics, NTNU, N-7491 Trondheim, Norway;*
e-mail: oyvind.auestad@itk.ntnu.no
[**] *Umoe Mandal AS, N-4515 Mandal, Norway*
[***] *Centre for Autonomous Marine Operations (AMOS), Dept. of Marine Technology, NTNU, N-7491, Trondheim, Norway*

Abstract: This paper covers vertical motion damping of a free floating Surface Effect Ship (SES) at zero vessel speed. Vertical motion damping is requested at the bow deck of the SES during offshore wind turbine docking operation. Vertical motion damping provides a safer transfer of personnel and goods from vessel to the wind mill in moderate/rough sea states. This will provide an increased operational weather window access for maintenance and repair.

The paper has two main contributions. 1) A simulator model for a SES. This is referred to as the cushion process plant model and provides a valid simulation tool for the control system. 2) A simple controller for actuating air cushion pressure. The presented controller actively controls the air flow actuators to the air cushion in order to minimize vertical motions at the vessel bow. A numerical stability investigation for the controller is included.

Keywords: Ship control, Feedback control

---

1. INTRODUCTION

Surface Effect Ships offer reduced hydrodynamic forces acting on the side hull compared to conventional catamarans. The SES is known to offer high speed as well as great sea-keeping capabilities in rough seas.

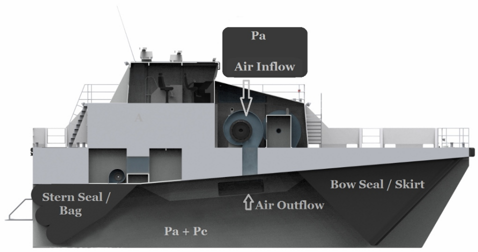

Fig. 1. The SES Concept (Umoe Mandal (UM) Proprietary)

The SES rides on an air cushion enclosed by catamaran type side hulls and flexible rubber seals in stern and bow end. During transit, the air cushion approximately lifts 80 % of the vessel mass, leaving only a minor part exposed to hydrodynamic disturbances. One or more lift fans provide cushion air inflow. The fans are assumed to run at constant rotational speed. The air cushion actuator is composed of adjustable ventilation valves for controlling the air outflow. By closing the ventilation valve the vessel will increase its vertical position (upwards). The opposite effect will appear by opening the valve. This paper presents a SES simulator model as well as a controller that actively adjusts the ventilation valve in order to compensate for encountered wave propagation.

umoe WAVE CRAFT

Fig. 2. This paper deals with UM's Wave Craft (UM Proprietary)

The SES simulator was developed for design and numerical testing of the proposed control system. The simulator calculates enclosed air cushion volume, air flows and a set of equations in order to compute cushion pressure at each time instance. The cushion pressure acts on the wet deck area which induce forces acting on the craft.

The control problem of this paper is different from traditional air flow control on a SES which is known as a Ride Control System (RCS) where one is striving to damp out pressure variations which corresponds to high vertical accelerations during transit, see [Sørensen and Egeland, 1995]) and [Kaplan and Davies, 1978]. These accelerations result in a passenger comfort problem.

In contrast, the controller presented here encourage large pressure variations in order to minimize vertical motions at the bow tip excited by medium/ large wave disturbances. This is done by changing the rotation point in pitch from center of gravity to the vessel bow tip.

A similar task was introduced by Basturk et al. [2011], where disturbance cancellation was performed on another Umoe Mandal developed vessel, the T-Craft (Hybrid Air Cushion - Hovercraft). This work involves active control of the airflow in order to minimize wave induced motion between two ramp-connected ships. Another work by Basturk and Krstic [2012] presents an observer for first order wave propagations that uses measurement of state derivatives. This utilizes the fact that one can implement the system using only a heave accelerometer.

2. SES SIMULATOR - PROCESS PLANT MODEL

The SES simulator is implemented using the integrated ship design tool *ShipX* [Marintek, 2012]. *ShipX* consist of several necessary plug-ins in order to simulate a SES: VeRes calculates offline hydrodynamic vessel response using strip theory according to various predetermined parameters such as vessel dimension, mass distribution, radii of gyration, vessel velocity and a desired set of wave propagation's and headings.

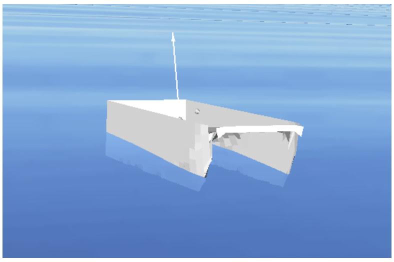

Fig. 3. SES Simulation and visualization using ShipX plug-ins

Online simulation of the vessel and environmental disturbances acting on the vessel is performed by the Vessel Simulator (VeSim). All hydrodynamic forces acting on the craft are calculated by VeSim. The air cushion forces and moments acting on the vessel are not build into ShipX. This is solved by externally sending these forces and moments to VeSim, see figure 4. The calculation is based on Faltinsen [2005] with some minor adjustments. The cushion process plant was first implemented by Espeland [2008] and further developed in [Auestad, 2012]. The model also includes dynamics from the flexible rubber bow and stern seals [Wu, 2011]. The seal dynamics includes seal leakage and seal forces acting on the vessel. The seal dynamics are not further discussed in this article.

Figure 4 illustrate the overall SES Simulator implemented in VeSim. It is the green subsystem on the upper left corner that is implemented and discussed in this paper, the rest is handled by ShipX and VeSim.

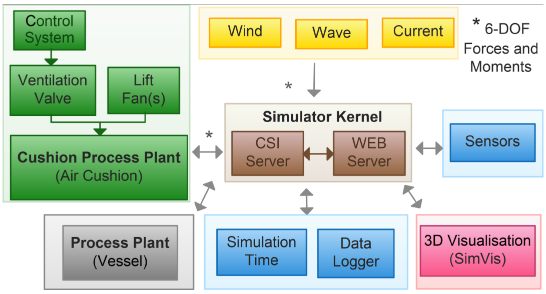

Fig. 4. Architecture of the SES Simulator. CSI: Common Simulation Interface. The WEB server enables the simulator to receive parameters and input via an internet browser.

2.1 Cushion Process Plant Model

In this section we derive an expression for the cushion pressure variations which enable us to calculate the air cushion forces acting on the vessel. Only the most vital aspects of this process are discussed. We define a moving coordinate system, B, whose origin is located at the mean water plane below the center of gravity (CG). The **x**,**y** and **z** axes are defined positive forward, to the port and upwards respectively, as illustrated in figure 5.

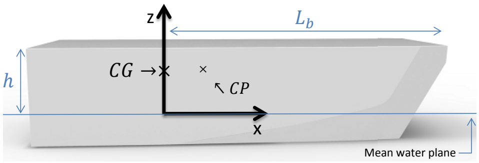

Fig. 5. Body fixed coordinate system B. CG and CP are set to illustrate possible longitudinal positions but not actual design parameters.

CP, as illustrated in figure 5, denotes the longitudinal center of pressure which is the attack point of the cushion pressure, $\eta_{1,2,3}$ represent surge, sway and heave which respectively denotes the translation along the **x**, **y** and **z** axes. $\eta_{4,5,6}$ respectively represent roll, pitch and yaw which is rotation around the given axes according to the right hand rule. The equation of motion are formulated in the B-frame.

Using a 3D model of the craft, the enclosed air cushion volume Ω is numerically calculated as a function of time according to:

$$\Omega(t) = \iint_{A_c} h_c + \eta_3(t) + y\,\eta_4(t) - x\,\eta_5(t) - T - \zeta(x,y,t)\,dA, \tag{1}$$

where $h_c = h_c(x,y)$ is the spatial varying height from the baseline to the wet deck (cushion roof), A_c is the cushion area, T and ζ are, respectively, draught and wave elevation.

Total cushion pressure is $P_c(t) + P_a$, where P_a is the atmospheric pressure, and $P_c(t)$ is cushion excess pressure. The cushion dynamics are linearized around an equilibrium air cushion excess pressure P_0. P_0 corresponds to the cushion excess pressure in the case of constant lift fan rotational frequency, constant valve leakage area (A_0^{ctrl}) and no waves. The non-dimensional uniform pressure variation $\mu_u(t)$ is defined according to:

$$\mu_u(t) = \frac{P_c(t) - P_0}{P_0}, \tag{2}$$

The air cushion air inflow (Q_{in}) is given by a designed lift fan characteristic as a function of $P_c(t)$. The cushion air outflow is given by:

$$Q_{out}(t) = c_n A_L(t)\sqrt{\frac{2P_c(t)}{\rho_a}} \tag{3}$$

where ρ_a is the atmospheric density of air and $0 < c_n < 1$ is a correction term for leakage orifice. This term is assumed constant. $A_L(t)$ is the total cushion leakage area.

The cushion process plant is linearized. Using Taylor Expansion on (3) with respect to $\mu_u(t)$ around the equilibrium $\mu_u = 0$ yields:

$$\begin{aligned} Q_{out}(t) &\approx c_n A_L(t)\sqrt{\frac{2P_0}{\rho_a}} + \frac{1}{2}c_n A_L(t)\sqrt{\frac{2P_0}{\rho_a}}\mu_u(t) \\ &= c_n A_L(t)\sqrt{\frac{2P_0}{\rho_a}}\left(1 + \frac{\mu_u(t)}{2}\right), \end{aligned} \tag{4}$$

Note that the total cushion leakage $A_L(t)$ include leakage contribution from under the side hulls, seals and the active controllable ventilation valve:

$$A_L(t) = A^{SEALS}(t) + A^{HULL}(t) + A^{CTRL}(t) \tag{5}$$

Two more equations must be satisfied in order to calculate the cushion pressure $P_c(t)$.

(1) A continuity equation for the air mass inside the cushion using the chain rule yields

$$\begin{aligned} \dot{m} &= \dot{m}_{in} - \dot{m}_{out} \\ &= \frac{d}{dt}(\rho_c \Omega) \\ &= \dot{\rho}_c(t)\,\Omega(t) + \rho_c(t)\,\dot{\Omega}(t), \end{aligned} \tag{6}$$

where ρ_c is the density in the air cushion. Faltinsen [2005] and Kaplan and Davies [1974] shows that the mass rate can be expressed as:

$$\rho_{c0}\left[Q_{in}(t) - Q_{out}(t)\right] = \dot{\rho}_c(t)\,\Omega(t) + \rho_c(t)\,\dot{\Omega}(t), \tag{7}$$

where ρ_{c0} is the air mass density at equilibrium excess pressure P_0. A normal simplification is setting $\rho_{c0} = \rho_a$.

(2) An adiabatic equation relating pressure and mass density, assuming ideal gas:

$$\frac{P_c(t) + P_a}{P_0 + P_a} = \left(\frac{\rho_c(t)}{\rho_a}\right)^{\gamma}, \tag{8}$$

where $\gamma = 1.4$ is the ratio of heat capacities for air. Rewriting (8) using (2) and linearizing $\rho_c(t)$ around P_0 using Taylor expansion results in:

$$\rho_c(t) \approx \rho_a\left(1 + \frac{\mu_u(t)P_0}{\gamma(P_0 + P_a)}\right). \tag{9}$$

Note that equation (6) requires $\dot{\rho}_c$. Differentiating (9) with respect to time yields:

$$\dot{\rho}_c = \frac{\rho_a P_0}{\gamma(P_0 + P_a)}\,\dot{\mu}_u. \tag{10}$$

Using (4), (9) and (10) and inserting this into (7) yields:

$$\rho_a\left[Q_{in}(t) - c_n A_L(t)\sqrt{\frac{2P_0}{\rho_a}}\left(1 + \frac{\mu_u(t)}{2}\right)\right] = \frac{\rho_a P_0}{\gamma(P_0 + P_a)}\,\dot{\mu}_u(t)\,\Omega(t) + \rho_a\left(1 + \frac{\mu_u(t)P_0}{\gamma(P_0 + P_a)}\right)\dot{\Omega}(t) \tag{11}$$

which can be rewritten:

$$\dot{\mu}_u + A^*\mu_u(t) = B^* \tag{12}$$

Where:

$$\begin{aligned} A^* &:= \left[\frac{\gamma(P_0 + P_a)c_n A_L(t)}{2P_0\,\Omega(t)}\right]\sqrt{\frac{2P_0}{\rho_a}} + \frac{\dot{\Omega}(t)}{\Omega(t)} \\ B^* &:= \frac{\gamma(P_0 + P_a)}{P_0\Omega(t)}\left[Q_{in}(t) - c_n A_L(t)\sqrt{\frac{2P_0}{\rho_a}} - \dot{\Omega}(t)\right] \end{aligned} \tag{13}$$

Finally, in the simulator, (12) is solved for each time instance i using the integration factor:

$$\begin{aligned} g(t) &:= \int_{t_{i-1}}^{t_i} A^*\,dt \\ \mu_u(t) &= e^{-g(t)}\int_{t_{i-1}}^{t_i} B^*\,e^{g(t)}\,dt \end{aligned} \tag{14}$$

The cushion pressure induce forces and pitch moments acting on the vessel according to:

$$\mathbf{F_{cushion}}(t) := -\iint_S P_0(1 + \mu_u)\mathbf{n}\,dS \tag{15}$$

$$\mathbf{M_{cushion}}(t) := -\iint_S P_0(1 + \mu_u)(\mathbf{r} \times \mathbf{n})\,dS, \tag{16}$$

where $\mathbf{r}$ is a vector from the origin to the point where the moments are calculated. $\mathbf{F_{cushion}}$ and $\mathbf{M_{cushion}}$ are sent to VeSim as illustrated in figure 4, where they are merged with the environmental and hydrodynamic forces acting on the hull. The location of the surface S and normal vector n is shown in figure 6.

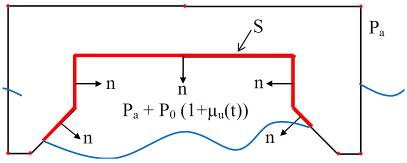

Fig. 6. Calculating Air Cushion Forces and Moments for the Simulator

3. CONTROL SYSTEM - CONTROL PLANT MODEL

The Control Plant Model differs from the Process Plant Model since it is a simplified mathematical description of the process plant that is relevant to the control problem.

While the equations in section 2.1 are based on Faltinsen [2005] the following are based on Sørensen and Egeland [1995]. Sørensen presents both coupled and decoupled equations for heave, pitch and uniform pressure variations.

The equations used in this analysis are quasi-coupled. With this, we understand that there is no coupling between heave and pitch with respect to hydrodynamic added mass, water wave radiation damping and hydrostatic coefficients, as this his is assumed negligible in the B-frame (figure 5). However, there is coupling between uniform pressure variations and pitch velocity. This coupling is necessary to include since the Wave Craft has very narrow side hulls at the fore-end compared to the stern. To obtain a reasonable trim angle when lift fans are turned off, the longitudinal center of gravity is forced relatively far to the stern. Compared to other SES, this leads to a non-negligible gap between the center of pressure and longitudinal CG. This is also accounted for in the Process Plant Model. There is also a coupling between heave and pitch in the controller when transforming the motion from the control point to the chosen coordinate system. Therefore, we assume that translation and velocity for both heave and pitch are available for measurement.

Remark 1. Sørensen and Egeland [1995] also presents the solution to damp spatial varying pressure variations around the resonance frequencies of the vessel, this is not discussed here or in the cushion process plant model since such a short SES, at zero speed, does not experience acoustic vibrations. This result in certain simplifications.

3.1 Craft Dynamics

The following control plant model include contributions from hydrodynamic buoyancy and air cushion dynamics.

The active controlled leakage area of the ventilation valve can be expressed as:

$$A^{CTRL} = A_0^{CTRL} + \Delta A^{CTRL}, \tag{17}$$

where A_0^{CTRL} is the reference leakage area allowing two sided control as discussed in Kaplan and Davies [1974].

The dynamics in heave according to Sørensen and Egeland [1995] is given according to:

$$(m+A_{33})\,\ddot{\eta}_3(t)+B_{33}\,\dot{\eta}_3(t)+C_{33}\,\eta_3(t)-A_c\,P_0\,\mu_u(t) = F_3^e(t), \tag{18}$$

and the dynamics in pitch can be written:

$$(I_{55}+A_{55})\ddot{\eta}_5(t)+B_{55}\dot{\eta}_5(t)+C_{55}\eta_5(t)+A_c p_0 x_{cp}\mu_u(t) = F_5^e(t), \tag{19}$$

where m and I_{55} are vessel mass and the moment of inertia around the body fixed y-axis. Let j = 3,5 respectively denote heave and pitch. A_{jj} is hydrodynamic added-mass coefficient, B_{jj} is the water wave radiation damping coefficient and C_{jj} is found by integrating over the water plane area of the side hulls. F_j^e is the hydrodynamic excitation force acting on the side-hulls acting in j direction. A_c is equilibrium air cushion area. x_{cp} is the longitudinal position of the center of pressure. The hydrodynamic excitation force in heave can be expressed as:

$$F_3^e(t) = 2\zeta_a e^{-k\,d}\frac{sin\frac{k\,L}{2}}{\frac{k\,L}{2}}\left(C_{33}-\omega_0^2 A_{33}\right)sin\,\omega_0 t, \tag{20}$$

where $k = 2\pi/\lambda$. ζ_a, λ and ω_0 are respectively sea wave elevation amplitude, length and frequency, d is draft of side hulls. The hydrodynamic excitation force in pitch is given by:

$$\begin{aligned}F_5^e(t) = 2\zeta_a e^{-k\,d}\Big[\Big(\frac{1}{k}cos\frac{k\,L}{2}-\frac{2}{k^2\,L}sin\frac{k\,L}{2}\Big)\\ \left(C_{33}-\omega_0^2 A_{33}\right)\Big]cos\,\omega_0 t\end{aligned} \tag{21}$$

The uniform cushion pressure equation is given by:

$$\begin{aligned}K_1\,\dot{\mu}_u(t)+K_3\,\mu_u(t)+\rho_{c0}\,A_c\,\dot{\eta}_3(t)-\rho_{c0}A_c x_{cp}\dot{\eta}_5 =\\ K_2\;\Delta A^{CTRL}(t)+\rho_{c0}\,\dot{V}_0(t),\end{aligned} \tag{22}$$

where:

$$\begin{aligned}K_1 &= \frac{\rho_{c0}\,h_0\,A_c}{\gamma\left(1+\frac{P_a}{P_0}\right)},\\ K_2 &= \rho_{c0}\,c_n\sqrt{\frac{2P_0}{\rho_a}},\\ K_3 &= \frac{\rho_{c0}}{2}\left(Q_0-2\,P_0\,q\frac{\partial Q_{in}}{\partial P}|_0\right),\end{aligned} \tag{23}$$

ΔA^{CTRL} is the controlled air flow leakage out of the air cushion, h_0 is the height from waterline to wetdeck at equilibrium pressure P_0, Q_0 is the equilibrium air flow, $\frac{\partial Q_{in}}{\partial P}|_0$ is the lift fan characteristic slope at equilibrium point, $\dot{V}_0(t)$ is the rate of wave volume pumping of dynamic pressure, q is the total number of lift fans (if more than one, assume they run at similar rotational speed and share the same fan characteristic).

The rate of wave volume pumping is expressed as:

$$\dot{V}_0(t) = A_c\,\zeta_a\,\omega_0\,\frac{sin\frac{k\,L}{2}}{\frac{k\,L}{2}}\,cos(\omega_0 t) \tag{24}$$

3.2 State Space Model

Consider the following control plant model of the linear time-invariant (LTI) system of the form

$$\begin{aligned}\dot{\mathbf{x}} &= \mathbf{A}\,\mathbf{x}+\mathbf{B}\,u+\mathbf{E}\,\mathbf{v}\\ \mathbf{y} &= \mathbf{C}\,\mathbf{x},\end{aligned} \tag{25}$$

where

$$\mathbf{x} = \left[\,\eta_3\;\eta_5\;\dot{\eta}_3\;\dot{\eta}_5\;\mu_u\,\right]^T \quad ,\mathbf{v} = \left[\,F_3^e\;F_5^e\;\dot{V}_0\,\right]^T, \tag{26}$$

where $\mathbf{x}(t)$ is the 5-dimensional state vector, $u(t) = \Delta A^{CTRL}$ is the scalar control input, $\mathbf{y}(t)$ is the 2-dimensional measurement vector which will be discussed in the next section. See appendix A and Sørensen and Egeland [1995], respectively, for the numerical and analytic time invariant matrices $\mathbf{A}$, $\mathbf{B}$ and $\mathbf{E}$.

3.3 Control System

It is desired to minimize the bow motion acting in the defined $\mathbf{z}$ axis located at the vessel bow. Defined this as coordinate system B_2 which has the same axes direction of the coordinate system B, but the origin is positioned at the vessel bow. This corresponds to placing an accelerometer at the bow, and integrating the signal twice, respectively to $\dot{\eta}_{3\_bow}$ and η_{3_bow}. The coordinate system as defined in section 2.1 has its origin defined below CG, hence one must transform the motion from the bow to the origin in the same coordinate frame. In the absent of pitch ($\eta_5 = 0$), $\eta_{3,bow} = h+\eta_3$, where h is the height from the mean water plane to the bow deck. It becomes clear that η_{3_bow} will increase its value when the bow/nose is pointing upwards (negative pitch). It can easily be shown that:

$$\begin{aligned}\eta_{3\_bow} &= h + \eta_3 + L_b\, tan(-\eta_5)\\ \eta_{3\_bow} &= h + \eta_3 - L_b\, tan(\eta_5),\end{aligned} \tag{27}$$

By linearizing (27) around $\eta_5 = 0$, (27) can be rewritten:

$$\eta_{3\_bow} = h + \eta_3 - L_b \eta_5 \tag{28}$$

Differentiating (28) with respect to time yields:

$$\dot{\eta}_{3\_bow} = \dot{\eta}_3 - L_b \dot{\eta}_5, \tag{29}$$

using (28) and (29), $\mathbf{y_0}$ and $\mathbf{y}$ can be expressed as:

$$\begin{gathered}(\mathbf{y_0} - \mathbf{y}) = -\begin{bmatrix}\eta_{3\_bow}\\ \dot{\eta}_{3\_bow}\end{bmatrix},\\ \mathbf{y_0} = \begin{bmatrix}-h\\ 0\end{bmatrix}, \quad \mathbf{y} = \mathbf{C}\,\mathbf{x} = \begin{bmatrix}1 & -L_b & 0 & 0 & 0\\ 0 & 0 & 1 & -L_b & 0\end{bmatrix}\mathbf{x}\end{gathered} \tag{30}$$

Therefore, the following feedback controller is proposed for minimizing motion along the $\mathbf{z}$ axis of the B_2 frame:

$$u = \mathbf{K}\,(\mathbf{y_0} - \mathbf{y}) \tag{31}$$

where $\mathbf{K}$ is a time invariant feedback gain matrix given by:

$$\mathbf{K} = [K_p \;\; K_d] \tag{32}$$

Consequently, the controller tries to change the rotation point in pitch from CG to the bow tip.

3.4 Discussion

The control system is virtually moving the center of rotation in order to minimize heave position and velocity at the vessel bow. In order to try to understand this concept mathematically the closed loop pressure equation can be written:

$$\dot{\mu}_u = -\frac{K_3}{K_2}\mu_u - \frac{A_c\rho_{c0}}{K_1}\dot{\eta}_{3\_cp} - \frac{K_p}{K_2}\eta_{3\_bow} - \frac{K_d}{K_2}\dot{\eta}_{3\_bow}, \tag{33}$$

where $\dot{\eta}_{3\_cp} = \dot{\eta}_{3\_cp}(\eta_3, \eta_5)$ is heave velocity acting at the center of pressure (se fig 5). Lets first discuss the behavior when the control system is inactive. We set $K_p = K_d = 0$. Since the constants are defined positive, the first two terms in (33) will stabilize the pressure and heave velocity acting on the wetdeck.

By gradually increasing the control gains, the two last terms in (33) will dominate the two first. The cushion pressure will try to minimize $(\mathbf{y_0} - \mathbf{y})$ by altering the cushion pressure in order to change the longitudinal rotation point in pitch.

3.5 Stability properties of the control system

Due to limited space, this paper does not consider parametric uncertainties, classification of disturbance, optimal or robust control properties. Therefore a very brief numerical stability investigation will be given. It can be shown that the pair $(\mathbf{A}, \mathbf{B})$ is stabilizable and $(\mathbf{A}, \mathbf{C})$ is observable. Note that we will be investigating stability of the origin of the B-system for different control gains. The closed loop perturbed system in (25) can be expressed in the frequency domain as:

$$\begin{aligned}\mathbf{y} &= \mathbf{C}\,(s\,\mathbf{I_{5x5}} - \mathbf{A} + \mathbf{B}\,\mathbf{K}\,\mathbf{C})^{-1}\,(\mathbf{B}\,\mathbf{K}\,\mathbf{y_0} + \mathbf{E}\mathbf{v})\\ &:= \mathbf{C}\,(s\,\mathbf{I_{5x5}} + \mathbf{H_0})^{-\mathbf{1}}\,(\mathbf{B}\,\mathbf{K}\,\mathbf{y_0} + \mathbf{E}\mathbf{v})\\ &:= \mathbf{H_1}(s)\mathbf{y_0} + \mathbf{H_2}(s)\mathbf{v},\end{aligned} \tag{34}$$

where $\mathbf{H_1}$ is the transfer function matrix from $\mathbf{y_0}$ to $\mathbf{y}$, and $\mathbf{H_2}$ is the mapping from the disturbance vector $\mathbf{v}$ to the measurement vector $\mathbf{y}$. $\mathbf{H_1}$ and $\mathbf{H_2}$ share the same poles which corresponds to the zeros of $\mathbf{H_0}$.

All zeros of $\mathbf{H_0}$, except a complex conjugated pair, have negative real parts for all K_p and all K_d. Therefore, the stability relies on this conjugated pair. Denote the real part of these two poles as α. Figure 7 shows α for different K_p and K_d.

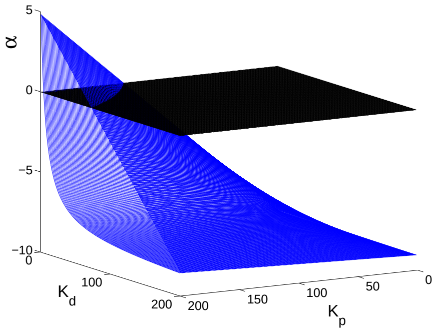

Fig. 7. α - The real value of the complex conjugated pair of poles that determine stability

In order to achieve stability, the real part of all the poles must be negative, therefore, for a large K_p, K_d must be chosen sufficiently large according to figure 7.

4. RESULTS

The objective of this paper is to develop a functional and valid SES simulator and to investigate the concept of damping wave induced motion at the vessel bow. Figure 8 shows the time series for P_c, η_5 and η_3 vs η_{3_bow} for a simulation run in regular wave head sea. The control system is initially inactive and turned on at $t \approx 3710[s]$. The figure illustrates the concept of vertical motion damping at the bow deck by changing the rotation point in pitch using the controller given in (31). In this sea state, η_3 and η_5 independently remain relatively unchanged, regardless if the control system is active or not.

Figure 9 illustrates that the comprehensive computational simulator (Process Plant Modell) in VeSim is modeling the actual real world. The heave position at bow deck is shown for the simulator and an actual model test of the Wave Craft. The model test has a scale factor 1/8 compared to full-scale craft and possess realistic, scaled actuators, sensors and seals. Although this paper is not meant to discuss model test results, the comparison figure is given to validate the simulator. It must be noted that the model test provided some uncertain simulator parameters. The control system is initially active, and then turned off.

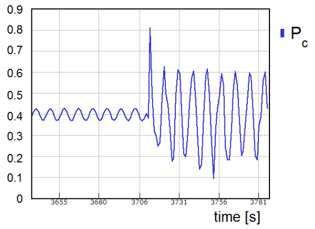

(a) Cushion Pressure - P_c

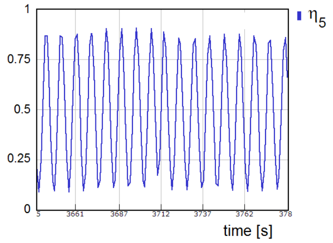

(b) Pitch - η_5

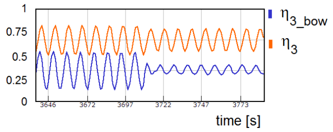

(c) Heave position at η_{3_bow} and η_3

Fig. 8. Simulation run, regular head sea, Wave height and period are 0.5m and 8s. All variables have been normalized.

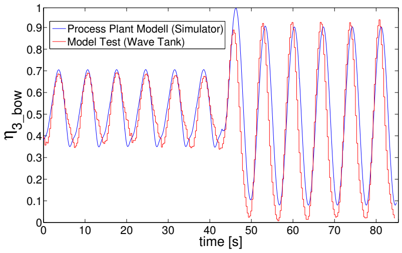

Fig. 9. Simulator validation and vertical bow motion damping, showing the control system respectively toggled on and off. The y-axis is normalized.

5. CONCLUSIONS AND FURTHER WORK

This paper contains a study in modeling and control of a Surface Effect Ship at zero vessel speed. The main focus is to create an overall credible simulation toolbox for a SES. Optimal performance has not been a topic, although the results clearly illustrates the concept of motion damping.

A process plant for modelling a SES has been succesfully implemented. A simplified control plant model is presented for the preliminary stability investigation of the control system.

Further work involves three important studies. Due to parametric uncertainties a global stability analysis is necessary. Obtaining a heave position signal which is a control input is possible but often an expensive task. It is therefore desired to implement a heave observer. For optimal control, control gains need to vary as functions of wave height and period. Some sort of adaptive control system is therefore desired.

REFERENCES

Ø. Auestad. Heave control system for a surface effect ship: Disturbance damping of wave induced motion at zero vessel speed. Master's thesis, Department of Engineering Cybernetics, NTNU, 2012.

H. Basturk and M. Krstic. Adaptive backstepping cancelation of unmatched unknown sinusoidal disturbances for unknown lti systems by state derivative feedback. *ASME Dynamic Systems and Control Conference*, 2012.

H. Basturk, J. Doblack, and M. Krstic. Air cushion adaptive disturbance cancellation for the reducion of wave induced motion of ramp-connected ships. *11th internatinoal Conference on Fast Sea Transportation, Honolulu Hawaii, USA September*, 2011.

T. H. Espeland. Simulation of motion of ses in waves. Master's thesis, Department of Marine Technology, NTNU, 2008.

O. M. Faltinsen. *Hydrodynamics of high-speed marine vehicles, pp 71-84.* Cambridge UniversityPress, 2005.

P. Kaplan and S. Davies. *A Simplified Representation of the Vertical Plane Dynamics of SES Craft.* AIAA/SNAME Advanced Marine Vehicle Conference, 1974.

P. Kaplan and S. Davies. System analysis techniques for designing ride control system for ses craft in waves. *5th Ship Contr. Syst. Symp. Annapolis, MD*, 1978.

Marintek. Shipx. `http://www.sintef.no/upload/MARINTEK/PDF-filer/Sofware/ShipX.pdf`, 2012. Developed by Edvard Ringen and Dariusz Fahti.

A. J. Sørensen and O. Egeland. Design of ride control system for surface effect ships using dissipative control. *Automatica*, 31:183 – 199, 1995.

MinKang Wu. Improvement to ses seakeeping model in vesim with emphasis on bow and stern seals. Umoe Mandal AS Property, Marintek Sintef, 2011.

Appendix A. SYMBOLIC MODEL MATRICES

$$\mathbf{A} = \begin{bmatrix} 0 & 0 & 1 & 0 & 0 \\ 0 & 0 & 0 & 1 & 0 \\ -1.0006 & 0 & -0.1915 & 0 & 2.8723 \\ 0 & -0.1254 & 0 & -0.9333 & -0.8100 \\ 0 & 0 & -53.3167 & 119.9625 & -17.1696 \end{bmatrix}$$

$$\mathbf{B} = [0\ 0\ 0\ 0\ 8.9234]^{\mathsf{T}}$$

2.2 Conference Paper 2

Unfortunately, an error observed in Section*2.4 Step 4 - Transformation of Motion* was found after the final submission was sent. Therefore, when calculating the transformation of motion from one point on the vessel (body coordinates) to another point given (inertial, NED-frame), the solution given in the literature citation [25] are recommended to use instead.

Ø. F. Auestad, J. T. Gravdahl, and T. I. Fossen. Heave motion estimation on a craft using a strapdown inertial measurement unit. In *proceedings of the 9th IFAC Conference on Control Applications in Marine System, Osaka, Japan, September 17-20, 2013*

Heave Motion Estimation on a Craft Using a Strapdown Inertial Measurement Unit [⋆]

Øyvind F. Auestad [*,**] **Jan T. Gravdahl** [*] **Thor I. Fossen** [*]

[*] *Dept. of Eng. Cybernetics, NTNU, N-7491 Trondheim, Norway;*
e-mail: oyvind.auestad@itk.ntnu.no
[**] *Umoe Mandal AS, N-4515 Mandal, Norway*

Abstract: This paper deals with heave position and heave velocity estimation on a craft. The estimation is done without any knowledge of the specified craft. An accurate estimation of these signals is useful when one wants to control or monitor the heave motions on a platform or a ship such as in a active heave compensated systems. The necessary sensor input for the proposed guidance system is a strapdown inertial measurement unit (IMU) which consists of three gyroscopes and three accelerometers. In this case study, the heave motion estimation is required as input for a control system on a Surface Effect Ship (SES) where it is desired to control the air cushion pressure in order to damp vertical motions. The motions are induced by sea wave propagations. A SES will experience high frequency accelerations on the hull compared to other vessels. A lift fan sets up these accelerations or process disturbances and complicates the performance of the estimation. The estimation is performed using an observer. The observer model is based on a set of superimposed sinusoidals, each with a different excitation frequency. The sum of these denotes the actual heave motion. The estimation algorithm is adaptive in terms of changes in the sea states. Results will be given using real experimental data from model tests of a 3 meter long SES.

Keywords: Observer, strapdown systems, Inertial measurement units, Spectral analysis

1. INTRODUCTION

Several methods for estimating heave motion is available both in literature and on the market. One approach is to aid the IMU with external sensors such as lasers, acoustic or GPS measurements. The latter is done in Fossen and Perez [2009]. However, external aiding usually results in higher costs and dependency on the external sensor. In this paper, only systems with a low cost such as a strapdown Micro-Electro-Mechanical Sensor (MEMS) IMU as sensor measurement are considered.

MRU H [Kongsberg, 2013] is an example of what is available on the market. The Motion Reference Unit (MRU) offers high accuracy but suffers from a high purchasing cost. Godhavn [1998] presents the Seatex MRU which accurately estimates the heave motion using an adaptive heave filter algorithm. The filter minimizes measured acceleration error sources such as bias and noise by adaptively changing the cut off frequencies of a bandpass filter. Kongsberg now owns Seatex.

The approach used in this paper is based on Küchler et al. [2011]. Küchler estimates heave motion using a single accelerometer and shows results both in simulation and through a test bed that consist of two winches and a hook. This paper estimates the motion in a similar way but transfers the motion to a different point on the vessel. Results will be given using real experimental data of a 3 meter long SES with severe process disturbance. Also, the implemented proposed observer has been altered from an EKF to a linear discrete time Kalman Filter without any loss of generality or functionality. The proposed system is Linear-Time-Invariant (LTI) which ensure that the Kalman Filter will converge towards a steady-state.

1.1 Motivation

The case studied in this paper involves the Umoe Mandal's Offshore Service Vessel named The Wave Craft. The Craft is designed for service missions to offshore wind-turbines. The craft is a SES, which rides on an air cushion enclosed by catamaran twin hulls and flexible rubber seals in the bow and in the stern. The air cushion is pressurized using centrifugal lift fans that lifts the vessel towards the water surface leaving only a small portion of the side hulls in the water. The cushion pressure can be altered by controlling the air cushion outflow leakage area. Altering the opening angle of an installed ventilation valve does this. It is damping of the bow tip that is of interest since this is the area where the service personnel will leave the vessel and board the turbine. Is is therefore important that the motion estimation occurs at this point.

Due to the cushion dynamics, the strapdown accelerometers will experience severe process disturbances. These disturbances are unwanted on the estimated heave motion. The magnitudes of these accelerations are varying along the longitudinal position of the ship. Therefore, the model test setup was set up using two options that possibly would alter the performance of the estimation. At the first approach, the IMU, with the accelerometers, was placed

---

[⋆] A special thank to Umoe Mandal who made the model test possible. Also for allowing to sharing logged time series and data.

amidships where the magnitude is assumed low. The motion was transferred to the bow tip using a coordinate transformation. The second approach, which is denoted the direct approach, consist of placing the IMU directly at the vessel bow tip.

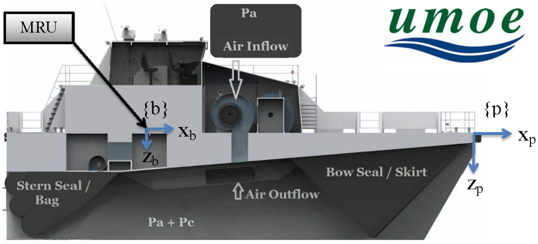

Fig. 1. The SES Concept (Umoe Mandal (UM) Proprietary). Two coordinate systems are defined. The $\{b\}$ frame is body fixed with its origin located at the IMU. Denote the linear translation along the z_b axis as z. The $\{p\}$ frame is formulated with the z_p axis pointing downwards normal to the Earth's surface. The origin is located at the vessel bow tip. Denote the translation along this axis as D. Motion in z and D are both referred to as heave. Both coordinate systems use the right hand rule to determine rotation signs.

Auestad et al. [2013] presents a SES simulator and a control system for damping vertical motions at the bow. This is done by altering the cushion pressure using feedback from the heave motion at the craft's nose tip. An actuator that controls the opening of the ventilation valve will act proportionally to the heave motion. This will arrange for safer transfer of personnel and goods from vessel to turbine foundation. The craft is assumed free floating at zero craft speed. The article assumes that the heave motion is known. In reality, heave velocity is simple to obtain, while heave position is not. Accelerometer measurements are affected by noise and bias. The errors accumulate by the number of times this signal is integrated. Hence, estimating heave position is harder than estimating heave velocity.

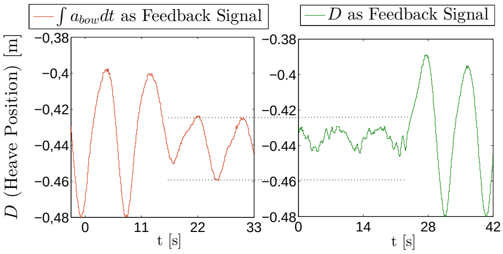

Fig. 2. The plot shows the effect of a long crested regular wave, $T_p = 8.5$s. D is measured by lab equipment and $\int a_{bow}\, dt$ was given by numerical integration of a high-pass filtered accelerometer signal. The accelerometer was attached at the origin of the $\{p\}$ frame.

Figure 2 shows time series for the heave position (expressed in $\{p\}$) from a model test where the vertical wave induced motions are being damped. The control system is inactive at the beginning and at the end of the left and right sub-figure respectively. This corresponds to a constant air cushion pressure. The control system is active for the remaining part and note that the amplitude of the right sub-figure is smaller than of the left. Hence, when the craft faces a long crested wave, such as in this case, the performance is increased when D (see fig. 1) is available. The wave period as denoted T_p.

2. HEAVE MOTION ESTIMATION

The task of this paper is to estimate $\dot{D}$ and D using an IMU as illustrated in figure 1. Define: $\hat{\mathbf{D}} := \left[\dot{\hat{D}}, \hat{D}\right]^T$ and $\hat{\mathbf{z}} := \left[\dot{\hat{z}}, \hat{z}\right]^T$. $\hat{\mathbf{D}}$ is the output of the estimator.

The proposed method for estimating heave motion involves four steps that will be explained in the following. The first three steps are based on [Küchler et al., 2011] while the latter one consist of transforming the motion from the {b} to the {p} frame.

The input for the estimator and the necessary signals from the IMU, is roll rate, pitch rate and linear acceleration along the z_b axis. Denote these as p_{imu}, q_{imu} and $a_{z,imu}$, respectively.

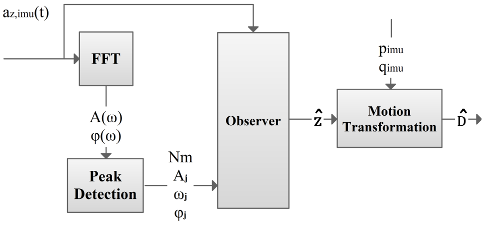

Fig. 3. Illustration of the four necessary steps in order to estimate heave motion.

The estimator model is based on including all forms of waves that will excite craft motions. Heave position, $z = z(t)$, can be modelled as a set of N_m overlaying sine waves [Chakrabarti, 2008]:

$$\begin{aligned} z(t) &= \sum_{j=1}^{Nm} A_j cos(\omega_j t + \varphi_j) + v(t) \\ &:= \sum_{j=1}^{Nm} z_j(t) + v(t) \overset{v=0}{=} \sum_{j=1}^{Nm} z_j(t) \end{aligned} \tag{1}$$

where $j = 1, 2, .., Nm$, A_j, ω_j and φ denotes amplitude, eigenfrequency and phase of each sine wave. Each wave is denoted as a mode. $v(t)$ is included to capture slowly varying effects such as the tidal range. Since our problem only concerns relative heave motion, $v(t)$ is neglected for the rest of the analysis.

2.1 Step 1 - Fast Fourier Transform (FFT)

Eq. (1) is described in the time domain. It can be expressed in the frequency domain using a wave energy spectrum [Faltinsen, 1993]. The spectrum is calculated online using a FFT with a chosen memory length that is sufficiently small to ensure smooth spectral curves. Let $\ddot{A}(\omega)$ and $\ddot{\varphi}(\omega)$

denote the amplitude and phase spectrum of the acceleration signal (therefore the double dot). The wave spectrum illustrates the energy that acts in heave acceleration as a function of frequency.

Figure 3 and eq. (1) indicates that it is the spectrum of heave position that are of interest, and not the heave acceleration spectrum. However, a spectrum transformation from acceleration to position can be calculated directly using:

$$A(\omega) = \frac{\ddot{A}(\omega)}{\omega^2}, \quad \varphi(\omega) = \ddot{\varphi}(\omega) - \pi, \quad \omega > 0 \qquad (2)$$

The accuracy of the estimation is dependent on chosen sampling time of the FFT which gives the spectrum a desired resolution in the frequency plane. In the next section we will see that this corresponds to the number of modes (N_m) that will appear. The window length of the FFT must include and detect the highest frequency of the sea state as well as potential, relevant eigenfrequencies of the craft that might be excited.

2.2 Step 2 - Peak Detection

Figure 4 illustrates the amplitude spectrum discussed in section 2.1. The peak detection consist of localizing every local maximum of $|A(\omega)|$. Every maximum corresponds to a mode j, where $j = 1, 2, ..., N_m$.

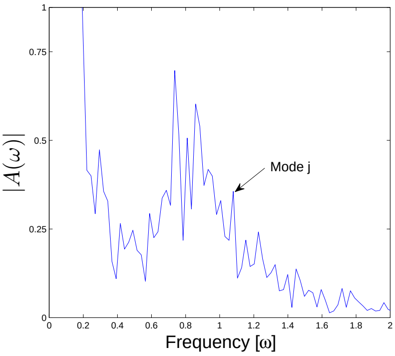

Fig. 4. The normalized amplitude of the frequency response. As the figure indicates, this specific wave has a period of 8.5 seconds ($\omega \approx 0.8$) where the majority of the energy is stored. The tests were performed in a wave tank [1]

Each mode has a specific amplitude (A_j), phase (φ_j) and eigenfrequency (ω_j). This is the output of the peak detection algorithm. In order to avoid singularities, modes with eigenfrequency equal to zero or modes that are sufficiently close to a neighbour mode must be removed. In order to handle changes in the sea states, the peak detection must be repeated every fixed time interval T.

2.3 Step 3 - Observer

An observer is required since the FFT only considers mean values over a finite time horizon. By setting $v = 0$ in eq. (1), each mode is considered a solution to an undamped oscillator The following ordinary differential equation describes the dynamics of the oscillator:

$$\ddot{z}_j + \omega_j^2 z_j = 0, \quad t > t_0, \qquad (3)$$

where $j = 1, 2, ..., N_m$. The initial conditions of (3), namely $z_j(t_0)$ and $\dot{z}_j(t_0)$ are given according to (1) and by differentiating (1) along its system trajectories using the output from the peak detection algorithm, t_0 denote the time whenever the system needs to be re-initialized. In order to keep the decay time down, one must only re-initialize the system whenever a new mode j is either detected or vanished from the output of the peak detection algorithm. This mode, is respectively, added or removed from the system. The system needs to be adaptive in terms of changes in the sea state, therefore, the dynamics of the eigenfrequencies, ω_j, are modeled as random walk parameters:

$$\dot{\omega}_j = \epsilon(t), \qquad (4)$$

where $\epsilon(t)$ is defined as white noise with zero mean and unit variance. When comparing the heave motion estimation with the true state, which will be discussed later, it was shown that 4 could be solved independent of the remaining states without loosing any performance. By first solving (4) for each mode j, the remaining, uncoupled term of (3) can be presented as a linear system. Define the vector: $\mathbf{x}_j = [z_j, \ \dot{z}_j]^T = [x_{1,j}, \ x_{2,j}]^T$. Each mode denote an oscillator and can be written in state space form:

$$\begin{aligned} \dot{\mathbf{x}}_j &= [x_{2,j}, \ -\omega_j^2 x_{1,j}],^T \quad t > t_0, \ \mathbf{x}_j(t_0) = \mathbf{x}_{j,0}, \\ y_j &= -\omega_j^2 x_{1,j}, \end{aligned} \qquad (5)$$

where $j = 1, 2, ..., N_m$. Each of the N_m modes are now modelled. Before we can implement the observer, one must compensate for certain errors when measuring heave acceleration:

$$a_{z,imu} = \sum_{j=1}^{Nm} y_j - cos(\theta)\, cos(\phi) g + b_z + \xi_z \qquad (6)$$

where g denote gravity and is assumed constant, θ, ϕ respectively denotes roll and pitch angles, b_z and ξ_z denote sensor offset (or bias) and some noise. Eq. (6) illustrates that the measured acceleration signal will contain an offset. Therefore, denote an offset state: x_{off} that is modelled as a random walk parameter:

$$\dot{x}_{off} = \epsilon(t), \quad x_{off}(0) = -cos(\theta)\, cos(\phi) g, \qquad (7)$$

To convert the system from continuous to discrete state space form, let $t_k = k\Delta t$, $k \forall \mathbb{N}$, where Δt is the sampling time of the observer. The initial state is calculated in the same way for the continuous and the discrete time system. The dynamics of the eigenfrequencies, ω_j, in (4) is solved first since it is decoupled from the rest of the system.

We obtain the complete state space system by adding all the N_m states of the modes together with the the offset state x_{off}, the entire system is solved for every time instance and re-initialized if a new mode is either detected or vanishes. The complete discrete system can be written in state space form:

---

[1] All figures containing time series/frequency response, are from model tests of the Wave Craft, performed in cooperation between, SINTEF/Marintek, Umoe Mandal and NTNU. Test results in this paper were performed both at the *MC Lab, NTNU*, and the *Ship Model Tank, Marintek.*

$$\begin{aligned}\mathbf{x}_{k+1} &= \mathbf{A}\mathbf{x}_k \\ \mathbf{y}_k &= \mathbf{C}\mathbf{x}_k,\end{aligned} \tag{8}$$

where

$$\begin{aligned}\mathbf{x}_k &= [\ \mathbf{x}_{1,k},\ \ \mathbf{x}_{2,k},\ \ \ldots\ \mathbf{x}_{N_m,k}\ \ x_{off,k}]^T \\ \mathbf{C} &= [\omega_{1,k}^2,\ \ 0\ \ \omega_{2,k}^2,\ 0,\ \ \ldots\ \omega_{N_m,k}^2,\ \ 0,\ \ 1], \\ \mathbf{A} &= \begin{bmatrix} \mathbf{A}_1 & & & \{\mathbf{0}\} & \\ & \mathbf{A}_2 & & & \\ & & (\ldots) & & \\ & & & \mathbf{A}_{Nm} & \\ & \{\mathbf{0}\} & & & 1 \end{bmatrix}\end{aligned} \tag{9}$$

where $\mathbf{A}_j = \begin{bmatrix} 1 & \Delta t \\ -\omega_{j,k}^2 \Delta t & 1 \end{bmatrix}$, $j = 1, 2, ..., N_m$, $\mathbf{x}_k$ is the $(2N_m + 1 \times 1)$ state space vector and $\mathbf{y}_k$ is the $1 \times (2N_m + 1)$ measurement vector and $\{\mathbf{0}\}$ covers the non-diagonal parts of $\mathbf{A}$ with zeroes.

The observer itself is implemented using a standard discrete time Kalman Filter. The process covariance matrix ($\mathbf{Q}$) is weighted in such a way that the modes with high eigenfrequencies are penalized compared to modes with lower ones. A suitable solution is to multiply each element in $\mathbf{Q}$, which is associated to a mode, with the corresponding eigenfrequency w_j . The covariance of the measurement noise equals the standard deviation of the sensor noise squared.

2.4 Step 4 - Transformation of Motion

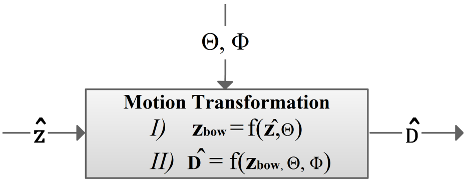

Fig. 5. Structure of the proposed heave motion transformation from $\{b\}$ to $\{p\}$

The output of the proposed observer is $\hat{\mathbf{z}}$ which is heave position and heave velocity at the location of the IMU. This section transfer the motion from this point to the bow tip, thus from the body fixed reference frame $\{b\}$ to the $\{p\}$ frame as illustrated in figure 1. We will divide the problem into two parts. In (I) we will translate the body fixed heave motion from $\{b\}$ to the bow tip. Let the axes point in the same body fixed directions. Denote this new coordinate frame as $\{b_{bow}\}$. Linear translation along the body fixed z axis of $\{b_{bow}\}$ is denoted $\mathbf{z}_{bow}$. In the second part, (II), we transform $\mathbf{z}_{bow}$ to the defined $\{p\}$ frame using Euler angle transformation.

Roll and pitch angles are required for the transformation. Since the angular output from an IMU is angular rate it is necessary to integrate these signals. Additional filtering is required in order to handle measurement errors such as drift and noise. It is assumed that the angular positions are correctly calculated and available for measurement using a method such as in Sabatelli et al. [2011]. Denote roll as ϕ and pitch as θ.

It is also assumed that the unwanted process disturbance, which will be discussed in section 3.1, will only have a very small impact on the calculation of roll and pitch angles. This assumption is made since the angular lab measurements shows no sign of the process disturbance frequencies. Thus, with correct handling of the angular rates, a smooth and accurate estimation of the angular positions will be made.

I) Transforming the motion from one point is discussed in chapter 7.5.4 in Fossen [2011] where one is assuming small roll and pitch angles. This results in a simplified linear transformation. Since the Wave Craft is a vessel designed to handle very rough seas, we will approach the problem without linearisation. The translation is illustrated in figure 6. Remember we are only interested in relative heave motion. It is assumed that both the IMU and the bow point is positioned at the centerline and share the same position on the baseline.

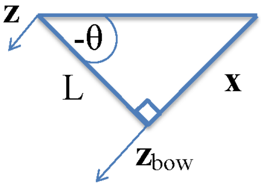

Fig. 6. Coordinate transformation from $\{b\}$ to $\{b_{body}\}$

where L is the longitudinal length from the location of the MRU to the bow tip. Note that the pitch is defined negative with the nose down according to the right hand rule. Hence:

$$\begin{aligned}\mathbf{z_{bow}} &= \hat{\mathbf{z}} + \mathbf{x} \\ &= \hat{\mathbf{z}} + L\,tan(-\theta) \\ &= \hat{\mathbf{z}} - L\,tan(\theta)\end{aligned} \tag{10}$$

II) To change coordinate system from the body fixed $\{b_{body}\}$ to the {p} frame we use section section 2.2.1 in Fossen [2011]. The results follow directly using the Euler angle transformation matrix:

$$\hat{\mathbf{D}} = cos(\theta)\,cos(\phi)\,\mathbf{z_{bow}} \tag{11}$$

3. RESULTS

As mentioned, the results in this section and figure 2 and 4 are based on time series from model test of a 3 meter long SES, namely the Wave Craft. The scale factor is 1 : 8. The peak detection is run online with $T = 15s$ (see section 2.2) The FFT has a certain memory sequence with $a_{z,imu}(k)$ as input in a first in, last out approach. The accelerometer used for the test is an [ICSensors, 2013] and the true heave position is read using [Qualisys, 2013]. Most axis are unified due to UM proprietary rights.

3.1 Severe process disturbances on the accelerometer

Figure 1 illustrates the lift fan that blows air into the air cushion. The cushion dynamics involves large large changes in net air flow due to nonlinear lift fan characteristics and sudden leakages under seals and through the ventilation valve. The dynamics will correspond in accelerations denoted as process disturbances. Figure 7 illustrates the challenges that occur on a SES compared to other crafts when it comes to estimate heave motion using an accelerometer. The lift fan is turned off through the second half of the time series. When the fan is turned off, it is assumed that the process disturbances can be compared to craft such as catamarans or swaths. Figure 7 shows the time series of the air cushion pressure ($P_c(t)$), the accelerometer placed in the origin the $\{b\}$ frame ($a_{z,imu}$) and an accelerometer placed at the bow tip ($a_{z,bow}$).

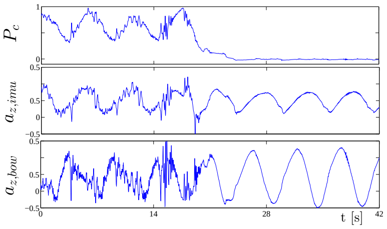

Fig. 7. The air cushion dynamics on a model test SES produce more process disturbances when the lift fans are on versus off. However, it is doubtful that the process noise is directly scalable for a full-sized SES. Regular wave, $T_p = 8.5s$

Note that the process disturbance is even larger on the bow tip. This is why we propose to transform the motion from the $\{b\}$ frame to the bow tip instead of estimating heave motion directly from the bow tip.

3.2 Heave Motion Estimator Performance

For the following results, the control system discussed in section 1.1 is at all times turned on. Two different time series will be shown using an irregular JONSWAP wave with $T_p = 8.5s$. First, we will illustrate heave motion estimation at the location of the MRU in the $\{b\}$ frame. On the following figure, this motion will be transferred to the $\{p\}$ frame where it will be compared to measurements of the true heave position. There will not be done any comparison between estimated heave velocity and the true heave velocity since these results are assumed better than of the position estimates (Küchler et al. [2011]). As previously, the output of the observer/estimator is denoted with a hat ($\hat{\diamond}$) and the true state without.

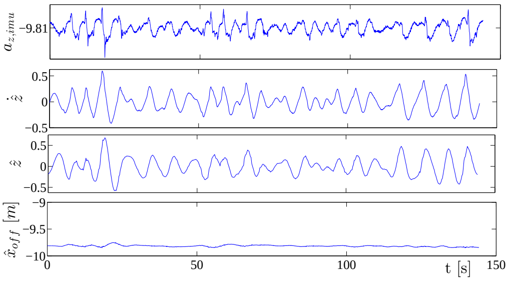

Fig. 8. The time series shows accelerometer signal and heave motion estimation in the $\{b\}$ frame.

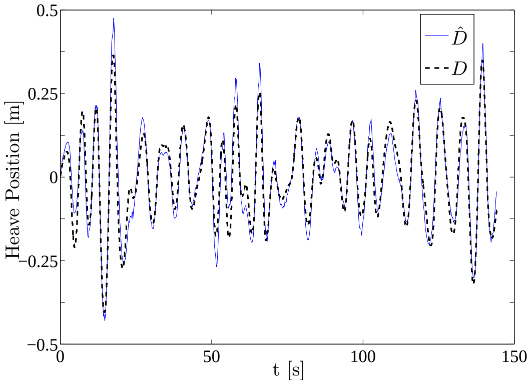

Fig. 9. The motion has been transformed from the $\{b\}$ frame to the $\{p\}$ frame where it is compared to the true heave position read by lab equipment.

Figures 8 and 9 illustrates the performance of the system with acceleration error terms such as gravity, measurement noise and process disturbance. The following figures, 10 and 11 illustrates the performance when we add an instant, fake, bias to the accelerometer, $b_{z,k} = 2$ at $t = \Delta t$. In other words, for each time step after the first, $a_{z,imu}(k) = a_{z,imu}(k) + b_{z,k}$. This illustrates the robustness of the system if a sudden bias or drift error appear on the signal.

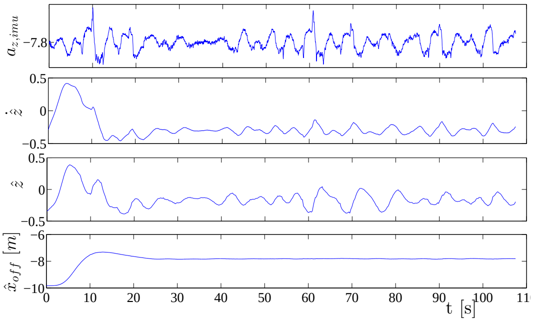

Fig. 10. Bias is added to the accelerometer, $b_{z,k} = +2$.

In figure 10, observe that the offset state converge to the correct value. The estimated heave motion also converges and does not experience any offset. All the figures illustrates that the process disturbances are rejected well since we do not want to expose the actuator to such oscillations in terms of wear and tear.

3.3 Estimate heave motion directly from an accelerometer located at the bow tip

In this section we will investigate the results if we place an accelerometer at the bow tip and use the proposed observer without any transformation of motion from the IMU to the bow tip as explained in section 2.4.1. Note that we are still transforming the motion to the $\{p\}$ reference frame as explained in section 2.4.2 in order to compare it to the true heave position. Figure 12 illustrate this scenario where

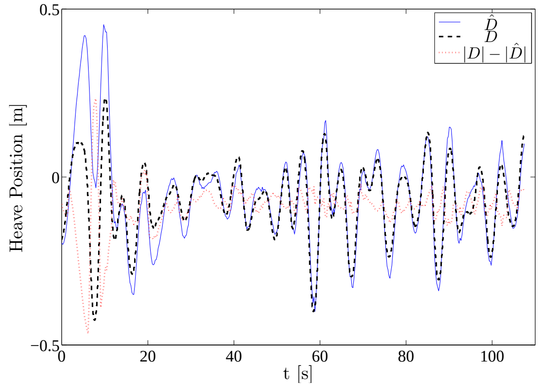

Fig. 11. Bias is added to the accelerometer, $b_{z,k} = +2$.

we denote $\hat{D}_{DIRECT}$ as the direct heave estimation. The time series used are the same as in figure 8. Therefore we will compare if it is best to position the accelerometer amidships and perform a transformation of motion to the bow, or just position the accelerometer directly on the bow tip. The observer remains unchanged in both cases.

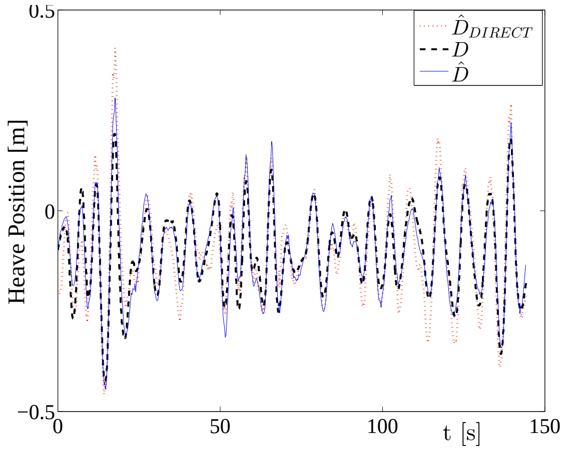

Fig. 12. Heave position estimation of an accelerometer placed at the vessel bow tip ($\hat{D}_{DIRECT}$) versus amidships ($\hat{D}$).

As expected, due to a larger process disturbance on an accelerometer placed on the bow tip, the performance is decreased using the direct approach.

4. CONCLUSIONS AND FURTHER WORK

We are interested in estimating heave motion at a specific point on a vessel in environments with high process disturbance. The case studied is a SES and we want to estimate heave motion at the bow tip. The focus is proper handling of an accelerometer signal, which includes unwanted terms for the heave motion estimation. Remember, the vent valve actuator are going to act accordingly to our estimated signals.

By studying the time series of the two accelerometers, one located at the bow tip and the other at amidships. We have seen that the process disturbance is larger at the former. Our results indicate that it is better to measure the acceleration at amidships, perform heave motion estimation and then transform the motion to the bow tip (D) in order to gain the highest performance.

According to figures 9 and 11, the heave motion estimation works as expected. However, the estimator fails to follow the true state at some points. These points are located at extreme heave positions. In this situation the actuator, that is assumed to act proportionally to the estimated heave motions, might saturate. This leads to a lack of compensation and can justify some of the deviation.

All in all the results are satisfactory and the estimation is usable as input signal for the controller.

Further work involves a study on how the process disturbances affects roll and pitch rates read by the IMU gyroscopes.

REFERENCES

Ø. Auestad, J.T. Gravdahl, A. J. Sørensen, and T. H. Espeland. Simulator and control system design for a free floating surface effect ship at zero vessel speed. *The 2013 IFAC Intelligent Autonomous Vehicles Symposium, Gold Coast (Australia), June 26 - June 28*, 2013.

S. Chakrabarti. *Handbook of Offshore Engineering*. Elsevier, Amsterdam, 2nd edition, 2008.

O. Faltinsen. *Sea Loads on Ships and Offshore Structures*. Cambridge University Press, Cambridge MA, 1993.

T. I. Fossen. *Handbook of Marine Craft Hydrodynamics and Motion Control*. John Wiley & Sons, Ltd, UK, 2011.

T. I. Fossen and T. Perez. Kalman filtering for positioning and heading control of ships and offshore rigs. *IEEE Control Systems Magazine*, 29 (6):32–46, 2009.

J.M. Godhavn. Adaptive tuning of heave filter in motion sensor. *OCEANS Conference Proceedings, Nice (France), September 28 - October 1*, 1:174–178, 1998.

ICSensors. Pressure sensors, accelerometers, and custom microstructures, model 3041. $http://nees.berkeley.edu/Facilities/pdf/Instrumentation/ic\_sensors\_catalog.pdf$, 2013.

Kongsberg. Motion reference unit - mru. `http://www.km.kongsberg.com`, May 15 2013.

S. Küchler, J. Eberharter, K. Langer, K. Schneider, and O. Sawodny. Heave motion estimation of a vessel using accelerometer measurements. *18th IFAC World Congress, Milano (Italy), August 28 - September 2*, pages 14742–14747, 2011.

Qualisys. Oqus camera series. $http://www.qualisys.com/products/hardware/oqus$, 2013.

S. Sabatelli, F. Sechi, L. Fanucci, and A. Rocchi. A sensor fusion algorithm for an integrated angular position estimation with inertial measurement units. *Design, Automation and Test in Europe Conference & Exhibition (DATE), Grenoble (France)*, 2011.

2.3 Conference Paper 3

Ø. F. Auestad, J. T. Gravdahl, A. J. Sørensen, and T. H. Espeland. Motion compensation system for a free floating surface effect ship. In *proceedings of the 19th World Congress of the International Federation of Automatic Control, IFAC, Cape Town, South Africa, August 24-29, 2014*.

Note that the proof of *Remark 1* in this paper is given in Appendix B.

Motion Compensation System for a free floating Surface Effect Ship [⋆]

Øyvind F. Auestad [∗,∗∗] **Jan T. Gravdahl** [∗]
Asgeir J. Sørensen [∗∗∗] **Trygve H. Espeland** [∗∗]

[∗] *Dept. of Eng. Cybernetics, O. S. Bragstads plass D, NTNU, N-7491 Trondheim, Norway; e-mail: oyvind.auestad@itk.ntnu.no*
[∗∗] *Umoe Mandal AS Gismerøyveien 205, N-4515 Mandal, Norway*
[∗∗∗] *Centre for Autonomous Marine Operations (AMOS), Dept. of Marine Technology, Otto Nielsens vei 10, NTNU, N-7491, Trondheim, Norway*

Abstract: This paper deals with vertical motion compensation, or motion damping, on a free-floating Surface Effect Ship (SES) at zero speed. The Motion Compensation System (MCS) works by varying the air cushion pressure of a Surface Effect Ship (SES) to minimize vertical motion due to sea waves. We present a control system which guarantees Global Exponential Stability for the closed-loop state space system and ultimately boundedness for the perturbed system. A study of the performance of the control system is demonstrated through model-test results of a 3 meter long SES.

Keywords: Marine systems, Lyapunov stability, automatic control (closed-loop).

1. INTRODUCTION

1.1 The SES Concept

Surface Effect Ships are known to offer high speed and excellent sea keeping performance in high sea states compared to conventional catamarans. The SES rides on an air cushion which is enclosed by to two catamaran side hulls and flexible rubber seals in the bow and stern end, see fig. 1. A great advantage of SES over a hovercraft, or an Air Cushion Vehicle (ACV), is that the rigid side hulls permit the use of water jet propulsion which enables a high and efficient transit speed. The air cushion is pressurized using a set of lift fans that blow air into the air cushion. The cushion lifts the vessel vertically, and the pressurized air can carry the majority of the vessel weight.

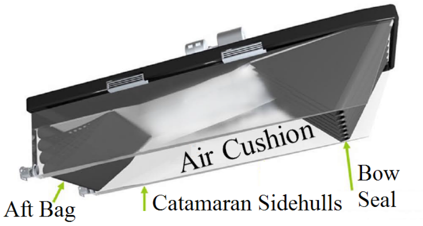

Fig. 1. SES hull, bag and bow seal (photo: Umoe Mandal)

The pressure is indirectly controlled by varying the leakage area A_L out of the air cushion using ventilation valves. By controlling the air flow actuators, a SES at zero speed, can alter its lift force in counter-phase with the sea waves. The controlled air cushion pressure acts as a compensator to the motion set up by sea wave propagations. Hence the control system is called a compensation system.

A comprehensive study on the SES is presented by Butler (1985). More recent literature involves the T-Craft and (Doctors, 2012) which focus on hydrodynamics. Also, Basturk and Krstic (2013) reduces ramp motions between a large, medium-speed, roll-on/roll-off (LMSR) vessel and a SES by controlling the air cushion pressure which resembles the problem formulation of this article.

Modelling and control of the air cushion during transit are covered by Kaplan and Davies (1974) and Sørensen and Egeland (1995).

This paper presents stability analysis and performance properties of the Motion Compensation System (MCS) using experimental model-test results. This document complements Auestad et al. (2013b) which presents mathematical modelling and development of a comprehensive simulator toolbox that captures the dynamics of a SES. Also, simulation of the MCS is presented.

1.2 Motivation

The craft of interest is the Offshore Wind Farm Service Vessel, the UM Wave Craft.

Operation and Maintenance (O&M) costs constitute a sizeable share of an offshore wind farm, in fact, 20% to 30% of the total levelized cost of energy (Musial and Ram, 2010). Decreasing O&M costs includes minimization of maintenance time requirements and maximization of access feasibility (EWEA, 2013).

The Wave Craft, which is a Umoe Mandal high speed craft with speed capability of up to 45 knots is currently

---

[⋆] A special thanks is handed out to Umoe Mandal (UM) for sharing information and being helpful

WAVECRAFT
umoe
SES

Fig. 2. The UM Wave Craft (photo: Umoe Mandal)

under construction. It is a craft with very narrow side hulls. This means that only a small area is exposed to hydrodynamic disturbances which will reduce vertical bow motion. In addition, the craft automatically controls the pressure inside the air cushion to further maximize access feasibility. By utilizing active control of the air cushion pressure to stabilize vertical motion, the vessel is able to dock with offshore wind turbines in higher sea states than possible today.

This docking scheme consists of two phases. In this paper, *Phase One* is studied.

- *Phase One:* Deals with a free-floating SES that uses automatic control to alter the air cushion pressure in order to compensate for motions induced by wave forces. The pressure is controlled in such a way that the vertical motion of the bow tip is minimized. In section 4 (Model Test Results), this is denoted "Bow Pos.". Phase one prepares the vessel for phase two.
- *Phase Two:* In this phase, the captain will allocate sufficient thrust force from the water jets, which will result in a mechanical friction force that will hinge the craft bow rubber fender to the turbine. At this point, the cushion pressure is actively controlled so that the friction force is larger than the excitations force. A paper describing the second phase will be published at a later stage.

1.3 Model Testing

The proposed control system was tested in waves using a 3 meter long model of the Wave Craft. The hull, lift fans, seals and ventilation valves are correctly scaled and modelled to fit the designed full-scale properties. The main dimensions of the craft are given in app. B and the scaling factor is 8.

The paper is organized as follows. Section 2 is about modelling the most important dynamics used for the control system design discussed in section 2.2 and the stability analysis which is discussed in section 3. Section 4 presents experimental model test results and we conclude our work in section 5.

2. CONTROL PLANT MODEL

The mathematical model presented is used for stability analysis. For a more detailed process plant model, suitable for craft simulation, see Auestad et al. (2013b).

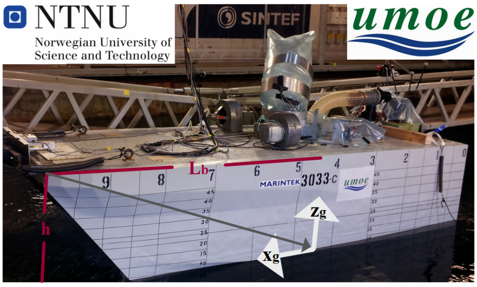

Fig. 3. The picture shows the 3 meter long model test craft of the UM Wave Craft

Equations of motion and cushion pressure dynamics for a SES were first presented by Kaplan and Davies (1974). The equations consider three coupled degrees of freedom, uniform pressure, heave and pitch. A decoupled version of pressure, heave and pitch was presented in Sørensen and Egeland (1995) which forms the basis of this work.

A body-fixed coordinate system is defined according to the right hand rule with the x_g, y_g and z_g-axes oriented positive forwards, to the port and upwards respectively. The origin is located on the mean water plane, under the center of gravity, as illustrated in figure 3. All equations of motion are formulated in this frame. One thing differs from the control plant model presented in Sørensen and Egeland (1995), but is defined in the process plant model in Sørensen (1993):

Assumption 1. A coupling exist between cushion pressure, and pitch velocity.

This assumption is justified by the large variations of cushion pressure that occurs during MCS. The point of attack for the air cushion pressure does not coincide with the hydrodynamic point of attack, which is our origin. The longitudinal distance between these points is denoted x_{cp} and is considered to be too large to neglect.

Translation along the z_g-axis is called heave and denoted η_3, while the rotation angle around the y_g-axis is called pitch and denoted η_5. The remaining degrees of freedom, which are not relevant in this article, includes η_i, where $i = 1, 2, 4$ and 6 which respectively denotes surge, sway, roll and yaw.

The SES dynamics in the vertical plane are modelled as a mass-spring-damper system with sea wave excitation forces and air cushion volume pumping as disturbances.

The following equations (1) - 10) are based on Sørensen (1993). The total pressure inside the air cushion is described as

$$P_c(t) = P_a + P_u(t) \tag{1}$$

where P_a is the atmospheric pressure, and $P_u(t)$ is uniform cushion excess pressure.

The lift fans are assumed to run at constant speed supplying the air cushion with an air inflow $Q_{in}(t)$ which is given according to a linearised fan characteristic. The cushion air outflow $Q_{out}(t)$ varies proportionally to the ventilation valve leakage area A_L defined as

$$A_L(t) = A_{L,Bias} + \Delta A_L(t), \tag{2}$$

where $A_{L,Bias}$ is a certain constant valve opening, allowing controlled area variations (ΔA_L) in both directions. The vessel will reach it's equilibrium state when $\Delta A_L = 0$ and no sea waves are present. In this case, the cushion excess pressure reaches its equilibrium pressure P_0, hence $P_u(t) = P_0$. The system will be linearised about this point.

For modelling purposes, a non-dimensional uniform pressure variation $\mu_u(t)$ is defined according to

$$\mu_u(t) = \frac{P_u(t) - P_0}{P_0} \tag{3}$$

The equations of motion in heave and pitch are written as

$$(m+A_{33})\,\ddot{\eta}_3(t)+B_{33}\,\dot{\eta}_3(t)+C_{33}\,\eta_3(t)-A_c\,P_0\,\mu_u(t) = F_3^e(t), \tag{4}$$

$$\begin{aligned}(I_{55} + A_{55})\ddot{\eta}_5(t) + B_{55}\dot{\eta}_5(t) + C_{55}\eta_5(t) + A_c\,P_0\,x_{cp}\,\mu_u(t)\\ = F_5^e(t),\end{aligned} \tag{5}$$

where m is vessel mass, and I_{55} is the moment of inertia about the body fixed y-axis. A_c is equilibrium air cushion surface-area. Let j = 3,5 respectively denote heave and pitch motions. Then, A_{jj} is hydrodynamic added-mass coefficient, B_{jj} is the water wave radiation damping coefficient and C_{jj} is a hydrostatic coefficient due to buoyancy. F_j^e is the hydrodynamic excitation force acting on the side-hulls.

The hydrodynamic excitation forces in heave and pitch can be expressed as:

$$F_3^e(t) = 2\zeta_a e^{-\kappa\,d}\frac{sin\frac{\kappa\,L}{2}}{\frac{\kappa\,L}{2}}\left(C_{33} - \omega_0^2 A_{33}\right) sin\,\omega_0 t, \tag{6}$$

$$\begin{aligned}F_5^e(t) = 2\zeta_a e^{-\kappa\,d}\Bigg[\left(\frac{1}{\kappa}cos\frac{\kappa\,L}{2} - \frac{2}{\kappa^2\,L}sin\frac{\kappa\,L}{2}\right)\\ \left(C_{33} - \omega_0^2 A_{33}\right)\Bigg] cos\,\omega_0 t\end{aligned} \tag{7}$$

where $\kappa = 2\pi/\lambda$. ζ_a, λ and ω_0 are respectively sea wave elevation amplitude, length and frequency, L is air cushion length, d is the draft of side hulls.

The uniform cushion pressure equation is expressed as:

$$\begin{aligned}K_1\,\dot{\mu}_u(t) + K_3\,\mu_u(t)+\rho_{c0}\,A_c\,\dot{\eta}_3(t) - \rho_{c0}A_c x_{cp}\dot{\eta}_4(t) =\\ K_2\;\Delta A_L(t) + \rho_{c0}\,\dot{V}_0(t),\end{aligned} \tag{8}$$

where:

$$\begin{aligned}K_1 &= \frac{\rho_{c0}\,h_0\,A_c}{\gamma\left(1 + \frac{P_a}{P_0}\right)},\\ K_2 &= \rho_{c0}\,c_n\sqrt{\frac{2P_0}{\rho_a}},\\ K_3 &= \frac{\rho_{c0}}{2}\left(Q_0 - 2\,P_0\,q\frac{\partial Q_{in}}{\partial P}|_0\right),\end{aligned} \tag{9}$$

where h_0, ρ_{c0} respectively denote the height from the waterline to the wet-deck and air density, both at equilibrium cushion pressure. ρ_{c0} can be approximated to ρ_a, air density at ambient conditions. Q_0 is the equilibrium air flow rate, $\frac{\partial Q_{in}}{\partial P}|_0$ is the lift fan characteristic slope at equilibrium point, q is the total number of (identical) lift fans, $\dot{V}_0(t)$ is the rate of wave volume pumping for the dynamic pressure. Volume pumping occur when sea waves are changing the air cushion volume. This results in certain vertical dynamics which can be expressed:

$$\dot{V}_0(t) = A_c\,\zeta_a\,\omega_0\,\frac{sin\frac{\kappa\,L}{2}}{\frac{\kappa\,L}{2}}\,cos(\omega_0 t), \tag{10}$$

where we assume zero craft surge speed.

2.1 State Space System

The LTI, system given in eq. (1) – (10), can be written in standard state space form:

$$\dot{x}(t) = A\,x(t) + B\,u(t) + E\,v(t) \tag{11}$$

where:

$$\begin{aligned}x = \left[\,\eta_3\;\;\eta_5\;\;\dot{\eta}_3\;\;\dot{\eta}_5\;\;\mu_u\,\right]^T_, \quad u = \Delta A_L, \quad v = \left[\,F_3^e\;\;F_5^e\;\;\dot{V}_0\,\right]^T_,\\ A \in \mathbb{R}^{5\times5}_, \quad B \in \mathbb{R}^{5\times1}_,, \quad E \in \mathbb{R}^{3\times5}_,\end{aligned} \tag{12}$$

The measurement signal y is a bandpass filtered numerical integration of an accelerometer located at the bow tip. Using the defined coordinate system, Auestad et al. (2013b) shows that this signal can be written:

$$y(t) = Cx(t) = \dot{\eta}_3 - L_b\dot{\eta}_5, \tag{13}$$

where L_b is the longitudinal length to the bow tip (see fig. 3) from our coordinate origin. Also, $C \in \mathbb{R}^{1\times5}$. All coefficients in the system matrices A, B, C and E have physical meanings and are given in App. A.

2.2 Control System Design

The following singel-input-singel-output, motion compensating, proportional feedback control law is proposed:

$$u(t) = -k\,y(t), \tag{14}$$

where $k > 0$ is the controller gain and k, u and $y \in \mathbb{R}$

3. STABILITY ANALYSIS

By combining (11) - (14) and setting $v = 0$, then the unperturbed closed loop system can be written:

$$\begin{aligned}\dot{x} &= (A - BkC)x\\ &= A_{cl}\,x,\end{aligned} \tag{15}$$

Lemma 1. A_{cl} is hurwitz

Proof: The closed loop system matrix is written:

$$A_{cl} = \begin{bmatrix} 0 & 0 & 1 & 0 & 0\\ 0 & 0 & 0 & 1 & 0\\ -\frac{C_{33}}{A_{33}+m} & 0 & -\frac{B_{33}}{A_{33}+m} & 0 & \frac{A_c P_0}{A_{33}+m}\\ 0 & -\frac{C_{55}}{A_{55}+I_{55}} & 0 & -\frac{B_{55}}{A_{55}+I_{55}} & -\frac{A_c P_0 x_{cp}}{A_{55}+I_{55}}\\ 0 & 0 & \alpha & \beta & -\frac{K_3}{K_1} \end{bmatrix},$$

where $\alpha = -\frac{A_c\rho_{c0}+K_2 k}{K_1}$ and $\beta = \frac{A_c\rho_{c0}x_{cp}+\frac{1}{2}K_2 L_b k}{K_1}$.

Choosing the Lyapunov candidate $V(x)$:

$$V(x) = x^T P x \tag{16}$$

The derivative along the system trajectories of the closed loop system yields:

$$\begin{aligned}\dot{V}(x) &= \dot{x}^T P x + x^T P \dot{x} \\ &= x^T (A_{cl}^T P + P A_{cl}) x \\ &:= -x^T Q x\end{aligned} \tag{17}$$

The Lyapunov equation is defined:

$$P A_{cl}^T + A_{cl} P = -Q \tag{18}$$

For A_{cl} to be Hurwitz, and therefore the equilibrium point $x = 0$ to be globally asymptotic stable (GAS), (18) must be fulfilled and there must exist a P, Q s.t. $P > 0$ and $Q \geq 0$. Since the system is linear we can extend our results and claim global exponential stability (GES) of the origin. Due to the structure of A_{cl} and P, the top left (2×2) corner of Q is forced to zero. Therefore, the invariance principle will be used which will prove that a $Q \geq 0$ results in GAS for the closed loop system defined in (15).

Let $P = diag(p_{ii})$, $Q = diag(q_{ii})$ for $i = 1, 2, ..., 5$.

We choose:

$$p_{11} = p_{33} \frac{C_{33}}{A_{33} + m}, \quad p_{22} = p_{44} \frac{C_{55}}{A_{55} + I_{55}}, \quad p_{55} = 1,$$
$$p_{33} = \frac{(A_{33} + m)(A_c \rho_{c0} + K_2 k)}{A_c K_1 P_0}, \; p_{44} = \frac{K_2 L_b k + A_c \rho_{c0} x_{cp}}{A_c K_1 P_0 x_{cp}} \tag{19}$$

As the top left 2×2 submatrix of A_{cl} is zero, the same will hold for the chosen Q hence $q_{11} = q_{22} = 0$. Then choose:

$$q_{33} = \frac{2\, p_{33}\, B_{33}}{(A_{33} + m)}, \quad q_{44} = 2\, p_{44}\, A_c \rho_{c0} x_{cp}, \quad q_{55} = 2\, p_{55} \frac{K_3}{K_1} \tag{20}$$

It can be seen that the solution for P and Q solves the Lyapunov equation (18). Also, $P > 0$ and $Q \geq 0$ since P and Q are diagonal and all the terms in (19) and (20) are positive due to their physical interpretation.

Using the invariant set theorem we can show GES for the equilibrium $x = x_0$. From (15) and (17) it can be seen that:

$$\begin{aligned}&\dot{V}(x) = 0 \\ &\Downarrow \\ x = x_0 = &[\,\eta_3 \;\; \eta_5 \;\; 0 \;\; 0 \;\; 0\,]^T\end{aligned} \tag{21}$$

However, using the left hand side of (15):

$$\ddot{\eta}_3 = \ddot{\eta}_5 = \dot{\mu}_u = 0, \tag{22}$$

only if

$$\eta_3 = \eta_5 = 0 \tag{23}$$

Hence the equilibrium $x = 0$ is GES for all parametric uncertainties in A, B and C and the result of Lemma 1 follows.

Remark 1. By combining eq. (11) - (14), the perturbed, closed loop system can be written:

$$\dot{x}(t) = A_{cl} x(t) + E v(t) \tag{24}$$

The solution for the perturbed system (24) is uniformly, ultimately bounded by a term b. Hence, $\|x(t)\| \leq b \; \forall x$ according to *Lemma* 9.2 in Khalil (2002).

In addition, by using the results from Lemma 1 and by extending our Lyapunov function, with the perturbed term $(v(t) \neq 0)$, it can be seen that:

$$\dot{V} = -x^T Q x + 2 x^T P E v < 0, \tag{25}$$

if we restrict the disturbance vector v to satisfy the inequality:

$$||v(t)|| < ||T\, x(t)||, \tag{26}$$

where $T = \begin{bmatrix} 0 & 0 & B_{33} & 0 & 0 \\ 0 & 0 & 0 & B_{55} & 0 \\ 0 & 0 & 0 & 0 & \frac{K_3}{\rho_{c0}} \end{bmatrix}$, and the vector norm $|| \bullet ||$ denotes the 1-norm (App. A in Khalil (2002)).

4. MODEL TEST RESULTS

4.1 Setup and Notation

In this section, the experimental setup is described.

- The Main Dimensions for the UM Wave Craft are listed in app. B. The model scale factor is 8.
- All tests are performed either at Marine Cybernetics Laboratory (NTNU) or The Towing Tank, both located at SINTEF, Marintek in Trondheim, Norway.
- The craft includes fully scalable SES equipment such as the Ventilation Valve, Lift Fans, Bag Fan, Stern and Aft seal/Bag.
- The input for the control system is an accelerometer (ICSensors, Model 2041) located midships at the bow tip. A SES experience vibrations in the hull, i.e. process disturbances due to the air cushion dynamics. Auestad et al. (2013a) presents proper handling of the raw accelerometer signal.

Experimental model test results will be shown for regular and irregular seas with the MCS toggled OFF/ON.

The following notations will be used:

- 180° sea: Wave direction from the aft.
- MCS OFF: Constant air cushion leakage, $A_L = A_{L,Bias}$
- MCS ON: The proposed controller varies the cushion leakage, $A_L(t) = A_{L,Bias} + \Delta A_L(t)$
- H_s, T_s denotes wave height $[m]$ and period $[s]$. Definitions of H_s involves:
  - · For regular waves: Peak to peak height
  - · For irregular waves: Mean height of the third highest waves
- Motion Damping $:= 100 \left(1 - \frac{\text{Peak to Peak, MCS ON}}{\text{Peak to Peak, MCS OFF}}\right)$
- Bow Pos.: The translation of the bow tip along the Down axis in the North-East-Down frame. These measurements are given by lab equipment (Qualisys, Oqus Camera Series). Mathematically this can be expressed:

$$BowPos. = cos(\eta_4) cos(\eta_5) \int y dt \tag{27}$$

using Fossen (2011).

4.2 Performance in Regular Waves

In this experiment, the SES encounters regular head sea waves with the MCS toggled OFF and ON. Figure 4 and

5 clearly illustrate the effect of the MCS which is toggled ON at $t = 17s$ and $t = 150s$, respectively.

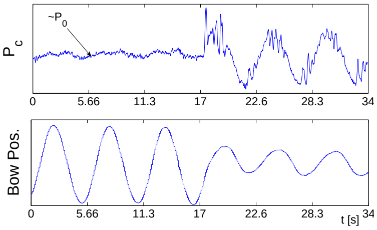

Fig. 4. Head Sea, $H_s = 1.2m$, $T_s = 5.6s$. MCS OFF / ON at $t = 17s$, 68 % Motion Damping

Figure 5 shows the performance of the control system in large long crested waves.

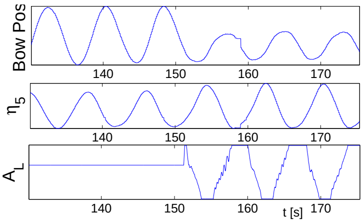

Fig. 5. 135° Sea, $H_s = 2.7m$, $T_s = 8s$. MCS OFF / ON at $t = 151s$, 60 % Motion Damping

4.3 Performance in Irregular Waves

The following model test results illustrates the Power Spectral Density (PSD) for the Bow Pos., see eq. (27).

The duration of each test is approximately an hour with one half MCS ON and one half MCS OFF. The wave spectrum is Jonswap (Fossen, 2011) with $\gamma = 3.3$, $(\sigma_{low}, \sigma_{high}) = (0.007, 0.009)$.

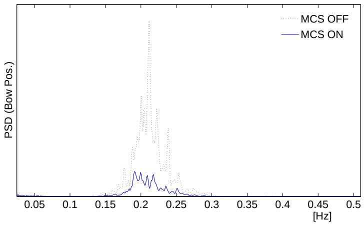

Fig. 6. Head sea, $H_s = 1m$, $T_s = 5s$

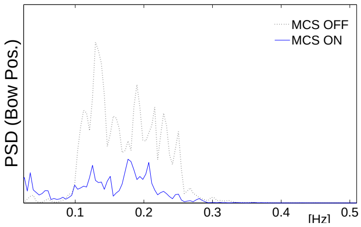

Fig. 11. 135° sea, $H_s = 2m$, $T_s = 7.5s$

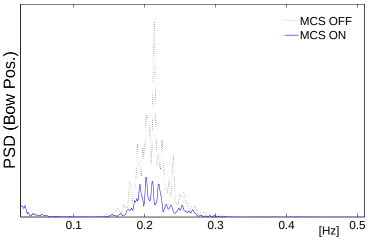

Fig. 7. 45° sea, $H_s = 1m$, $T_s = 5s$

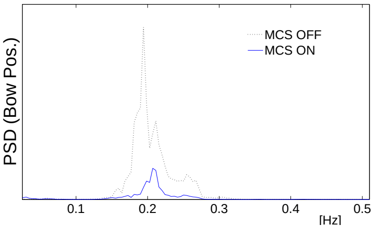

Fig. 8. 135° sea, $H_s = 1m$, $T_s = 5s$

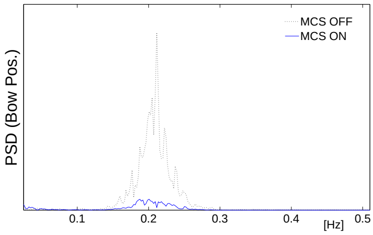

Fig. 9. 180° sea, $H_s = 1m$, $T_s = 5s$

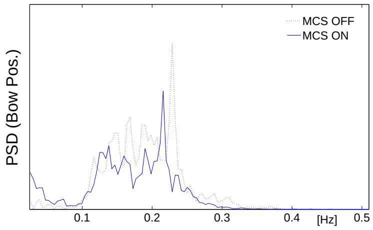

Fig. 10. 90° sea, $H_s = 1.5m$, $T_s = 7s$

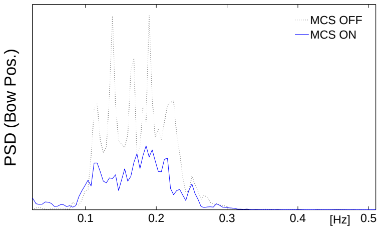

Fig. 12. 45° sea, $H_s = 2.5m$, $T_s = 8s$

The MCS performs best in following seas. A reason for this could be the longitudinal difference in buoyancy. The stern hull has higher buoyancy than the fore part of the hull. For instance, let two sea waves hit the rigid vessel at different time instances, one head sea wave and one following sea wave. Now, it would be reasonable to assume that it is easier to compensate for the vertical position of the bow tip when the wave energy lays on the stern part of the hull instead of on the fore part.

The Power Spectral Density (PSD) plots (fig. 6 - 12) illustrate that the bow tip motions are reduced when the MCS is toggled ON. This is evidently true for all sea wave headings except 90 degree seas, where, as expected, the MCS has small effects since the roll motion are dominating the heave motion in the specific wave period.

Using Kaplan et al. (1981) the uniform pressure resonance is calculated to approximately 1.5 Hz. However, the resonance frequency is not scalable through model testing (Kaplan et al., 1981) and the main reason behind this is the lack of scaling opportunities for P_a. The model test pressure resonance was found to be approximately 10 [Hz], which would correspond to a 3.5 Hz resonance in the full scale domain. However, these high frequencies are not excited at zero surge speed.

5. CONCLUSIONS AND FURTHER WORK

A control system for controlling the vertical position of a Surface Effect Ship at zero vessel speed is presented. The system is named Motion Compensation System (MCS). The stability analysis shows that the non-perturbed, closed loop system is Globally Exponential Stable. The poles of the perturbed closed loop system has strictly negative real values (this proves stable behaviour for any parametric uncertainties using the proposed controller).

The performance of the MCS is illustrated through experimental model testing of a 3 meter long Surface Effect Ship. The performance is presented through time series (figure 4 and 5) and power spectrum density plots (fig. 6 and 12) for regular and irregular seas, respectively. The plots illustrate how the controlled air cushion pressure affects the bow tip motion.

For instance, fig. (6) and (12) illustrate two different waves with two different motion damping ratios, respectively 68% and 60%. This paper successfully illustrates damping of vertical motions of a free floating SES, at zero craft speed, which has not been documented before.

The MCS is not limited to transfer of personnel from a vessel to a wind turbine, it is relevant for every scenario where one wants to control and damp vertical motion at seas. The control point location, which in this case was the bow tip, can easily be changed, even online.

Further work involves work using hybrid control tools when switching between the different phases as explained in section 1.2.

ACKNOWLEDGEMENTS

This work was partly supported by Umoe Mandal and The Research Council of Norway through the Centres of Excellence funding scheme, project number 223254 - AMOS and the Industrial Ph.D. scheme. The model tests were financed by Carbon Trust's Offshore Wind Accelerator program (OWA, 2010)

REFERENCES

Auestad, Ø., Gravdahl, J.T., and Fossen, T.I. (2013a). Heave motion estimation on a craft using a strapdown inertial measurement unit. *The 9th IFAC Conference on Control Applications in Marine Systems (CAMS), Osaka, Japan, 17-20, Sep.*

Auestad, Ø., Gravdahl, J.T., Sørensen, A.J., and Espeland, T.H. (2013b). Simulator and control system design for a free floating surface effect ship at zero vessel speed. *The 2013 IFAC Intelligent Autonomous Vehicles Symposium, Gold Coast, Australia, 26 - 28 June.*

Basturk, H.I. and Krstic, M. (2013). Adaptive wave cancelation by acceleration feedback for ramp-connected air cushion-actuated surface effect ships. *Automatica*, 49(9), 2591–2602.

Butler, E.A. (1985). The surface effect ship. *Naval Engineers Journal*, 97(2), 200–258.

Doctors, L. (2012). Near-field hydrodynamics of a surface-effect ship. *Journal Of Ship Research*, 56(3), 183–196.

EWEA (2013). Deep water - the next step for offshore wind energy. Technical report, European Wind Enery Association, July.

Fossen, T.I. (2011). *Handbook of Marine Craft Hydrodynamics and Motion Control.* John Wiley & Sons, Ltd, UK.

Kaplan, P. and Davies, S. (1974). *A Simplified Representation of the Vertical Plane Dynamics of SES Craft.* AIAA/SNAME Advanced Marine Vehicle Conference.

Kaplan, P.B., Bentson, and Davis, S. (1981). *Dynamics and Hydrodynamics of Surface Effect Ships.* Trans. SNAME VOL 89 1981 page 211 - 247.

Khalil, H.K. (2002). *Nonlinear Systems.* Prentice Hall.

Musial, W. and Ram, B. (2010). *Large-Scale Offshore Wind Power in the United States, p. 116-117.* National Renewable Energy Laboratory.

OWA (2010). Offshore wind accelerator (owa) access competition competition overview and technical specification. *Carbon Trust.*

Sørensen, A.J. (1993). *Modelling and Control of SES Dynamics in the Vertical Plane.* Ph.D. thesis, Department of Engineering Cybernetics, NTNU (Formerly NTH).

Sørensen, A.J. and Egeland, O. (1995). Design of ride control system for surface effect ships using dissipative control. *Automatica*, 31, 183 – 199.

Appendix A. SYMBOLIC MODEL MATRICES

$$A = \begin{bmatrix} 0 & 0 & 1 & 0 & 0 \\ 0 & 0 & 0 & 1 & 0 \\ \frac{-C_{33}}{m+A_{33}} & 0 & \frac{-B_{33}}{m+A_{33}} & 0 & \frac{A_c P_0}{m+A_{33}} \\ 0 & \frac{-C_{55}}{I_{55}+A_{55}} & 0 & \frac{-B_{55}}{I_{55}+A_{55}} & \frac{-A_c\, P_0\, x_{cp}}{I_{55}+A_{55}} \\ 0 & 0 & \frac{-\rho_{c0} A_c}{K_1} & \frac{\rho_{c0}\, A_c\, x_{cp}}{K_1} & \frac{-K_3}{K_1} \end{bmatrix}$$

$$B = \begin{bmatrix} 0 \ 0 \ 0 \ 0 \ \frac{K_2}{K_1} \end{bmatrix}^T \qquad C = [0 \ 0 \ 1 \ -L_b \ 0]$$

Appendix B. MAIN DIMENSIONS

Length/Width over all: 26.6/10.4 m, Draught OFF/ON Cushion: 2.77/0.8 m, Passengers: 12 PAX.

2.4 Conference Paper 4

Ø. F. Auestad, T. Perez, J. T. Gravdahl, A. J. Sørensen, and T. H. Espeland. Boarding Control System - for Improved Accessibility to Offshore Wind Turbines. In *proceedings of the 10th IFAC Conference on Manoeuvring and Control of Marine Craft (MCMC), Copenhagen, Denmark, August 24-26*

Conference paper 4 won the "Best Student Paper" award. However, it is not included in this thesis since all its information is given in the extended journal paper edition given in Section 2.5.

2.5 Journal Paper

Ø. F. Auestad, J. T. Gravdahl, T. Perez, A. J. Sørensen, and T. H. Espeland. Boarding Control System for Improved Accessibility to Offshore Wind Turbines: Full-scale testing. To be published in Control Engineering Practice (CONENGPRAC-D-15-00270), 2015.

Boarding Control System for Improved Accessibility to Offshore Wind Turbines: Full-scale testing

Øyvind F. Auestad[a,c,*], Jan T. Gravdahl[a], Tristan Perez[b], Asgeir J. Sørensen[d], Trygve H. Espeland[c]

[a] *Dept. of Eng. Cybernetics, O. S. Bragstads plass D, NTNU, N-7491 Trondheim, Norway;*
[b] *Inst. for Future Environments and Electrical Eng. & Comp. Science, Queensland Univ. of Tech., Brisbane, Australia*
[c] *Umoe Mandal AS Gismerøyveien 205, N-4515 Mandal, Norway*
[d] *Centre for Autonomous Marine Operations (AMOS), Dept. of Marine Technology, Otto Nielsens vei 10, NTNU, N-7491, Trondheim, Norway*

Abstract

This paper considers the dynamic modelling and motion control of a Surface Effect Ship (SES) for safer transfer of personnel and equipment from vessel to-and-from an offshore wind-turbine. The control system designed is referred to as Boarding Control System (BCS). The performance of this system is investigated for a specific wind-farm service vessel—The Wave Craft. On a SES, the pressurized air cushion supports the majority of the weight of the vessel. The control problem considered relates to the actuation of the pressure such that wave-induced vessel motions are minimized. Results are given through simulation, model- and full -scale experimental testing.

Keywords: Compensating feedback, Marine systems, Ship control, Velocity control, Pressure control, Friction, SES

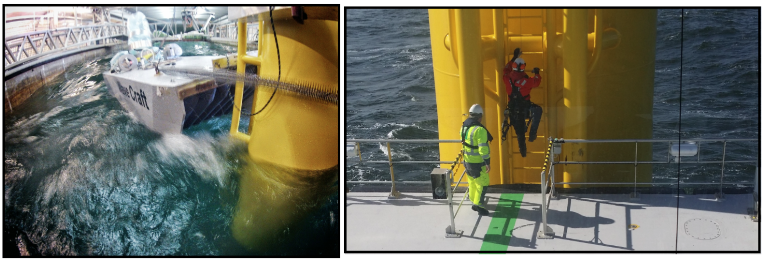

Figure 1: The Wave Craft model-test and prototype in BCS mode. Courtesy of Umoe Mandal (UM).

---

[*] Corresponding Author: Tel.: +4747615615. Email address: oyvind.auestad@itk.ntnu.no

Preprint submitted to Journal of Control Engineering Practice *September 17, 2015*

1. Introduction

1.1. A growing market for offshore wind-farms

As reported by the European Environment Agency's EEA [1], it is expected that in 2020 there will be 30-40 times the installed offshore-wind infrastructure developed in 2008. Fig. 2 illustrates that the installation of offshore wind-turbines in Europe is currently increasing.

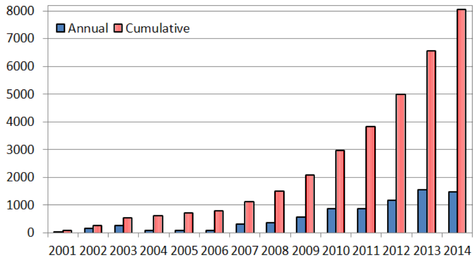

Figure 2: Annual and cumulative installations of offshore wind capacity - adapted from [2]

The next generation of turbines are located significantly further offshore. Therefore, they experience higher sea states, which require specialized service vessels for operation and maintenance (O&M) [3]. Fig. 1 shows the model- and full-scale version of the vessel studied in this paper. A key issue for good economics on an offshore wind farm is the maximization of access feasibility for O&M. The majority of the Crew Transfer Vessels (CTV's) are accessing the turbine using propulsion-thrust which sticks the bow fender to a turbine ladder. Surface Effect Ship (SES) equipped with the Boarding Control System (BCS), which is introduced in this paper, increases the annual dates where turbine access is possible while significantly decreasing sea-sickness incidents. The BCS leads to safer personnel transfer in higher seas than what is possible today and it is an enabling technology for O&M of offshore wind-energy infrastructure.

Today, the offshore wind marked for CTV's is dominated by catamarans [4, 5]. They offer transfer speed up to $25 - 27$kn, turbine accessibility is usually possible in up to $1.5 - 1.75$m significant wave height (Hs) and the typical vessel lengths are $18 - 27$m. The SWATH (Small-waterplane-area twin hull) is becoming more and more popular as the structure of the hull minimizes the hydrodynamic contact area, making them capable of withstanding rougher sea conditions than the catamaran design. However they suffer from lower transit speeds.

A two-modality vessel model is presented to account for the vessel's free motion and motion whilst in contact with a wind-turbine. A mathematical model is developed and stability properties for the BCS are investigated. Based on modelling and experimental validation (for data corresponding to the British North Sea), we estimate that a like-sized SES equipped with the BCS can enable safe turbine access in sea states up to 2.5m Hs and at least 3.2m for long-crested seas which is higher than the competing CTV's. After being in operation for 5 months and counting, the captains onboard the Wave Craft series prototype, *Umoe Ventus* reports that there hasn't been a single event where the bow fender have slipped the turbine. As a side note, the maximum speed of the vessel is in excess of 40kn and it got a minimum draft of 1.1m.

1.2. Surface effect ships

SES are known to offer very high speed and excellent sea keeping performance in high seas compared to conventional, equally-sized, catamarans. The SES rides on an air cushion which is enclosed by two rigid catamaran side-hulls and flexible rubber seals at the bow and the stern. Fig. 3 shows a cut view along the longitudinal center-plane of a typical SES. The air cushion is pressurized by centrifugal lift fans that

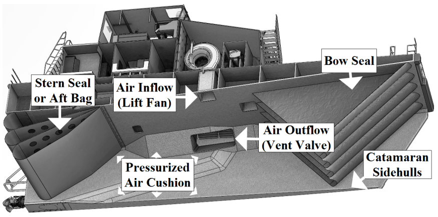

Figure 3: A typical SES. Illustration by Umoe Mandal.

blow air into the cushion. The air cushion lifts the vessel vertically and the pressurized cushion can support up to 80% of the total vessel weight. When this is the case, only a minor part of the hull is submerged and exposed to hydrodynamic drag. Two comprehensive work on the SES are given by Butler [6] Lavis [7].

The pressure is controlled by controlling the position of a set of vent valves that varies the cushion air leakage. This can alter the crafts submerged level considerably (2m on a 26m long Wave Craft). To obtain high performance during turbine boarding, a Wave Craft has installed twice the air-flow actuation capacity necessary for traditional SES high-speed mode. This is the consequence of the BCS needing to transfer large amount of air for each wave in order to achieve crucial vertical motion damping. Fig. 4 shows a model-test boarding setup.

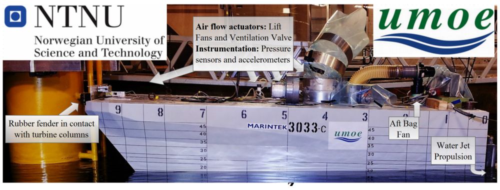
NTNU
Norwegian University of Science and Technology
Air flow actuators: Lift Fans and Ventilation Valve
Instrumentation: Pressure sensors and accelerometers
umoe
Rubber fender in contact with turbine columns
MARINTEK 3033-C
Aft Bag Fan
Water Jet Propulsion

Figure 4: The Wave Craft model test. Courtesy of Umoe Mandal.

1.3. Air cushion control for SES

The modern SES was invented in the 60s and Maritime Dynamics, Inc (MDI) developed the first functional, performing Ride Control System (RCS) which defines cushion pressure control during transit. The RCS damps wave-induced pressure fluctuations in the air cushion which reduce vertical accelerations and hence, increases passenger comfort. The U.S. Navy lead the development of the modern SES by launching the *XR-1* series, the *SES-100A* and the *SES-100B*, all with some form of RCS installed. The latter one, which was a 100-ton craft, established a sustained speed record of 91.9 knots [6]. MDI proceeded from their early success and dominated the industrial manufacture of the RCS for the SES. Air cushion pressure control is traditionally performed using vent valves, as seen in Fig. 5, located between the cushion and ambient air.

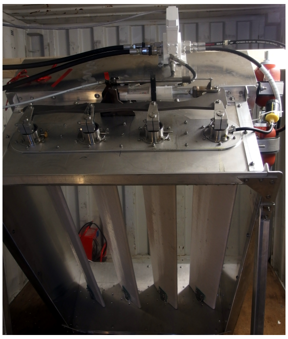

Figure 5: A vent valve assembly from a full-scale system bench-test. Courtesy of Umoe Mandal.

Kaplan et al. [8] and Adams et al. [9] present two comprehensive contributions to SES modelling and RCS design. Sørensen and Egeland [10] identified and solved certain spatial varying air cushion pressure resonances, using a set of partial differential equations, robust dissipative control and collocation principles. Later, Bertin et al. [11] proposed a decoupled high-gain controller which through simulation claims higher performance for damping of the lowest spatial varying resonance frequency.

A traditional RCS will mainly strive to neglect higher-frequency (> 0.5Hz) pressure variations during transit. An almost inverse control-scheme has appeared popular in the literature the past few years where wave-frequency (< 0.3 Hz) pressure variations in fact are desired to counter motions set up by sea waves at zero vessel speed. Basturk and Krstic [12] propose adaptive wave cancellation by controlling the air cushion pressure of a SES. The SES is ramp-connected to a large, medium-speed, roll-on/roll-off (LMSR) vessel. The controller acts to reduce the ramp motions. Auestad et al. [13, 14] also presents vertical motion damping on a SES, but the craft does not experience any external forces such as ramps or turbine contact.

The main scientific contribution in this paper is to present the breakthrough in heave and pitch damping, at low speeds on a SES. This article is an extended work of what was published in Auestad et al. [15] and includes a more extensive study, a stability investigation and full-scale results. Section 2 and 3 presents a mathematical vessel model and control system design. Section 4 presents simulation and experimental results while the work is concluded in section 5.

2. Mathematical Modelling

In this section, a mathematical model is developed that accounts for both free-floating stationkeeping and stationkeeping whilst the vessel bow is in contact with the wind-turbine column. A nomenclature can be found in Appendix C.

2.1. Modelling hypotheses

The following are the modelling hypotheses considered:

1. Vessel motion in surge, heave and pitch. The wind-turbine column is considered vertical and rigid.
2. With reference to Fig. 6, as a point of reference on the vessel, consider the point B fixed to the vessel which is located below the center-of-gravity on the mean water line. The surge and heave displacements at point B are considered with respect to the point O in an inertial (i) earth-frame, namely $x^i_{B/O}$ and $z^i_{B/O}$. The upper right script indicate the coordinate system used and the lower scripts indicate the reference points to which these offsets refer to.
3. The compliance of the point of contact between vessel and turbine is modelled by a vertical and a horizontal spring-damper, k_v, c_v, k_h and c_h, respectively. The spring system- captures the elasticity of the bow rubber fender and -can slide up and down the turbine column, see Fig. 4 and 6. When it slides, the contact is represented by a small mass m_*—which is considered in order to avoid computational causality issues due to holonomic constraints. The location of m_* is represented by the point M. M is fixed in x-direction, but variable in z-direction. Fig. 6 illustrates when no contact exists between vessel and turbine.
4. The point C is located at the bow tip on the craft's centerline. The offsets $x^b_{C/B}$ and $z^b_{C/B}$ indicate the fixed distance between point C and B in body-fixed coordinates.
5. Let the point O be chosen so that it coincide with B when the vessel is thrusting towards the turbine with the bollard pull force (K_{BP}). Consequently, the horizontal spring is compressed. Note that the point O is fixed in space while B is fixed to the vessel. When turbine contact isn't present, it is assumed that the model, with the chosen coordinate frame, is valid given that the bow is arbitrarily close to the turbine. This is illustrated in Fig. 6. Hence, the model covers both in- and not in- turbine contact mode.

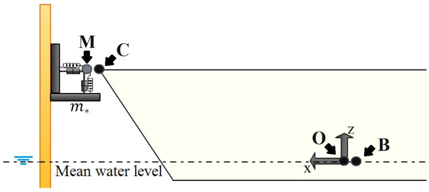

Figure 6: Uncompressed horizontal spring - no contact.

6. The horizontal spring produces force (X^i_s) only when it is in compression which is when $x^i_{C/O} > x^i_{M/O}$, see Fig. 7. When this is the case, the vertical spring force Z^i_s, can act both in compression and tension.

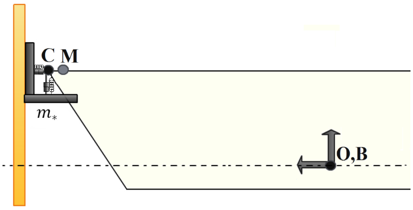

Figure 7: Compressed horizontal spring - turbine contact.

7. During boarding operation, when contact is present, the bow ($z^i_{C/O}$) can either be fixed to, or slide up and down the wind-turbine column. This is regarded as stick-slip motion and is modelled as Coulomb friction force.
   The stick motion relates to the static regime. When the applied wave force is large enough to overcome static friction, the bow will move either up or down and the system enters the kinetic regime. To account for this, the following modes are considered
   (a) Static friction, with coefficient μ_s, prevails if the mass m_* is fixed to the turbine, hence $\dot{z}^i_{M/O} = 0$.
   (b) Kinetic friction, with coefficient μ_k prevails if m_* glides up and down the wind turbine column, hence $\dot{z}^i_{M/O} \neq 0$.

2.2. Spring forces

The pitch angle is referred to as $\theta(t)$ and is defined positive with the bow down according to the right-hand rule. The inertial coordinates for the point C can be expressed using a rotation matrix according to

$$r^i_{C/O} = r^i_{B/O} + R^i_b r^b_{C/B}$$
$$\Downarrow$$
$$\begin{bmatrix} x^i_{C/O} \\ 0 \\ z^i_{C/O} \end{bmatrix} = \begin{bmatrix} x^i_{B/O} \\ 0 \\ z^i_{B/O} \end{bmatrix} + \begin{bmatrix} \cos(\theta) & 0 & \sin(\theta) \\ 0 & 1 & 0 \\ -\sin(\theta) & 0 & \cos(\theta) \end{bmatrix} \begin{bmatrix} x^b_{C/B} \\ 0 \\ z^b_{C/B} \end{bmatrix} \tag{1}$$

The horizontal spring force, in inertial coordinates, can be expressed

$$X^i_s = \begin{cases} k_h(x^i_{M/O} - x^i_{C/O}) - c_h \dot{x}^i_{C/O} & \text{if } (*) \\ 0 & \text{otherwise.} \end{cases}, \tag{2}$$

where $(*)$ represent the following statement $x^i_{C/O} \geq x^i_{M/O}$. According to hypothesis 2, $X^i_s < 0$ during craft-to-turbine contact. The vertical spring force in inertial coordinates is expressed

$$Z^i_s = k_v(z^i_{M/O} - z^i_{C/O}) + c_v(\dot{z}^i_{M/O} - \dot{z}^i_{C/O}). \tag{3}$$

2.3. The friction force

The friction force between the small mass m_* and the turbine column is modelled as follows

$$Z^i_f = \begin{cases} Z^i_s & \text{if } (**) \\ \mu_k X^i_s \,\mathrm{sgn}(\dot{z}^i_{M/O}) & \text{else.} \end{cases}, \tag{4}$$

where $(**)$ represent the following friction switching statement

$$|\dot{z}^i_{M/O}| < \epsilon \text{ and } |Z^i_s| \leq -\mu_s X^i_s. \tag{5}$$

When (5) is true then static friction force applies and the bow sticks to the turbine. When false, kinetic friction applies. The parameter ϵ is chosen sufficiently small to avoid simulation scattering and $\mathrm{sgn}(\cdot)$ denotes the signum function. Recall that $X^i_s \leq 0$ so the friction force will always act against the motion and act as a stabilizer and damping of motion. Observe that a discontinuity occurs when toggling the regimes.

The equation of motion for the fictitious mass m_*, can be written

$$m_* \ddot{z}^i_{M/O} = Z^i_f - Z^i_s. \tag{6}$$

Due to equation (3), (4) and (6), the point M coincide with C when turbine-contact is not present, hence $z^i_{M/O} = z^i_{C/O}$.

2.4. Decomposing the propulsion force

The propulsion forces are modelled in the inertial frame as

$$\begin{aligned} X^i_{prop} &= K_{BP}\cos(\theta), \\ Z^i_{prop} &= -K_{BP}\sin(\theta), \\ M^i_{prop} &= \frac{-L}{2} K_{BP}\sin(\theta), \end{aligned} \tag{7}$$

where $K_{BP} > 0$ is the propulsion bollard pull force. It is assumed that the propulsion force coincides with the water plane for $\theta = 0$. L denotes the air cushion length.

2.5. Air cushion pressure dynamics

The following notation and modelling of the air cushion is based on [10]. Let $P_u(t)+P_a$ denote the total air cushion pressure, where P_a and $P_u(t)$ denotes the atmospheric and the excess air cushion pressure, respectively.

For control purposes, $\mu_u(t)$ is defined as a uniform, non-dimensional dynamic cushion pressure variable according to

$$\mu_u(t) = \frac{P_u(t) - P_0}{P_0}, \tag{8}$$

where P_0 denotes the equilibrium pressure.

$\Delta A_L(t)$ is the controller output and denotes the commanded dynamic leakage-area of the air cushion. The total leakage is expressed

$$A_L(t) = A_0 + \Delta A_L(t), \tag{9}$$

where A_0 is some mean operating value that allows two-sided control. In the absence of sea waves, the system reach its equilibrium point when $\Delta A_L(t) = 0$.

The dynamics for μ_u given in [10] is written as follows

$$\begin{aligned} K_1\,\dot{\mu}_u(t) + K_3\,\mu_u(t) + \rho_{c0}A_c\dot{z}^i_{B/O}(t)& \\ -\rho_{c0}A_c x_{cp}\dot{\theta}(t) &= K_2\;\Delta A_L(t) + \rho_{c0}\,\dot{V}_0(t), \end{aligned} \tag{10}$$

with

$$\begin{aligned} K_1 &= \frac{\rho_{c0}\,h_0\,A_c}{\gamma\left(1+\frac{P_a}{P_0}\right)},\; K_2 = \rho_{c0}\,c_n\sqrt{\frac{2P_0}{\rho_a}}, \\ K_3 &= \frac{\rho_{c0}}{2}\left(Q_0 - 2\,P_0\,q\frac{\partial Q_{in}}{\partial P}|_0\right), \end{aligned} \tag{11}$$

where ρ_a, ρ_{c0} and A_c denotes ambient air density, equilibrium cushion density and air cushion area, x_{cp} denotes the longitudinal length between the inertial coordinate frame origin and the center of the air cushion pressure, Q_0 is the equilibrium air flow, $\frac{\partial Q_{in}}{\partial P}|_0$ is the linearised lift fan characteristic slope at the equilibrium point, which is always negative. The parameter q denotes the total number of lift fans that are running at the same constant speed.

$\dot{V}_0$ is the sea wave volume pumping of the dynamic pressure. It is regarded a disturbance to the air cushion since it represents compressed pressure waves induced by encountered sea waves. $\dot{V}_0$ is modelled as follows

$$\dot{V}_0(t) = A_c\,\zeta_a\,\omega_0\,\frac{\sin\frac{\kappa\,L}{2}}{\frac{\kappa\,L}{2}}\,\cos(\omega_0 t), \tag{12}$$

where ζ_a and ω_0 denotes the wave height amplitude and sea wave frequency. $\kappa = \frac{2\pi}{\lambda}$ denotes the wave number where λ is the sea wave length.

The cushion pressure dynamics is linearised about P_0 which is found reasonable for the control plant model by investigating the actual nonlinear air-flow actuators response from zero to maximum air cushion pressure in Fig. 8. The upper limit of the cushion pressure is limited due to leakage under the seals and hulls, which denies a further increase for P_u as the cushion air outflow (Q_{out}) equals the fan inflow (Q_{in}). The characteristics for Q_{in} is found from the lift-fan characteristic table from the Wave Craft and the air-flow out of the air cushion is expressed according to

$$Q_{out} = c_n A_L(t)\sqrt{\frac{2P_u(t)}{\rho_a}} \tag{13}$$

Fig. 8 illustrates that for the control plant model, a linearised flow approach around P_0 is considered applicable.

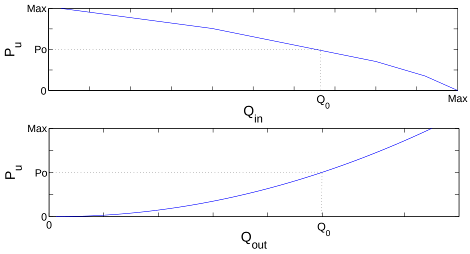

Figure 8: Leakage air-flow characteristics.

2.6. Motion in surge, pitch and heave

The vessel motion in surge, pitch and heave consist of standard seakeeping equations of motion with radiation and wave excitation forces. The restoring forces are considered linear, following assumption 7.1 in [16], for low-speed applications. The same symbolic notation is also used.

The equations of motion are coupled with cushion pressure, spring forces and friction forces. A hydrostatic coupling between heave and pitch is neglected due to the chosen coordinate frame. The air cushion pressure is coupled with heave and pitch velocity. The modelling presented in this paper assumes regular (long-crested) head seas. The following control plant model is considered, where the surge dynamics can be expressed as

$$\begin{aligned}(m+A_{11})\,\ddot{x}^i_{B/O}(t)+B_{11}\,\dot{x}^i_{B/O}(t)&=X^i_{prop}(t)\\ &+X^i_s(t)+X^i_{waves}(t),\end{aligned}\tag{14}$$

and the motion in heave can be written as,

$$\begin{aligned}(m+A_{33})\,\ddot{z}^i_{B/O}(t)+B_{33}\,\dot{z}^i_{B/O}(t)+C_{33}\,z^i_{B/O}(t)\\ -A_c\,P_0\,\mu_u(t)=Z^i_{prop}(t)+Z^i_s(t)+Z^i_{waves}(t),\end{aligned}\tag{15}$$

while the pitch equation is given by

$$\begin{aligned}(I_{yy}+A_{55})\ddot{\theta}(t)+B_{55}\dot{\theta}(t)+C_{55}\theta(t)+x_{cp}A_cP_0\mu_u(t)\\ =M^i_{prop}(t)+z^b_{C/B}X^i_s(t)-x^b_{C/B}Z^i_s(t)+M^i_{waves}(t),\end{aligned}\tag{16}$$

where A_{ii}, B_{ii} and C_{ii} denotes the hydrodynamic added-mass-, water wave radiation- and hydrostatic coefficient in motion ii where $i = 1, 3, 5$ respectively denoting motion in surge, heave and pitch. Added mass and radiation terms are frequency-dependent but are solved as coefficients using the Cumming equation [17], [16]. m and I_{yy} denotes vessel mass and moment of inertia around the y-axis. X^i_{waves}, Z^i_{waves} and M^i_{waves} are the hydrodynamic wave excitation forces in surge, heave and pitch, respectively, and models for these can be found in [17] and [16].

3. Control System Design

The control problem considered consist of minimizing the vertical craft motion by controlling the air cushion pressure. The pressure is not actuated directly but through varying the leakage area out of a set of vent valves as illustrated in equation (9), (10) and Fig. 5.

3.1. State space model

The system, expressed in equation (1) through (16) can be written in the following state space form

$$\begin{aligned}\dot{\mathbf{x}}(t)&=\mathbf{A}\mathbf{x}(t)+\mathbf{B}u(t)+\mathbf{f}(\mathbf{x}(t))+\mathbf{E}\mathbf{v}(t)\\ y(t)&=\mathbf{C}\mathbf{x}(t),\end{aligned}\tag{17}$$

where $\mathbf{x}\in\mathbb{R}^9$ and $\mathbf{v}\in\mathbb{R}^4$. $\mathbf{A}\mathbf{x}(t)$ captures the unperturbed and uncontrolled (BCS off) dynamics of the craft when bow-to-turbine contact is not present. In addition, $\mathbf{f}(\mathbf{x}(t))$ captures the dynamics of the bow-to-turbine-contact forces which include water jet-propulsion, spring- and friction-forces. $\mathbf{B}u(t)$ and $\mathbf{E}\mathbf{v}(t)$ is the control force and disturbance force, respectively.

Momenta, cushion pressure and displacement will be used as states in a 9-dimensional state space vector $\mathbf{x} = [x_1\ x_2\ ...\ x_9]^T$, where

x_1 : Heave displacement, $z^i_{B/O}$
x_2 : Pitch angle, θ
x_3 : Heave momentum, $(m + A_{33})\dot{z}^i_{B/O}$
x_4 : Pitch angular momentum, $(I_{yy} + A_{55})\dot{\theta}$
x_5 : Dynamic cushion pressure, $\mu_u(t)$
x_6 : Surge displacement, $x^i_{B/O}$
x_7 : Displacement of mass m_*, $z^i_{M/O}$
x_8 : Surge momentum, $(m + A_{11})\dot{x}^i_{B/O}$
x_9 : Vertical momentum of mass m_*, $m_*\dot{z}^i_{M/O}$

The scalar control is defined as $u(t) := \Delta A_L(t)$. Note that a positive u correspond to a total leakage area less than A_0 (9) and vice versa. The measurement is the sum of two numerical integrated acceleration signals. The accelerometers are located at point B and C (Fig. 6). Assuming $\theta < 10°$, the measurement can be mathematically expressed as $y(t) = k_B\dot{z}^i_{B/O} + k_c(\dot{z}^i_{B/O} - x^b_{C/B}\dot{\theta})$ where k_b and k_c are non-negative scaling parameters which weights the input from the sensor located at point B and C respectively. The initial state is

$x(t_0) = [\mathbf{0}_{1x6}\ z^b_{C/O}\ \mathbf{0}_{1x2}]$, where $\mathbf{0}_{nxm}$ is the $n \times m$-dimensional zero matrix. The disturbance vector is expressed $\mathbf{v} = [Z^i_{waves}\ M^i_{waves}\ \dot{V}_0\ X^i_{waves}]^T$.

The system matrices $\mathbf{A} \in \mathbb{R}^{9\times9}$, $\mathbf{B} \in \mathbb{R}^{9\times1}$, $\mathbf{f}(\mathbf{x}) \in \mathbb{R}^{9\times1}$, $\mathbf{E} \in \mathbb{R}^{9\times4}$ and $\mathbf{C} \in \mathbb{R}^{1\times9}$ can be found in Appendix C.

3.2. Feedback control law

The following feedback controller is proposed

$$\begin{aligned} u(t) &= -ky(t) \\ &= -k\,\mathbf{C}\,\mathbf{x}(t), \end{aligned} \tag{18}$$

where $k \in \mathbb{R}$ is the controller feedback gain and tuned in experiments by reducing the root mean square (rms) value for the two accelerometer signals.

Analysis and testing of controllers with different structure were conducted in simulation including full-state information for benchmarking. Through this analysis, it was found that the control law (18) provided not only the greatest simplicity, but also best performance. This control law injects damping into the system since it is proportional to the motion rates. The physical implementation of (18) is done by using two accelerometers located at point B and C on the vessel as illustrated in Fig. 6. They two accelerometer signals, both acting vertically, are numerically integrated and filtered separately, weighted (k_B and k_C) and then added together as illustrated in Fig. 9.

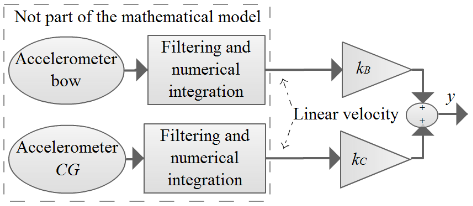
Not part of the mathematical model
Accelerometer bow
Filtering and numerical integration
k_B
Linear velocity
+
+
y
Accelerometer CG
Filtering and numerical integration
k_C

Figure 9: The measurement signal y.

Due to the air cushion dynamics, accelerometers on a SES measure hull vibrations above the control bandwidth, -as well as traditional measurement noise. Therefore, consideration must be taken into account when performing signal processing. In this article it is assumed that a numerical integrator exist with anti-windup logic. It is assumed that the accelerometer signals are properly band-pass filtered in such a way that the -3 dB corner frequency eliminates sensor drift, removes- and assure stability in all structural and resonance modes but at the same time does not induce significant phase lag at the relevant sea wave frequencies. Signal- filtering and -estimation on a SES is further discussed in [18].

The controller will manipulate the cushion pressure by adjusting the leakage area to counteract and reduce vertical motions. When toggling the BCS on/off, the air cushion pressure amplitude is either decreased or increased. For instance, if the BCS is initially turned off, and a certain sea state is inducing a large $\dot{V}_0$ then large cushion pressure variations are inducing vessel motion. Consequently, when the BCS is turned on, the pressure variations are decreased leading to decreased vessel motion. This is illustrated in Fig. 11a.

In contrast, if the hydrodynamic excitation forces (Z^i_{waves} and M^i_{waves}) are dominating and inducing vessel motion, typically at longer wave periods, the BCS will increase the cushion pressure amplitude to counteract the sea wave. In this case, the BCS can be seen upon as a heave-and-pitch compensator. This case is illustrated in Fig. 11b.

3.3. Stability investigation

This section will investigate the stability of the closed loop system when no contact exists between vessel and turbine. The following will classify the convergence of point B to O, see Fig. 6. The unperturbed dynamics that describes the non-turbine-contact is described as

$$\dot{\mathbf{x}} = \mathbf{A}\mathbf{x} + \mathbf{B}u. \tag{19}$$

State x_6 to x_9 includes surge motion and vertical motion of the fictitious spring suspension. These states are not relevant for the non-contact case. Therefore, in this section, $\mathbf{A}, \mathbf{B}, \mathbf{C}$ are reduced to $\mathbf{A1}_{5x5} \in \mathbb{R}^{5\times5}$, $\mathbf{B1}_{5x1} \in \mathbb{R}^{5\times1}$ and $\mathbf{C1}_{1x5} \in \mathbb{R}^{1\times5}$ which captures heave, pitch and cushion pressure dynamics while excluding the surge and spring suspension dynamics. See equation (C.3). Therefore, define $\tilde{\mathbf{x}} := [x_1\ x_2\ ...\ x_5]^T$ which are the first five states in $\mathbf{x}$. Let $\tilde{\mathbf{x}}_0$ denote the equilibrium of $\tilde{\mathbf{x}}$. The closed loop system can be written

$$\begin{aligned}\dot{\tilde{\mathbf{x}}} &= \mathbf{A1}_{5x5}\,\tilde{\mathbf{x}} + \mathbf{B1}_{5x1}\,u \\ &= (\mathbf{A1}_{5x5} - \mathbf{B1}_{5x1}\,k\,\mathbf{C1}_{1x5})\,\tilde{\mathbf{x}} \\ &:= \mathbf{A1}_{cl}\,\tilde{\mathbf{x}},\end{aligned} \tag{20}$$

where $\mathbf{A1}_{cl} \in \mathbb{R}^{5\times 5}$. When no contact exists between the vessel and the turbine, the system will be Globally Exponential Stable (GES) if $\mathbf{A1}_{cl}$ is Hurwitz since (20) is linear.

Lemma 1. $\mathbf{A1}_{cl}$ *is Hurwitz.*

Proof: By choosing the following Lyapunov candidate

$$\mathbf{V}(\tilde{\mathbf{x}}) = \tilde{\mathbf{x}}^T\mathbf{P}\tilde{\mathbf{x}}, \tag{21}$$

where $\mathbf{Q}, \mathbf{P} \in \mathbb{R}^{5\times 5}$, then the derivative along the system trajectories of (21) can be written according to

$$\dot{\mathbf{V}}(\tilde{\mathbf{x}}) = -\tilde{\mathbf{x}}^T\mathbf{Q}\tilde{\mathbf{x}}, \tag{22}$$

where $\mathbf{Q} \in \mathbb{R}^5$ needs to satisfy the Lyapunov equation:

$$\mathbf{P}\mathbf{A1}_{cl}^T + \mathbf{A1}_{cl}\mathbf{P} = -\mathbf{Q}. \tag{23}$$

Let's choose $\mathbf{P}$ and $\mathbf{Q}$ as two diagonal matrices with the following terms on the main diagonal ($p_1\ p_2\ ...\ p_5$) and ($q_1\ q_2\ ...\ q_5$), respectively.

A solution of (23) can be found as

$$\begin{aligned}p_1 &= \frac{C_{33}(I_{yy}+A_{55})(A_c\rho_{c0}+K_2k(k_B+k_C))}{A_cP_0(A_c\rho_{c0}x_{cp}+K_2\,k\,k_C\,x_{CB})} \\ p_2 &= \frac{C_{55}(I_{yy}+A_{55})}{A_cP_0x_{cp}},\ p_3 = \frac{p_1}{C_{33}(m+A_{33})}, \\ p_4 &= \frac{p_2}{C_{55}(I_{yy}+A_{55})},\ p_5 = \frac{K_1(I_{yy}+A_{55})}{A_c\rho_{c0}x_{cp}+K_2k_Ckx_{CB}},\end{aligned} \tag{24}$$

$$\begin{aligned}q_1 &= q_2 = 0,\quad q_3 = \frac{2B_{33}p_1}{C_{33}(m+A_{33})^2}, \\ q_4 &= \frac{2B_{55}p_2}{C_{55}(I_{yy}+A_{55})^2},\quad q_5 = \frac{2K_3p_5}{K_1}\end{aligned} \tag{25}$$

Since all the terms are positive due to their physical interpretation, $\mathbf{P} > 0$ and $\mathbf{Q} \geq 0$.

According to Vidyasagar [19] it can be shown that $\mathbf{A1}_{cl}$ is Hurwitz for a semi-definite $\mathbf{Q}$ by using the invariant set theorem. By solving equation (22) for zero,

$$\dot{\mathbf{V}}(\tilde{\mathbf{x}}) = 0, \tag{26}$$

and due to the structure of $\mathbf{Q}$ one can only be sure that the three latter terms in $\tilde{\mathbf{x}}$ must be zero, not necessarily the first two. Hence,

$$\tilde{\mathbf{x}} = \tilde{\mathbf{x}}_0 = \left[\begin{array}{ccccc} x_1 & x_2 & 0 & 0 & 0\end{array}\right]^T. \tag{27}$$

However, it can be seen from (20) that

$$\ddot{x}_3 = \ddot{x}_4 = \ddot{x}_5 = 0, \tag{28}$$

only if

$$x_1 = x_2 = 0 \tag{29}$$

Therefore, the result of Lemma 1 follows and the state vector $\tilde{\mathbf{x}}$ converges exponentially fast to $\tilde{\mathbf{x}}_0$. Numerical parametric uncertainties are not an issue in $\mathbf{A1}_{cl}$ since the analysis is performed using symbolic terms that are positive due to their physical interpretation.

Remark 1 Stability properties of the perturbed system will now be discussed. Again, by removing the in-turbine-contact dynamics, hence using the first 5 states of $\mathbf{x}$, then the corresponding disturbance vector $\tilde{\mathbf{v}} \in \mathbb{R}^3$ is written

$$\tilde{\mathbf{v}} = [Z^i_{waves}\ M^i_{waves}\ \dot{V}_0]^T. \tag{30}$$

By including the perturbation term, the closed loop system can be written as follows

$$\dot{\tilde{\mathbf{x}}} = \mathbf{A1}_{cl}\,\tilde{\mathbf{x}} + \mathbf{E1}_{5\times 3}\tilde{\mathbf{v}} \tag{31}$$

where $\mathbf{E1}_{5\times 3} \in \mathbb{R}^{5\times 3}$ and given in Appendix C. By using the same Lyapunov candidate as given in (21) the corresponding perturbed Lyapunov derivative is given by

$$\dot{V} = -\tilde{\mathbf{x}}^T\mathbf{Q}\,\tilde{\mathbf{x}} + 2\,\tilde{\mathbf{x}}^T\mathbf{P}\mathbf{E1}_{5\times 3}\tilde{\mathbf{v}}, \tag{32}$$

where $\mathbf{P}$ and $\mathbf{Q}$ are given in (24) and (25). Assuming that the disturbances are bounded such that $||\mathbf{E1}_{5\times3}\tilde{\mathbf{v}}|| < \zeta \;\forall\; t$, where ζ is some positive constant it can be shown, using the same argument as in theorem 4.8 in Khalil [20] that the perturbed system is ultimately bounded.

Remark 2 The complete closed loop state space system given in 17 and (18) includes friction force (4), spring force (2), (3) and propulsion force (7). The friction force will act in the opposite direction of any motion, the spring-damper forces will have a reducing effect on the overall motion and the propulsion force is thrusting towards a fixed structure. Based on this, a stable behaviour for the bow-to-turbine case is expected.

4. Results

In the following results, a controller has been designed as specified in section 3. The results are normalized for the purpose of generality (with Fig. 17 as an exception). It is the motion reduction ratio of the BCS that is the main interest of this work.

4.1. Simulation results

Fig. 10 illustrate the dynamics that occur when accessing a wind turbine.

Fig. 10 illustrates a test run that consists of three phases. The craft (point C) is initially located in front of the turbine (point M) and no contact exists. The propulsion force, which initially is zero, is enabled at $t = 33$ s. At this time turbine contact is engaged. The BCS is active from $t = 66$s.

The regular head sea wave has peak-to-peak wave height 2.4m and period 7.16s. The simulation can be summed up as follows:

Phase 1, $t \in (0, 33)$: The horizontal spring is uncompressed. The fictitious spring suspension follows the bow tip, hence $z^i_{M/O} = z^i_{C/O}$.

Phase 2, $t \in (33, 66)$: The propulsion force is thrusting the bow tip ($x^i_{C/O}$) towards the turbine, however, kinetic and static friction are fighting each other, leading the bow tip ($z^i_{C/O}$) to glide up and down the turbine. θ is damped due to friction.

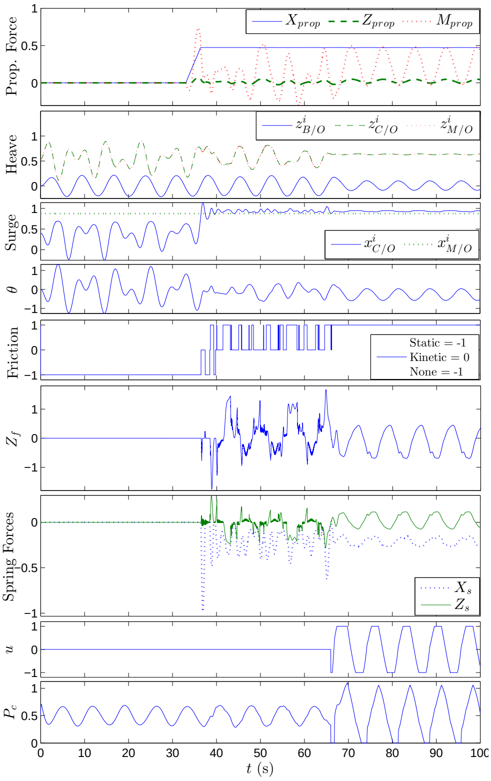

Figure 10: Simulation run with three phases. The label on the y-axes describe the corresponding signal

Phase 3, $t \in (66, 100)$: The BCS is activated while maintaining the propulsion trust force from phase 2. The amplitude of θ and $z^i_{B/O}$ indicates that motions in the entire vessel are significantly reduced. The friction force type are exclusively static and turbine access is safe since $z^i_{C/O}$ is fixed. The control system ensures that the system trajectories return to an equilibrium ($z^i_{C/O} \approx 0.6$).

4.2. Model-test craft

This section is divided into two parts, one for regular (long-crested) waves, and one for irregular seas which is defined by a wave spectrum with distributed wave heights and periods. In both cases, turbine contact is present and the friction alters between the static and kinetic regime. The model-test setup is described in Appendix B.

4.2.1. Regular seas:

Fig. 11 shows that the bow vessel tip is fixed to the turbine when the BCS is on while the bow slips up and down when it is off (uncontrolled system).

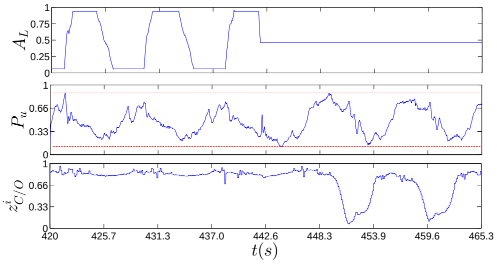

(a) $T_p = 8.5$s. BCS is turned *off* at $t = 441$s.

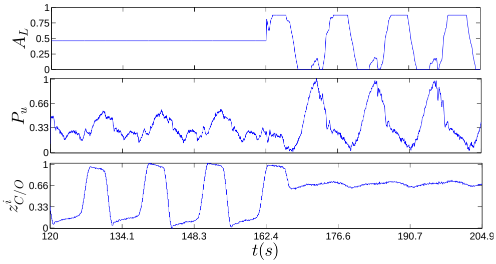

(b) $T_p = 11.7$s. BCS is turned *on* at $t = 162$s.

Figure 11: Model-scale time series. Wave height = 3.2m.

The peak-to-peak wave height is 3.2m. In Fig. 11a, the wave period (T_p) is 8.5s while it is 11.7s in Fig. 11b.

4.2.2. Irregular seas:

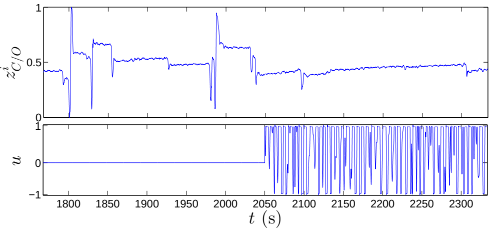

Figure 12: Time series of the bow motion with and without the BCS active. BCS is turned on at $t = 2050$s.

In this section, the parameters H_s and T_p denote significant wave height and wave period, respectively. In this case, the model-tank wave-generator produces a JONSWAP wave spectrum [16] parametrized with $H_s = 2.5$ m and $T_p = 7.5$ s.

Fig. 12 and 13 show the performance of the BCS in irregular seas by reducing bow motions which enables safe turbine access in higher sea states.

Fig. 12 shows the time series of a ten minute run, while Fig. 13 illustrates the Power Spectral Density (PSD) plot, obtained by the MATLAB function pwelch, for a 40 minute run.

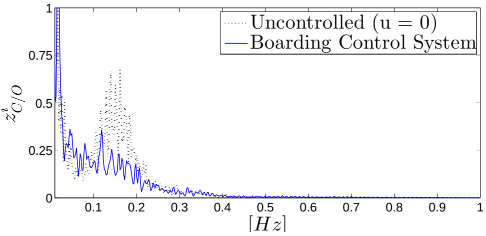

Figure 13: PSD figure of the bow motion with and without the BCS active.

4.3. Full-scale craft

The Wave Craft prototype, Umoe Ventus is currently charted too Dong Energy on the wind-farm Borkum Riffgrund 1 (March 2015), in the Germany's North Sea. The results presented in this article are taken on-site during the BCS tuning period.

The following figures shows the performance of the BCS in significant wave heights $H_s = 1.5$ - 1.8m with wave period around $T_p = 4 - 5$s.

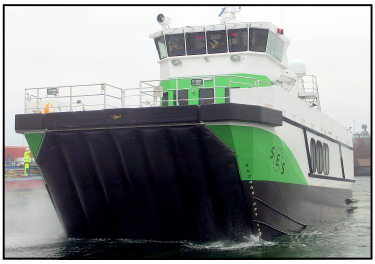

Figure 14: Wave Craft Prototype - Umoe Ventus, by courtesy of Umoe Mandal.

4.3.1. No turbine contact

These results show the performance of the vessel's free floating motion before turbine contact occur.

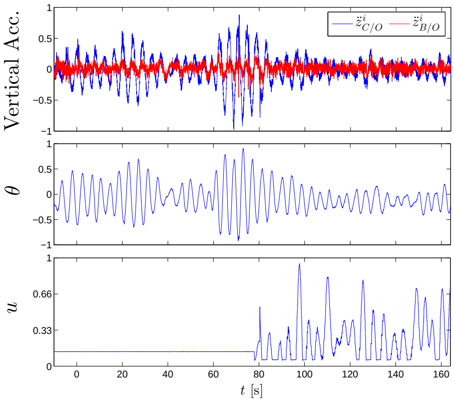

Figure 15: Time series for BCS performance, no turbine contact. Upper: vertical acceleration, middle: pitch angle, lower: controller output. The BCS is turned on at $t = 79$s.

The critical part in this phase is for the captain to smoothly maneuver the vessel into a hinged mode without slamming into the turbine or get the bow tip fender hanging with the nose too far up or too far down. Therefore, reducing pitch motion is crucial. The BCS is also used while loitering in the farm. Fig. 15 proves that the BCS greatly reduce motions.

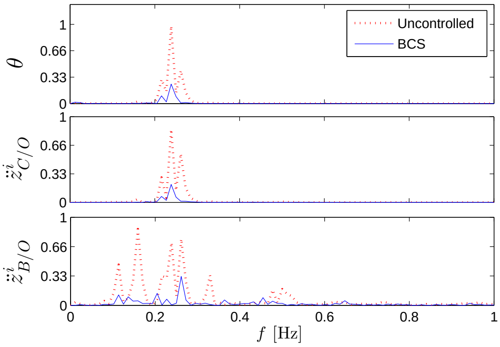

Figure 16: PSD curves showing BCS performance, no turbine contact. Upper: pitch angle, middle and lower: acceleration in bow- and CG, respectively.

Fig. 16 illustrates the same data but represented using three PSD curves. The curves proves a distinct reduction in vertical acceleration and pitch when the BCS is active. According to ISO 2631-1:1997 [21], Fig.17 proves that in these sea conditions, the serviceworkers are not going to get seasick even when operating at the farm for 8 hours. The CG accelerometer ($\ddot{z}^i_{B/O}$) is located directly underneath the serviceworkers cabin and the data is compared to the ISO-standard which deals with the criteria for seasickness.

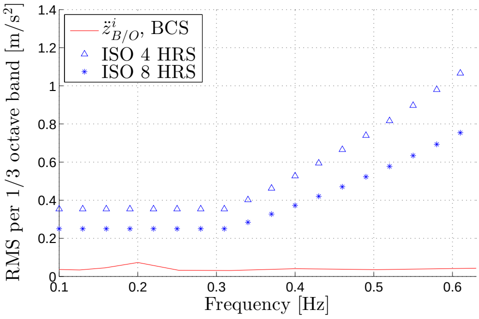

Figure 17: ISO 2631/3 (1997) Seasickness criterion.

4.3.2. Turbine contact

In this section, turbine contact is investigated. Fig. 18 shows that a slip occur for the uncontrolled case at $t = 120$s. This can be seen as θ suddenly changes its mean value.

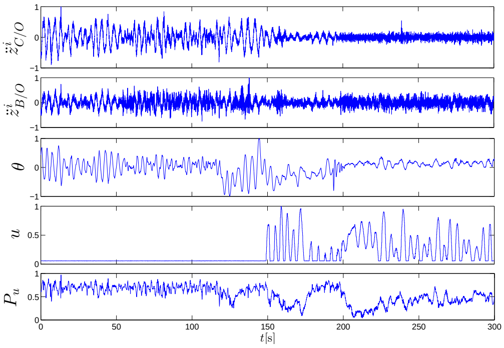

Figure 18: BCS performance, turbine contact, time series for vertical acceleration, pitch, controller output and cushion pressure.

Fig. 19 shows the PSD figure for heave acceleration, while Fig. 20 shows the PSD figure for the pitch angle, both using the time series given in Fig. 18.

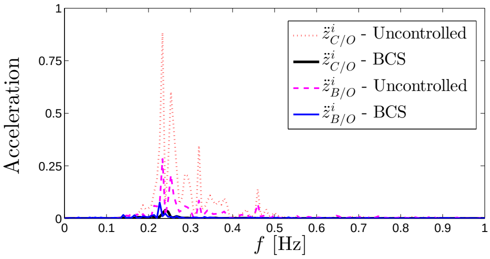

Figure 19: BCS performance, turbine contact, PSD figure for vertical acceleration.

Vertical accelerations are heavily reduced when the BCS is active ($t > 150$s). The system provides a safe boarding environment by sticking the fender to the turbine. Note that when the BCS is toggled on, θ, and hence $z^i_{C/O}$, slowly wanders and converges to its equilibrium point around $t = 200$s. The low frequencies ($< 0.05Hz$) seen in the figures for θ, u and P_u is a direct result of this wandering phenomena and crucial for maintaining a safe boarding environment.

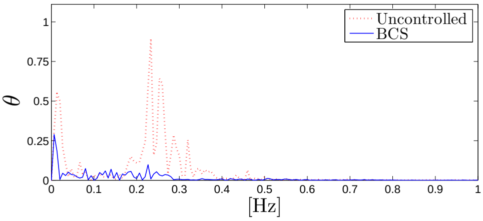

Figure 20: BCS performance, turbine contact, PSD figure for pitch.

5. Conclusions

The performance of the proposed BCS showed that wind-turbine accessibility was increased compared to the uncontrolled case. The results proved that the BCS decreased overall vessel motions and reduced the chance of getting seasick. The model-test results in Fig. 11 indicated safer turbine access in up to 3.2 meter for regular waves and up to 2.5 m significant for irregular waves (Fig. 12 and 13). Also, these results highly affected the decision to construct two full-scale vessel.

The full-scale results were in correspondence with simulation and model-test results. The BCS decrease pitch and heave motion significantly. Several factors apply when safely accessing a turbine, not just the vertical wave propagations as discussed in this article. The speed and direction of wind and current have proved itself crucial to this matter. In fact: the ability to access the turbines has to this point, not been limited by the wave induced vertical motions when the BCS is turned on. At certain events due to the wind and current forces, the CTV ('s) were forced to abort O&M mission and return to harbor. This was the case when the data for Fig. 15 - 17 was obtained. Therefore, to truly identify the potential of the BCS, testing in $2-3$m Hs seas is required, where the uncontrollable, horizontal effects such as current and wind are not dominating. The SES with the BCS have not yet been tried out at the wind-farm during sea waves exceeding 2m Hs, but up to this limit, not a single turbine slip has occurred.

The mathematical modelling presented in this article is not limited to wind-turbine-docking, it captures all types of docking toward offshore structures as long as propulsion force create contact between the bow and the structure. To deal with other type of vessels, one can easily remove the air cushion pressure dynamics.

Acknowledgement

A special thanks to Umoe Mandal and Island Engineering for sharing information and being very helpful. The model-tests was sponsored by *Regionale forskningsfond Agder*, the *Research Council of Norway (RCN)* and *Carbon Trust's Offshore Wind Accelerator (OWA)*. Thanks to the captains on Umoe Ventus (Valling Ship Management). This work was partly supported by the RCN through the Centres of Excellence funding scheme, project number 223254 AMOS, and in part by AFOSR grants FA9550-12-1-0127 and FA9550-15-1-0155.

References

[1] EEA, Offshore wind energy: Action needed to deliver on the energy policy objectives for 2020 and beyond, European Environment Agency Nov (2008).

[2] EWEA, The european offshore wind industry - key trends and statistics 2014, Tech. rep., European Wind Energy Association, January (2015).

[3] OWA, Offshore wind accelerator access competition - shortlisted designs (2014). URL `http://www.carbontrust.com/media/105306/owa-access-innovators.pdf`

[4] J. Bard, F. Thalemann, Offshore infrastructure: Ports and vessels, A report of the Offshore Renewable Energy Conversion platforms - Coordination Action ORECCA.

[5] OWA, Offshore wind accelerator (owa) access competition - overview and technical specification (2010). URL `http://www.engr.mun.ca/~bveitch/courses/IntroNavArch/Assignments/SOR%20-%20OWA.pdf`

[6] E.A. Butler, The surface effect ship, Naval Engineers Journal 97 (1985) 200–258.

[7] D. Lavis, Forty-plus years of hovercraft development, in: Proceedings of the 25th, Canadian Air Cushion Technology Society: CACTS '98, Canadian Aeronautics and Space Institute, 1998.

[8] P.B. Kaplan, Bentson, S. Davis, Dynamics and Hydrodynamics of Surface Effect Ships, SNAMET Transaction Volume 89, 1981.

[9] J.D. Adams, A.W. Ernest, J. Lewis, Design, Development and Testing of a Ride Control System for the XR-ID Surface Effect Ship; Part I - Classical Control, Maritime Dynamics, Inc., Tacoma, Washington, 98422., 1983.

[10] A.J. Sørensen, O. Egeland, Design of ride control system for surface effect ships using dissipative control, Automatica 31 (1995) 183 – 199.

[11] D. Bertin, S. Bittanti, S.M. Savaresi, Decoupled cushion control in ride control systems for air cushion catamarans, Control Engineering Practice 8 (2000) 191–203.

[12] H.I. Basturk, M. Krstic, Adaptive wave cancelation by acceleration feedback for ramp-connected air cushion-actuated surface effect ships, Automatica 49 (2013) 2591–2602.

[13] Ø.F. Auestad, J.T. Gravdahl, A.J. Sørensen, T.H. Espeland, Simulator and control system design for a free floating surface effect ship at zero vessel speed, in: Proceedings of the 8th IFAC Symposium on Intelligent Autonomous Vehicle, Gold Coast, Australia, 26-28 June, 2013.

[14] Ø.F. Auestad, J.T. Gravdahl, A.J. Sørensen, T.H. Espeland, Motion compensation system for a free floating surface effect ship, in: Proceedings

of the 19th World Congress of the International Federation of Automatic Control, IFAC, Cape Town, South Africa, August 24-29, 2014.

[15] Ø.F. Auestad, T. Perez, J.T. Gravdahl, A.J. Sørensen, T.H. Espeland, Boarding control system - for improved accessibility to offshore wind turbines, in: Proceedings of the 10th IFAC Conference on Manoeuvring and Control of Marine Craft (MCMC), IFAC, Copenhagen, Denmark, August 24-26, 2015.

[16] T.I. Fossen, Handbook of Marine Craft Hydrodynamics and Motion Control, John Wiley & Sons, Ltd, UK, 2011.

[17] O. Faltinsen, Sea Loads on Ships and Offshore Structures, Cambridge University Press, 1990.

[18] Ø.F. Auestad, J.T. Gravdahl, T.I. Fossen, Heave motion estimation on a craft using a strapdown inertial measurement unit., in: Proceedings of the 9th IFAC Conference on Control Applications in Marine System, Osaka, Japan, September 17-20, 2013.

[19] M. Vidyasagar, Nonlinear System Analysis, 2nd Edition. Prentice Hall, Englewood Cliffs, NJ, US, 1993.

[20] H.K. Khalil, Nonlinear Systems, Prentice Hall, 2002.

[21] Iso 2631-1:1997 mechanical vibration and shock evaluation of human exposure to whole body vibration., International Standards Organization, Switzerland (1997).

Appendix A. Main Dimensions

Description	**Full-scale**	**Model-test**
Length Over All	26.6m	3m
Width Over All	10.4m	1.3m
Draught (On-cushion)	3.1(1.1)m	0.39(0.14)m
Cargo Capacity	4T	7.8kg
Transit Speed	40+kn	14.1+kn
Range	700Nm	n.a.
Crew	$2-3$	n.a.
Passengers	12	n.a.

Appendix B. Model-scale test setup

The quantitative dimensions of the hull, seals, lift fans and the ventilation valve are accurately scaled. The measurements are obtained by an accelerometer (ICSensors, Model 3022, +/- 2g) located near CG and air cushion pressure sensors (Measurement Specialties, MS1451) which are distributed longitudinally along the cushion. Inertial positions in 6-degrees of freedom given in the North East Down (NED) frame, are available through high speed motion capture cameras (Qualisys, Oqus 3+). Waves were generated using wave makers (AWACS, delivered by DHI). Two springs, each tensioned to represent a Kamewa 45A3 water-jet. All tests were performed in the Ship Model Tank, Sintef, Marintek in Trondheim.

Appendix C. Symbolic Matrices and Nomenclature

The symbolic matrices for the state space system is written accordingly

$$\mathbf{A} = \begin{bmatrix} \mathbf{A1}_{5x5} & \mathbf{0}_{5x4} \\ \mathbf{0}_{4x5} & \mathbf{0}_{4x4} \end{bmatrix} \mathbf{f}(\mathbf{x}) = \begin{bmatrix} \mathbf{0}_{2x1} \\ \mathbf{f1}_{2x1} \\ \mathbf{0}_{3x1} \\ \mathbf{f2}_{2x1} \end{bmatrix} \mathbf{B} = \begin{bmatrix} \mathbf{B1}_{5x1} \\ \mathbf{0}_{4x1} \end{bmatrix} \tag{C.1}$$

$$\mathbf{E} = \begin{bmatrix} \mathbf{E1}_{5x3} & \mathbf{0}_{5x1} \\ \mathbf{0}_{2x3} & \mathbf{0}_{2x1} \\ \mathbf{0}_{1x3} & 1 \\ \mathbf{0}_{1x3} & 0 \end{bmatrix} \mathbf{C} = \begin{bmatrix} \mathbf{C1}_{1x5} & \mathbf{0}_{1x4} \end{bmatrix}, \tag{C.2}$$

where $\mathbf{I}_{nxm}$ denotes the nxm-dimensional identity matrix. Furthermore,

$$\mathbf{A1_{5x5}} =$$

$$\begin{bmatrix} 0 & 0 & \frac{1}{m+A_{33}} & 0 & 0 \\ 0 & 0 & 0 & \frac{1}{I_{yy}+A_{55}} & 0 \\ -C_{33} & 0 & \frac{-B_{33}}{m+A_{33}} & 0 & A_c P_0 \\ 0 & -C_{55} & 0 & \frac{-B_{55}}{I_{yy}+A_{55}} & -x_{cp} A_c P_0 \\ 0 & 0 & \frac{-\rho_{c0} A_c}{K_1(m+A_{33})} & \frac{x_{cp}\rho_{c0} A_c}{K_1(I_{yy}+A_{55})} & \frac{-K_3}{K_1} \end{bmatrix}$$

$$\mathbf{E1}_{5x3} = \begin{bmatrix} \mathbf{0}_{2x2} & \mathbf{0}_{2x1} \\ \mathbf{I}_{2x2} & \mathbf{0}_{2x1} \\ \mathbf{0}_{1x2} & \frac{\rho_{c0}}{K_1} \end{bmatrix} \mathbf{B1}_{5x1} = \begin{bmatrix} 0 & 0 & 0 & 0 & \frac{K_2}{K_1} \end{bmatrix}^T$$

$$\mathbf{C1}_{1x5} = \begin{bmatrix} 0 & 0 & \frac{k_B+k_C}{m+A_{33}} & \frac{-k_C x^b_{C/B}}{I_{yy}+A_{55}} & 0 \end{bmatrix}. \tag{C.3}$$

The nonlinear spring- and friction forces are expressed

$$\begin{aligned} \mathbf{f1_{2x1}} &= \begin{bmatrix} -K_{BP}\sin(x_2) + Z^i_s \\ -\frac{K_{BP} L \sin(x_2)}{2} + z^b_{C/B} X^i_s - x^b_{C/B} Z^i_s \end{bmatrix} \\ \mathbf{f2_{2x1}} &= \begin{bmatrix} K_{BP}\cos(x_2) + X^i_s \\ Z^i_f - Z^i_s \end{bmatrix}, \end{aligned} \tag{C.4}$$

where the spring forces are expressed

$$\begin{aligned} X^i_s &= k_h \left(x^i_{M/O} - x_6 - \alpha \right) - c_h \left(\frac{x_8}{m + A_{11}} + \frac{\beta x_4}{I_{yy} + A_{55}} \right) \\ Z^i_s &= \\ & k_v \left(x_7 - x_1 - \beta \right) + c_v \left(\frac{x_9}{m_*} - \frac{x_3}{m + A_{33}} + \frac{\alpha x_4}{I_{yy} + A_{55}} \right). \end{aligned} \tag{C.5}$$

The switching criteria between kinetic and static friction is written

$$Z^i_f = \begin{cases} Z^i_s & \text{if } |\frac{x_9}{m_*}| < \epsilon \text{ and } |Z^i_s| \leq -\mu_s X^i_s \\ \mu_k X^i_s \operatorname{sgn}(\frac{x_9}{m_*}) & \text{else,} \end{cases} \tag{C.6}$$

where

$$\begin{aligned} \alpha = \alpha(x_2) &= x^b_{C/B}\cos(x_2) + z^b_{C/B}\sin(x_2), \\ \beta = \beta(x_2) &= -x^b_{C/B}\sin(x_2) + z^b_{C/B}\cos(x_2). \end{aligned} \tag{C.7}$$

Nomenclature

$\Delta A_L(t)$	Commanded dynamic cushion leakage area
$\dot{V}_0(t)$	Air cushion wave volume pumping
γ	Heat capacity ratio for air
κ	Sea wave number
μ_s, μ_k	Static- and kinetic-friction coefficient respectively, between turbine and spring suspension (bow fender)
$\mu_u(t)$	Uniform dynamic cushion excess pressure
ρ_{c0}, ρ_a	Air cushion- and ambient-density, respectively
$\theta(t)$	Pitch angle
ζ_a, ω_0	Sea wave amplitude and period, respectively
A_0	Equilibrium cushion leakage area
A_c	Air cushion area
$A_L(t)$	Total cushion leakage area
A_{ii}, B_{ii}	Hydrodynamic terms, $i \in \{1, 3, 5\}$
c_n	Orifice coefficient for vent valve duct shape
c_v, c_h	Damper coefficients for the vertical- and horizontal-spring system, respectively
C_{ii}	Hydrostatic terms, $i \in \{1, 3, 5\}$
h_0, L	Height- and length-of air cushion, respectively
k_v, k_h	Spring coefficients for the vertical- and horizontal-spring system, respectively
K_{BP}	Bollard pull
m, I_{55}	Vessel mass and moment of inertia, respectively
$M^i_{prop}(t)$	Propulsion moment in pitch
$M^i_{waves}(t)$	Sea wave excitation moment in pitch
m_*	Fictitious mass of the spring suspension
P_0	Equilibrium air cushion excess pressure
P_a	Atmospheric pressure
$P_u(t)$	Uniform air cushion excess pressure
q	The number of (identical) lift fans
Q_0	Equilibrium air cushion air flow
Q_{in}	Air flow into the cushion from one lift fan
Q_{out}	Total air flow out from the air cushion
$x^b_{C/B}$	Offsets in x-direction between the bow and below CG (point B)
$X^i_s(t)$	Spring force in surge
$x^i_{B/O}(t)$	Surge displacement
$x^i_{C/O}(t)$	Surge displacement of the bow tip
$x^i_{M/O}(t)$	Surge displacement of the spring
$X^i_{prop}(t)$	Propulsion force in surge
$X^i_{waves}(t)$	Sea wave excitation force in surge
x_{cp}	Longitudinal length between CG and center of pressure
$z^b_{C/B}$	Offsets in z-direction between the bow and below CG (point B)
$Z^i_f(t)$	Friction force between turbine column and spring suspension (bow fender)
$Z^i_s(t)$	Spring force in heave
$z^i_{B/O}(t)$	Heave displacement
$z^i_{C/O}(t)$	Heave displacement of the bow tip
$z^i_{M/O}(t)$	Heave displacement of the spring
$Z^i_{prop}(t)$	Propulsion force in heave
$Z^i_{waves}(t)$	Sea wave excitation force in heave

Chapter 3

Full-scale Experiments

> The boarding mode (BCS) is very useful especially when operating in weather conditions where the wave period exceeds app. 4 seconds. The boarding mode eliminates pitching significantly and makes the turbine-boardings much more safe and calm.
>
> ---
>
> Kresten Hjelm Pedersen, captain and master at Umoe Ventus

> Normally, I usually get sea-sick after approximately 3 hours onboard these service vessels, today after 7 hours in moderate seas, on-board Umoe Ventus, I feel absolutely fine!
>
> ---
>
> Said-Massud Sahiby, turbine-service-personnel, Dong Energy

> Why is there so little motions on this vessel?
>
> ---
>
> James Flahrety, turbine-service-personnel, Dong Energy

> On Umoe Ventus, I can work on my laptop during transfer and during waiting time at the wind-farm, in contrast to other like-sized wind-farm service vessels.
>
> ---
>
> Miro Rodyk, turbine-service-personnel, Dong Energy (Editor: Comparing motions with the present sea conditions)

.

Figures 3.1 and 3.2 illustrates the 27.2m long full-scale vessel with cushion ratio $l/b = 2.5$. Appendix A presents the vessel's main characteristics and general information.

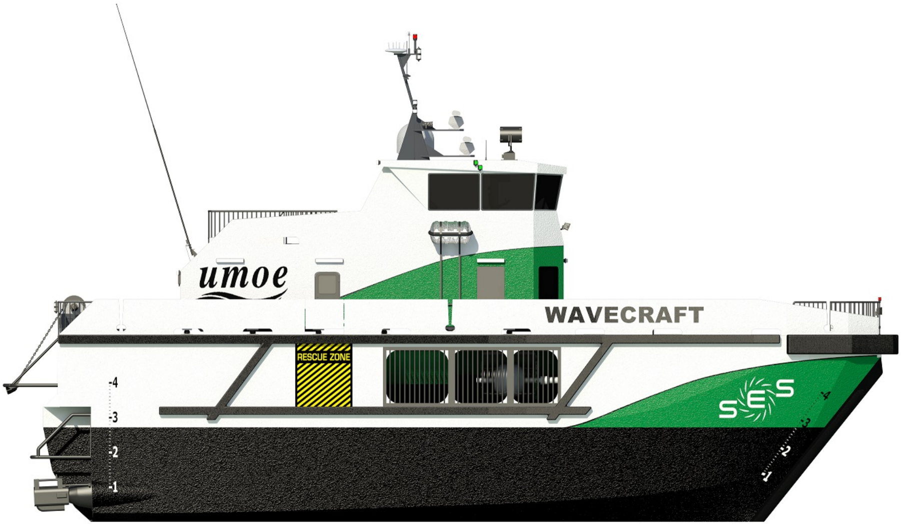
umoe
WAVECRAFT
RESCUE ZONE
SES
-4
-3
-2
-1

Figure 3.1: A computer model of Umoe Ventus shown from the side, by courtesy of Umoe Mandal.

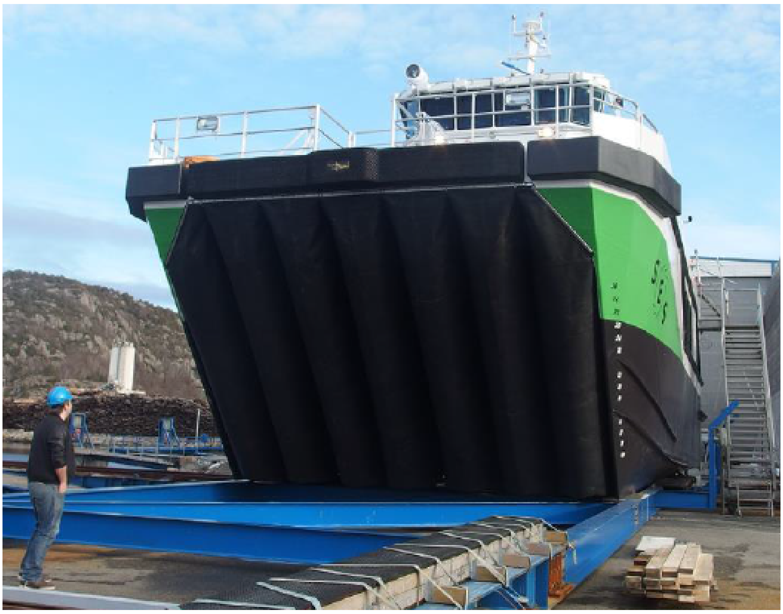

Figure 3.2: The Wave Craft prototype seen from the front. The bow skirt is visible. Photo: Umoe Mandal.

The control hierarchy for performing air cushion pressure control consist of an inner- and an outer-loop. A mixed block- and a signal flow -diagram is shown in Fig. 3.3. The input of the outer loop control law is y. The outer loop control law, which is synonymous to the BCS, provides the inner-loop with a commanded vent valve position signal (u). It is up to the inner loop control law to assure that the actual vent valve cylinder position (y_s) converge to the command. The inner loop is only discussed in Section 3.1 while the remaining sections of this chapter deals with the outer-loop system. The papers given in Chapter 2 deals with signal processing and the outer-loop exclusively.

As a side note, a third 'most-inner loop' exists inside the control valve manifold. The 'control valve', or 'servo valve', inputs a commanded spool position signal and regulates the actual spool position accordingly. The spool position distributes (pressurized) hydraulic oil to flow from the control valve manifold port A, B or a combination of them both, to a hydraulic cylinder. This ultimately moves the cylinder rod and the mechanically coupled vent valves louvers. This is the fundamental theory behind the interaction of a traditional electro-hydraulic servo valve and cylinder.

Section 3.2 presents full-scale measurements of the BCS which is implemented and tested on the Wave Craft prototype. All full-scale control system hardware and instrumentation are delivered by Island Engineering.

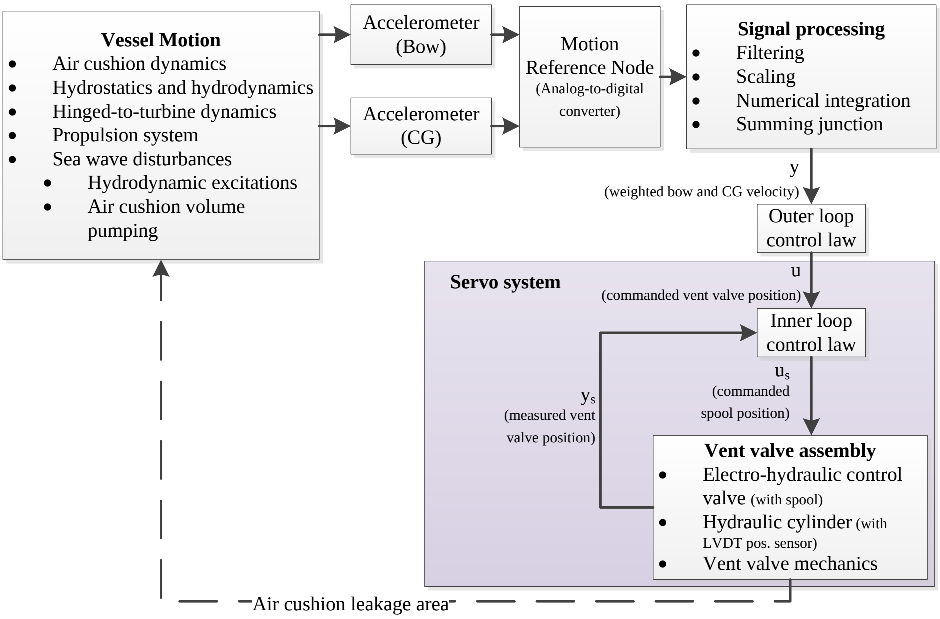
Vessel Motion
Air cushion dynamics
Hydrostatics and hydrodynamics
Hinged-to-turbine dynamics
Propulsion system
Sea wave disturbances
Hydrodynamic excitations
Air cushion volume pumping
Accelerometer (Bow)
Accelerometer (CG)
Motion Reference Node
(Analog-to-digital converter)
Signal processing
Filtering
Scaling
Numerical integration
Summing junction
y
(weighted bow and CG velocity)
Outer loop control law
Servo system
u
(commanded vent valve position)
Inner loop control law
y_s
(measured vent valve position)
u_s
(commanded spool position)
Vent valve assembly
Electro-hydraulic control valve (with spool)
Hydraulic cylinder (with LVDT pos. sensor)
Vent valve mechanics
Air cushion leakage area

Figure 3.3: Inner and outer loop control system.

Figure 3.4 shows the same illustration using a control theory block structure. Modelling and terminology of the inner loop servo system is found on Section 3.1, while the outer loop description is covered in Section 2.5.

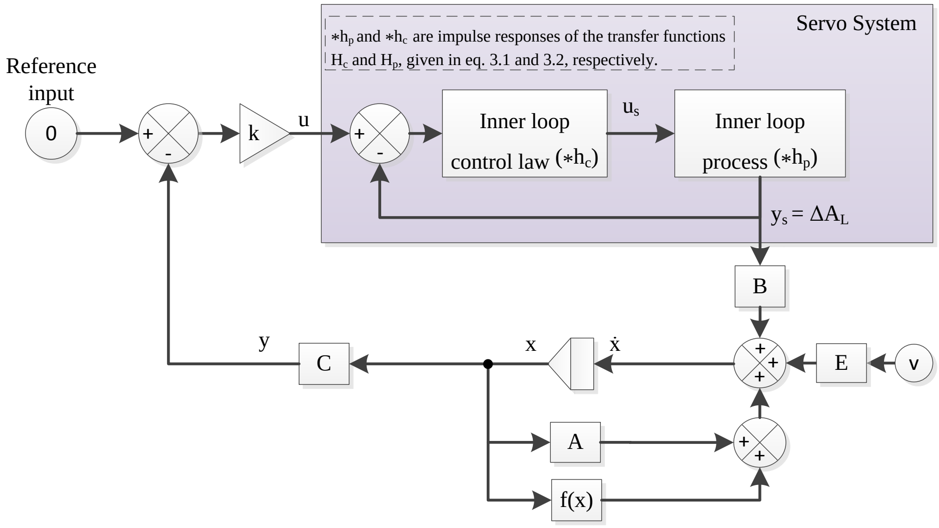
Servo System
*hp and *hc are impulse responses of the transfer functions Hc and Hp, given in eq. 3.1 and 3.2, respectively.
Reference input
0
+
-
k
u
+
-
Inner loop control law (*hc)
us
Inner loop process (*hp)
ys = ΔAL
B
y
C
x
ẋ
+
+
+
E
v
A
+
+
f(x)

Figure 3.4: A block diagram of the inner and outer loop system

3.1 Classification of the Response of a Servo System - Inner Loop

The inner-loop is regarded as a servo system. This section presents a procedure for tuning of a servo system and determine its stability margin. Several guides about tuning a servo-system are available in the literature. Parker present a highly acknowledged article in [33]. The somewhat unique contribution in this section, is to provide guidelines to determine the actual servo-response based on two logged time-series that generates a Bode plot. Some fundamental hydraulic principles are discussed.

The fundamental property of a servo system, seen from a control engineer's perspective, is the frequency response requirement. Usually, this is presented as the -3 dB corner frequency of x Hz, where x describes a certain frequency where the measured (sinusoidal) signal amplitude is $\approx 70.7\%$ of the command signal. Given a set of control parameters and one single test-run - we are able to classify the actual frequency response of the servo system from that specific test. The response is presented in such a way that it can be read directly off a Bode plot. Due to property rights, x is not given in this case study, and hence the x-axis on the plots is normalized. However, the principle of classifying the servo system and its stability margins remains the same.

The physical interpretation of this corner limit will be explained. The actuator is commanded to follow a sinusoidal signal with constant amplitude A over increasing frequencies. Hence, the command signal is a constant amplitude, frequency sweep sinusoidal signal. Now, the corner frequency x is the frequency at which the actual, measured amplitude is reduced to $0.7071A$ (-3dB). Hence, the servo system tries to reach the commanded position but the actual position does not "quite" get there in time. The frequency range $[0, x]$ Hz define the so-called control bandwidth.

This study will exclusively investigate the inner closed-loop, end-to-end performance (Fig. 3.3). In section 3.1.3, the Motion Reference Node is fed with two different command signals, first a step response - and then a frequency sweep-signal. The sweep signal response will determine the Bode plot.

The test took place at a test facility at Umoe Mandal and was conducted by the author of this thesis together with Island Engineering Inc. (IEI) personnel. The test consists of hardware and software identical to those installed onboard the Wave Craft. The opening position of the vent valves are mechanically associated with, and assumed linear with the position of a hydraulic cylinder, see Fig. 3.6.

The position of the cylinder is automatically controlled using closed loop feedback control. The Servo Node receives a commanded cylinder position and a LVDT sensor measures the actual cylinder position. A Data Acquisition (DAQ) Device (Measurement Computing, USB-3101) will feed the Motion Reference Node (Fig. 3.3) with the command signal which is an analog voltage DC signal. A logging device (Measurement Computing, BTH-1208LS) was used to store the test data.

The servo system is modelled in Section 3.1.1 while the results are covered in Section 3.1.3. The test overview is presented in Fig. 3.5 while the vent valve assembly is illustrated in Fig. 3.6.

First, in any servo-system, it is important that the structural natural frequency

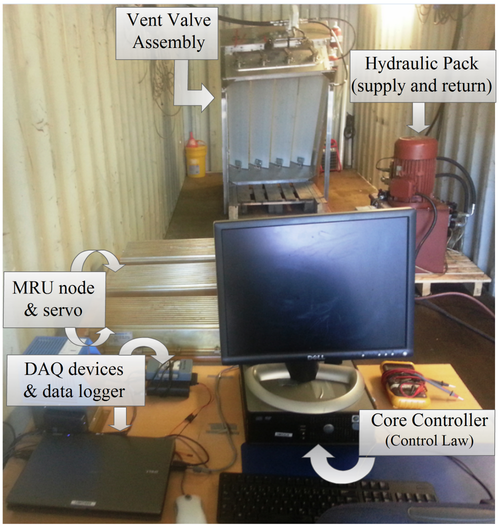
Vent Valve Assembly
Hydraulic Pack (supply and return)
MRU node & servo
DAQ devices & data logger
Core Controller (Control Law)

Figure 3.5: Test overview.

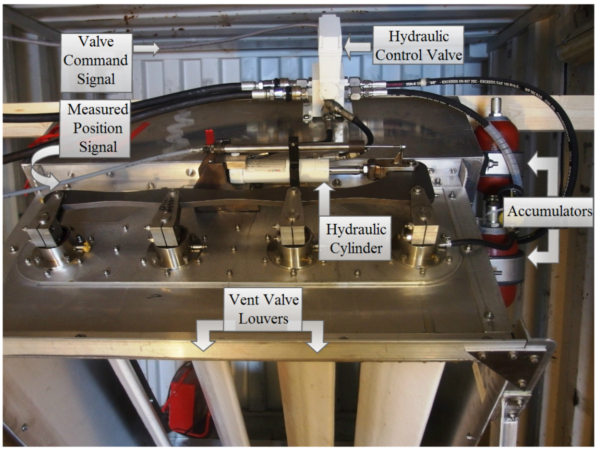
Valve Command Signal
Hydraulic Control Valve
Measured Position Signal
Accumulators
Hydraulic Cylinder
Vent Valve Louvers

Figure 3.6: Vent valve assembly.

of the moving assembly is sufficient high above the control bandwidth. The natural frequency should at least be 3 times higher than the frequency that correspond to the -3dB point of the vent valve frequency servo response (x Hz). In our case, a significant high natural frequency was successfully proven using an accelerometer mounted on the longitudinal plane of the louver blade while executing impact tests perpendicular to the blade. If any of the structural eigenfrequencies is sufficiently near the control bandwidth then the structure must be redesigned.

To understand the vent valve assembly system, the hydraulic flow is explained using Figs. 3.3 and 3.6. Assume that the vent valve louvers are initially located at 0

% opening, hence closed. Now, apply some positive command position, for instance a step up to 20 % opening. The analog control signal (Valve Command) is sent to the hydraulic-electric control-valve. In this case, the oil will flow in the following direction which will open up the louvers:

- From P (supply-side, a hydraulic pack which provides constant pressure), through the hydraulic control valve to A on the Cylinder
- From A to be B on the cylinder.
- From B on the cylinder to T (return-side, pack) through the hydraulic control valve assembly.

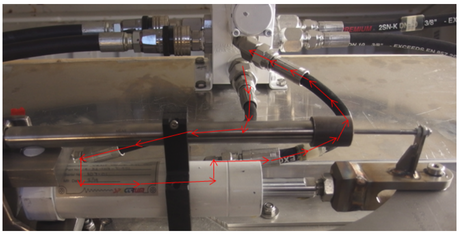

Figure 3.7: Direction of the hydraulic flow.

The direction of the flow is also illustrated in Fig. 3.7. As a side note, the effect of the accumulators is to assure a continuous hydraulic flow.

3.1.1 Modelling the servo system

For clarity, the servo-system consists of the hydraulic cylinder, a LVDT position sensor attached to the cylinder and the electric-hydraulic control valve given in Figs. 3.3 and 3.6. The notation used for this section is defined in Table 3.1.

Table 3.1: Inner loop notation

Symbol	Description
u	Command Position
y_s	Measured Position
u_s	Valve Command Signal
e_s	Error signal: u - y_s

Figure 3.8 illustrates the servo system using two transfer-function, $H_c(s)$ and $H_p(s)$ which respectively denotes the controller and the plant model. The plant

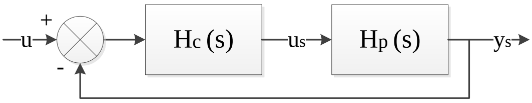

Figure 3.8: Feedback system in the frequency domain.

model, $H_p(s)$, captures the dynamics of the servo control-valve (the electric part of the Control Valve Manifold) and the cylinder. $H_p(s)$ is modelled according to [30] and and [20] which uses three basic mathematical relations: the continuity equation of the oil fluid, the pressure-flow equation of the control valve and the pressure load. The system will only be discussed in the frequency domain and it can be written on the following form, from input to output:

$$\frac{y_s}{u_s}(s) = H_p(s) = \frac{\frac{K_{sv}}{A}}{s\left(1 + 2\zeta_h \frac{s}{\omega_h} + \frac{s^2}{\omega_h^2}\right)\left(1 + \frac{s}{\omega_{sv}}\right)} \tag{3.1}$$

where u_s and y_s are described in Table 3.1 and A is the working area of the cylinder. ω_h and ζ_h denotes the natural frequency and the damping ratio of the open loop cylinder. K_{sv} and ω_{sv} are the flow gain and the cut-off frequency of the servo valve and can be found from the hydraulic valve data-sheet.

Observe that H_p has four poles (s^4-term in the denominator) and no zeroes (s^0-term in the numerator).

3.1.2 Control system design

The inner loop, or servo, controller is modelled as a PI-controller. In our application, the velocity term (D) in the servo software algorithm is not found necessary for the hydraulic servo because the requisite velocity damping is inherent in the P-Q characteristic curve of the servo-valve itself. Ideally, in most hydraulic servo applications, the I-term gain should be set to zero when the actuator is moving and set non-zero when motion has stopped to hold the stationary position without oscillation. An integral windup limit is necessary to avoid that the I-term grows too large for a temporary, or a small permanent, stationary error.

$$H_c(s) = K + \frac{K_i}{s}, \tag{3.2}$$

and

$$u_s(s) = H_c(s)\, e_s(s), \tag{3.3}$$

where K, and K_i are positive scalars which weights the proportional and integral term, respectively.

The system from input to output can be written:

$$\begin{aligned} y_s &= \left(\frac{H_p H_c}{1 + H_p H_c}\right) u \\ &:= Hu \end{aligned} \tag{3.4}$$

Model verification is presented in [30] for an identical setup, but with different coefficients which physically describes the specific servo-valve and the cylinder. Since modelling of the servo-dynamics is not the main task of this thesis, further model verifications or simulations are not given. However, we take advantage of one important thing we just discovered: using equation (3.1), (3.2), (3.4) and simple mathematics, we know that $H(s)$ got 6 zeros and 10 poles. This will be used when generating the Bode plot.

3.1.3 Tests and results

All tests presented here are end-to-end, real experiment response tests which will involve any software and hardware time delays or lag. Hence, we use the notation 'end-to-end response' which differs from a traditional servo-response test where a command signal is fed directly into the servo-valve, or the Control valve Manifold as denoted in Fig. 3.3.

All results will be shown in voltage, read directly from the DAQ logging device.

Step response - initial tuning:

In our case, a step response test is performed in order to do a somewhat coarse tuning. It is regarded valuable information before starting the frequency sweep test to ensure that the system is not unstable. Many servo applications perform the tuning solely using step responses. In our case, we are interested in a certain frequency response hence it is in the next section the fine tuning occurs.

The step response is a -1 to $+1$ [V] signal. Suitable control gains and control gain set points were found using the trial and error approach when the step response showed a satisfactory behaviour.

As expected, the test illustrated the trade-off that exists between overshooting and phase lag. By increasing K, the overshoot increased, while the phase lag decreased. A critical upper limit for K is when oscillatory response occurs at the measured position signal during a step response. If this happen, you want to decrease K. In our case, Fig. 3.9 shows a satisfactory, initial behaviour for the servo system with an overshoot of ≈ 20 %.

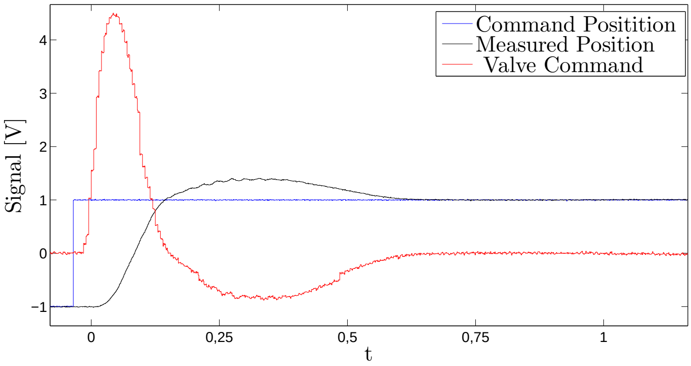

Figure 3.9: A step response is commanded on the input.

End-to-end response - frequency sweep

In this section we will force the vent valves to follow a sinusoidal wave with amplitude 1 V with increasing frequency. The frequency starts at the lowest frequency in the expected control bandwidth and ends at the highest. The total run time needs to be chosen sufficiently long so that the servo frequency response can be accurately estimated from our Bode diagram. Thus, we perform a frequency sweep and study the response between the input (Commanded Position) and the output (Measured Position) in terms of overshoot, undershoot and phase lag. This particular command signal, which is illustrated in Fig. 3.10, has an amplitude of 1V, starting with a low frequency and ends at x Hz.

$$\text{Command Position}(t) = \sin\left(2\pi f(t-t_0)\cdot(t-t_0)\right), \tag{3.5}$$

where $f(t-t_0) = \frac{1}{2}\cdot(t-t_0)$.

Another option to determine the frequency response is to run multiple sinusoids, each with one certain frequency. However, this is not the approach discussed in this work as we prefer running the whole frequency spectrum in one run which allows a quicker tuning. Figure 3.10 shows the time series of the sinusoidal frequency sweep test. Since x is not given, the ticks on the x-axis are not shown.

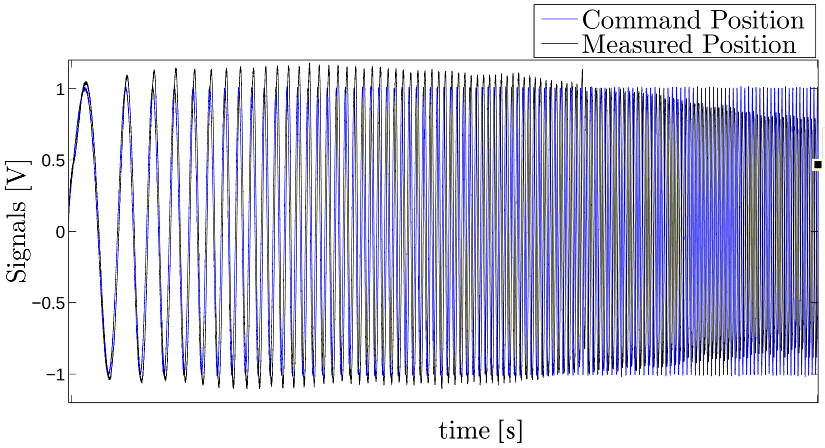

Figure 3.10: The servo system is following a 1V amplitude command signal with increasing frequency as time increases.

Figure 3.12 is an estimated frequency response using the time series in Fig. 3.10. The uncertainties of the estimated frequency response is given accordingly *Fit to estimation data: 88.01% (simulation focus), FPE: 0.007635, MSE: 0.007581.*

A simple explanation of the Bode diagram will be given. Figure 3.10 illustrates that at the lowest frequencies, the input follows the output close to perfect. If we look up these frequency in the Bode diagram, we read that the magnitude is 0.2 dB and ~0 degrees phase lag hence.

Now by studying Fig. 3.11, the highest frequency in our sweep, the measured position has some phase lag and undershoot compared to the commanded position

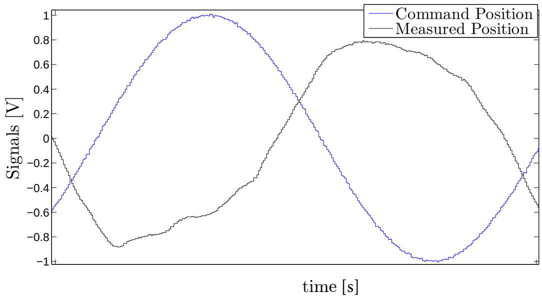

Figure 3.11: Figure 3.10 zoomed in at the end.

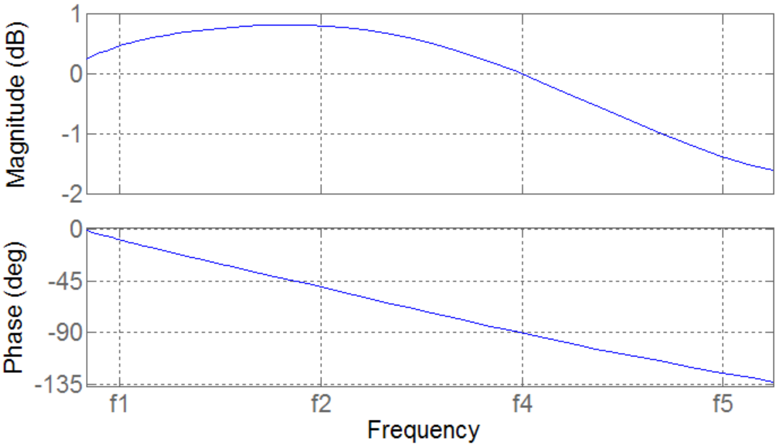

Figure 3.12: Bode Plot - illustrates the frequency response from the input (Command Pos.) to the output (Measured Pos.).

signal. We can classify these parameters by looking the highest frequency in the Bode diagram, we see that the undershoot, and the phase lag is -1.7 dB and $-133°$, respectively. The system shows satisfactory performance since Fig. 3.12 illustrates that the system is stable. The phase margin is defined as the margin to the instability limit, 180° phase limit where the amplitude crosses the 0 dB limit. Hence, the system is stable with a phase margin $180° - 91° = 89°$ and we do not even see the -3 dB limit in our control bandwidth. However, this limit can always be estimated by following the trend of the magnitude and phase curves down to -3 dB. Due to the large stability margin, the gains could be further increased but in our application the frequency response was fulfilled. Further increase of gain would increase actuator fatigue due to increased cylinder piston rod accelerations.

The magnitude figure has a resonance top around frequency $f2$. This correspond to the overshoot seen in the time series, Fig. 3.10. It is more complex to figure out what an acceptable overshoot limit is, as this depends on at least two factors: 1. How much overshoot is acceptable given the mechanical constraints of the design?

2. Is the overshoot followed by a resonant "ring" and does that raise concerns for the stability of the the servo at the fundamental resonance frequency for the design?

Figure 3.13 shows the valve command signal, hence the analog signal sent to the hydraulic-electric control valve, and the error between the measured and commanded position.

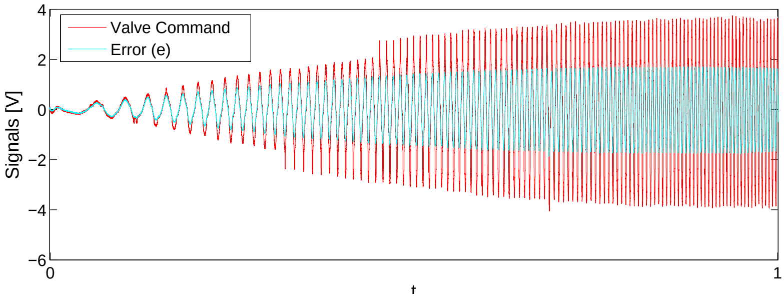

Figure 3.13: Valve Command and error signal.

The steps used in this case-study, to identify the servo response and to tune the servo system:

1. Find an initial set of controller parameters according to the step response test given in Section 3.1.3. Accept an overshoot between 10% and 20%.
2. Command a sinusoidal frequency sweep signal (y) using relevant frequencies for the control application. Choose a large run time and log u and y_s using a sample frequency of at least six times the largest frequency tested in the sweep.
3. Matlab code to generate Bode plot:

```
% We assume the logged time series vectors t (time),
% u and y_s are available in the workspace.
Ts = t(2)-t(1);
data = iddata(y_s,u,Ts);
np = 10; % Number of poles in H(s)
nz = 6; % Number of zeroes in H(s)
sys = tfest(data,np,nz);
% f_min and f_max denotes min and max frequency of,
% the chosen frequency sweep signal:
w = {2*pi*f_min,2*pi*f_max};
bode(sys,w)
```

4. If the frequency response is not satisfactory, adjust the controller gain accordingly (as explained in Section 3.1.3), and start again at 2.

3.2 The Boarding Control System - Outer Loop

This section includes the performance of the BCS on the Wave Craft prototype, the Umoe Ventus as seen in Fig. 3.14. The results are normalized for the purpose of generality. It is the motion reduction ratio of the BCS that is the main interest of this work.

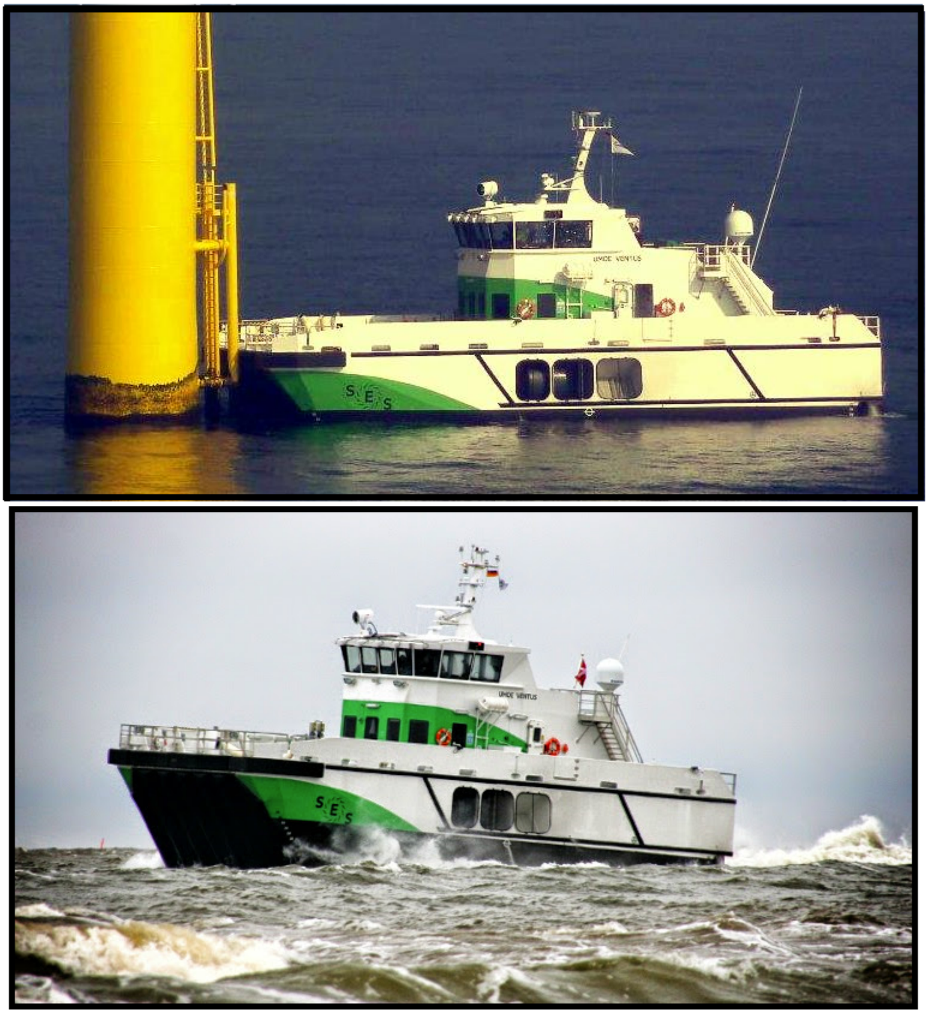

Figure 3.14: Top: Umoe Ventus in boarding mode towards a wind turbine by courtesy of Dong Energy. Bottom: Umoe Ventus in transit towards the wind farm by courtesy of vesseltracker.com.

3.2.1 No turbine contact

The following test, was conducted outside Mandal in February 2015 at zero forward speed, in irregular seas with wave period $T_p \approx 4 - 5$s and significant wave height $H_s = \approx 1.6$ m.

Figure 3.15 illustrates the time series during the test while Fig. 3.16 shows the power spectral density plot from the same run and compares the bow acceleration before and after the BCS is switched off. For the PSD plot, BCS was toggled active and inactive, each with an interval of 269 seconds. From this figure it is clear that bow tip vertical acceleration and pitch motion are reduced. The higher frequencies observed on Fig. 3.15 are typical on a SES due to the cushion dynamics but are way above the control bandwidth and hence no interest for the BCS.

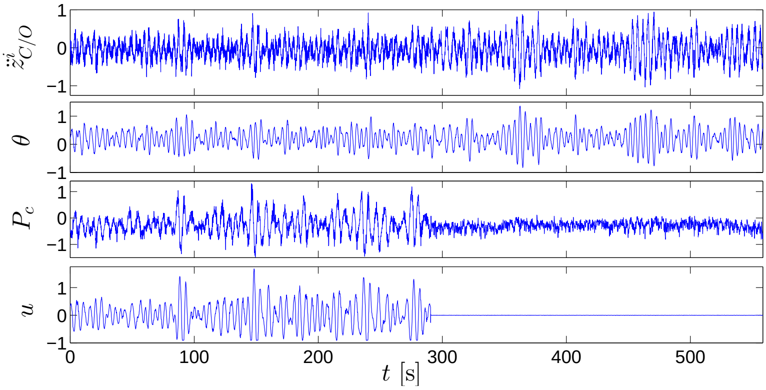

Figure 3.15: Time series plot of the bow acceleration. The BCS is initially on and turned off at $t = 290$s.

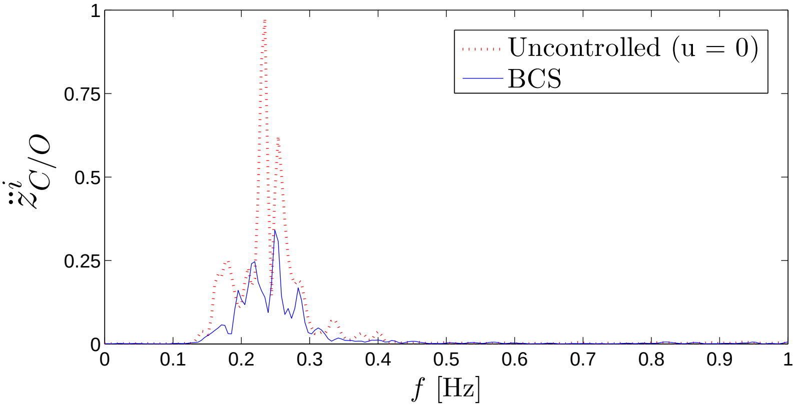

Figure 3.16: PSD plot of the bow acceleration with, and without, the BCS active.

The following test took place on the wind-farm Borkum Riffgrund 1, March,

2015. The test was taken an hour after the results given in the journal paper in Section 2.5. The sea waves are larger at this point which leads to an increase in vertical motion, both when the BCS is active, and not active. The wave period remained approximately the same. The largest sea waves were estimated up to 3.5 meter, hence the estimated significant wave height (H_s) is somewhere around, or slightly below 2m. The wave period (T_s) is $4-5$s. Figure 3.17 shows the time series, indicating the performance of the BCS in this sea condition. The plot shows, from top to bottom, vertical accelerations, pitch, controller output and cushion pressure.

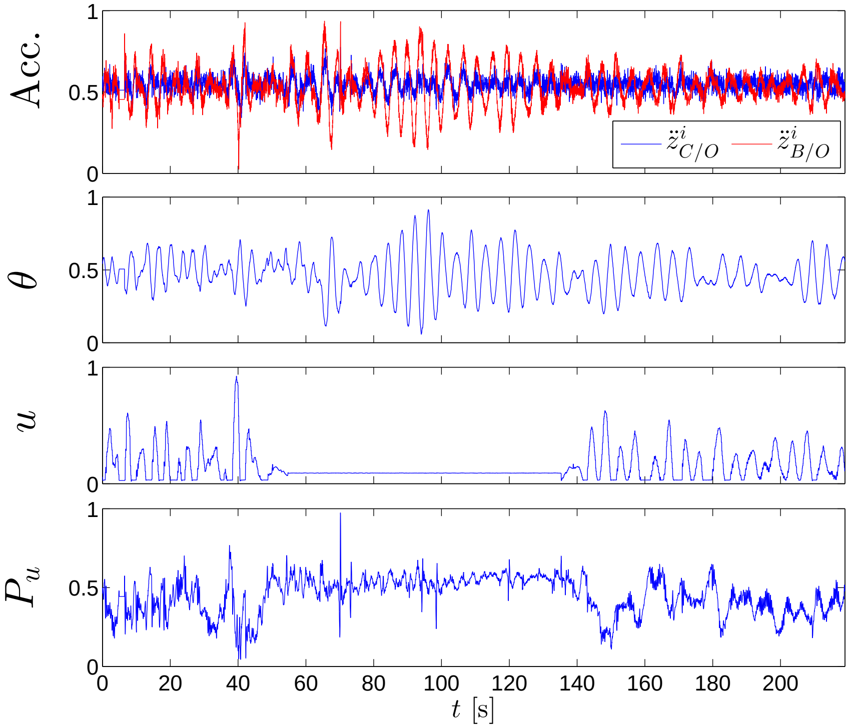

Figure 3.17: Time series with and without ($t = \{53, 1356\}$s) the BCS active.

Figures 3.18 and 3.19 show the PSD figure for bow and CG accelerations using the time series above. The data gathered for the uncontrolled case is taken for when $t = \{53, 136\}$s while $t = \{136, 219\}$s represent the time period for when the BCS is on.

Figures 3.18 and 3.19 were created using the Matlab function pwelch. Due to a sampling frequency on 32.16 Hz, each signal length is 2670 samples. The chosen FFT segment is set to 1025 samples with 25 % overlap. A Hamming window with the same length as the segments was used.

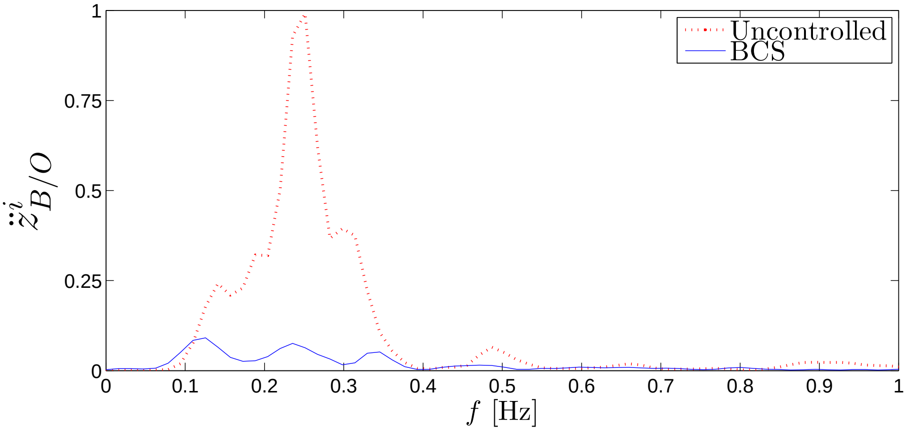

Figure 3.18: Bow acceleration PSD plot with, and without, the BCS active.

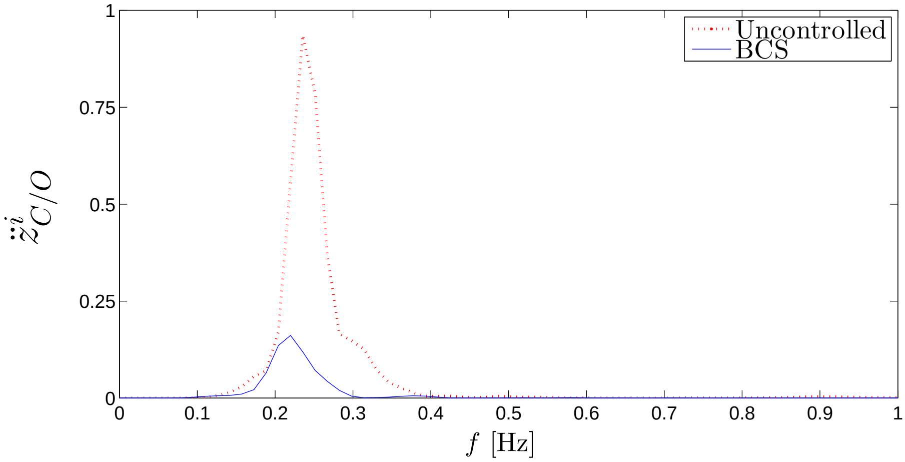

Figure 3.19: CG acceleration PSD plot with, and without, the BCS active.

Chapter 4

Conclusions and Recommendations for Future Work

4.1 Conclusions

No bow-to-turbine contact (free-floating motion)

When bow-to-turbine contact is not present, the results prove great motion damping at the bow tip for all sea headings. In fact, our model-test results shows up to 60% and 68% less motion compared to the uncontrolled case in head and following seas, respectively. See Figs. 4 - 12 in Conference paper 3, Section 2.3.

Our full-scale measurements have proved higher performance than what expected based on simulation and model-test craft. One of the reason for this is probably that the air flow friction, from the air cushion and out to ambient pressure, was smaller than anticipated. In simulation, a flow coefficient (c_n) of 0.61 was used, this was probably a very conservative value. Also, the model-test vessel had a non-linear butterfly valve with a 60 degree bent duct (to avoid water spray in the model-tank). The model-test rubber bow fender was dimensionally scaled, but not density scaled. The fender fabric, and therefore the rubber density, was identical for the model and full-scale tests. Hence, the model-test results presents conservative performance due to a somewhat 'too stiff fender'. These are all factors that are directly coupled with the control system performance.

Our full-scale experience and performance have proven that the Wave Craft prototype captains are fully dependent on the BCS-mode when approaching, and manoeuvring towards, a wind-turbine in larger seas. Previous stated quotes given in Section 3 illustrates that wind-turbine service personnel are very satisfied with the performance of the system, and surprised by the small vessel motions relative to the sea state.

Bow-to-turbine contact

The tests towards turbine have confirmed the capabilities of the vessel. Control of the air cushion pressure is indeed capable of improving the operational window compared to the uncontrolled case. For regular waves, model-tests proved that the control system can maintain and ensure that the bow fender that sticks to the turbine in up to 3.2m wave height. For model-test results in irregular seas, it is somewhat harder to decide a safe wave condition limit for turbine-transfer. Mainly since such a limit relies on statistics that are not available: for instance, how many and how large vertical bow slips are regarded safe during a fixed time period? This is discussed further in Section 2.5 and concludes, using model test data, that boarding a turbine up to 2.5m significant wave height (H_s) is regarded as safe.

The full-scale prototype, Umoe Ventus, proved that the damping effect of the BCS was close to 80% (Fig. 18 in Section 2.5). There was hardly any motions on the vessel when the BCS was turned ON. In-fact, the system was not near its maximum operational wave limit. To this date, the vessel has only been tested up to 2m H_s with zero slips from the wind turbine. Two factors have limited the full-scale craft to try and access turbines in 2m+ H_s:

- No turbine-vessel can operate in the wind-park alone. At least two vessels are required. Currently, only one SES with the BCS exists.
- Horizontal forces such as wind and current, highly affects the ability to access a turbine. The horizontal forces, which are not observable or controllable by the BCS, are a often a bigger issue than the vertical motion when the BCS is on.

In order to truly quantify the performance of the BCS in full-scale, the effects listed above cannot be present and therefore further testing would be required. However, the results given here shows that there are hardly any heave or pitch motion in seas around $1.5-1.8$m H_s, which is after all, close to the current operational wave limit of conventional turbine vessels [2].

4.2 Future work

Auestad et al. [11] wrote and presented a paper in the time between the article content of this thesis was set and when it was printed. This work is focusing further on the full-scale testing, digital signal processing and system identification techniques.

Future work could include automatic switching between different physical sensors distributed in the longitudinal direction of the craft. The results presented in this thesis indicates that when contact does not exist between the turbine and craft, the sensor should be located at the vessel bow for increasing damping of bow motion. When contact exists the sensor should be located around CG. The approach presented in Section 2.5 deals with a fixed, weighted ratio between the two sensors.

An approach to supplement the result in this thesis could involve different control strategies such as linear quadratic control, model predictive control, sliding mode control or hybrid control which could switch model or controller based on the current type of friction (static or kinetic).

In general, more investigations should be conducted in order to fully understand and optimize control of wave-frequency motions on a SES. This includes hull structure, modelling, experimental testing, control system design, choice of sensor(s) types, etc.

Station keeping in the horizontal domain using DP systems have attracted a lot of attention in the literature the past decades with very impressing results, leading to huge industrial manufacture-deals world-wide. The author of this thesis is convinced that control of a SES has an enormous, unused potential. The marine industry keeps moving further offshore, facing rougher sea conditions which leads to challenges regarding sea-sickness and safety for personnel, equipment and vessel [2].

Appendices

Appendix A

Wave Craft Main Characteristics

In general, the hull shape is similar to a SWATH (Small Waterplane Area Twin Hull), with very narrow side hulls and a small water plane area. A one-pager of the Wave Craft is given in Fig. A.1.

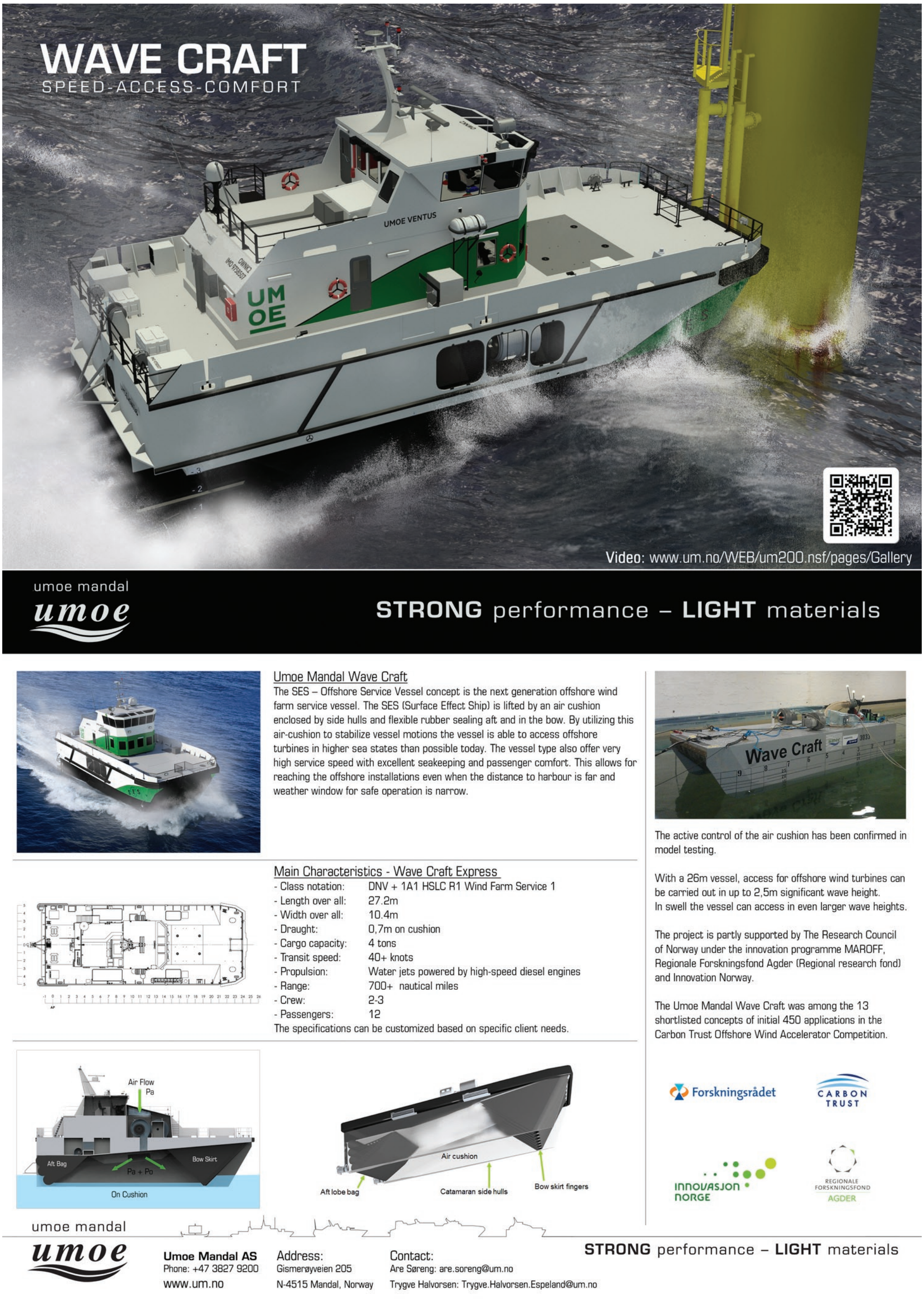
WAVE CRAFT
SPEED-ACCESS-COMFORT
UMOE VENTUS
UM OE
Video: www.um.no/WEB/um200.nsf/pages/Gallery
umoe mandal
umoe
STRONG performance – LIGHT materials
Wave Craft
Air Flow
Pa
Aft Bag
Bow Skirt
Pa + Po
On Cushion
Air cushion
Aft lobe bag
Catamaran side hulls
Bow skirt fingers
Forskningsrådet
CARBON TRUST
INNOVASJON NORGE
REGIONALE FORSKNINGSFOND AGDER
umoe mandal
umoe
STRONG performance – LIGHT materials

Umoe Mandal Wave Craft

The SES – Offshore Service Vessel concept is the next generation offshore wind farm service vessel. The SES (Surface Effect Ship) is lifted by an air cushion enclosed by side hulls and flexible rubber sealing aft and in the bow. By utilizing this air-cushion to stabilize vessel motions the vessel is able to access offshore turbines in higher sea states than possible today. The vessel type also offer very high service speed with excellent seakeeping and passenger comfort. This allows for reaching the offshore installations even when the distance to harbour is far and weather window for safe operation is narrow.

Main Characteristics - Wave Craft Express

- Class notation:	DNV + 1A1 HSLC R1 Wind Farm Service 1
- Length over all:	27.2m
- Width over all:	10.4m
- Draught:	0,7m on cushion
- Cargo capacity:	4 tons
- Transit speed:	40+ knots
- Propulsion:	Water jets powered by high-speed diesel engines
- Range:	700+ nautical miles
- Crew:	2-3
- Passengers:	12

The specifications can be customized based on specific client needs.

The active control of the air cushion has been confirmed in model testing.

With a 26m vessel, access for offshore wind turbines can be carried out in up to 2,5m significant wave height.
In swell the vessel can access in even larger wave heights.

The project is partly supported by The Research Council of Norway under the innovation programme MAROFF, Regionale Forskningsfond Agder (Regional research fond) and Innovation Norway.

The Umoe Mandal Wave Craft was among the 13 shortlisted concepts of initial 450 applications in the Carbon Trust Offshore Wind Accelerator Competition.

Umoe Mandal AS
Phone: +47 3827 9200
www.um.no

Address:
Gismerøyveien 205
N-4515 Mandal, Norway

Contact:
Are Søreng: are.soreng@um.no
Trygve Halvorsen: Trygve.Halvorsen.Espeland@um.no

Figure A.1: One-pager - UM Wave Craft

Appendix B

Proof of Remark 1, in Conference Paper 3 (IFAC, World Congress)

The goal of this section is to provide a restriction on the disturbance- or perturbation -vector v so that the system in Eq. B.1 has a global exponential stable equilibrium point.

The perturbed, closed loop system can be written:

$$\dot{x}(t) = A_{cl}x(t) + Ev(t) \tag{B.1}$$

Remember our Lyapunov candidate, $V(t)$, using P as previously calculated

$$V(t) = x^T(t)Px(t), \tag{B.2}$$

When differentiating along the system trajectories we use P and Q as defined earlier, however, in contrast to earlier, we are now including the perturbation term, hence $v(t) \neq 0$:

$$\begin{aligned}\dot{V}(t) &= -x(t)^T Qx(t) + 2x(t)^T PEv(t) \\ &= 2\left(\frac{\rho_{c0}\dot{V}_0\mu_u - K_3\mu_u^2}{K_1} + K_5\frac{F_3^e\dot{\eta}_3 - B_{33}\dot{\eta}_3^2}{A_cP_0} + K_4\frac{F_5^e\dot{\eta}_5 - B_{55}\dot{\eta}_5^2}{A_cP_0x_{cp}(A_{55} + I_{55}}\right)\end{aligned} \tag{B.3}$$

where $K_4 = A_c\rho_{c0}x_{cp} + \frac{K_2L_bk}{K_1}$, $K_5 = \frac{A_c\rho_{c0}+K_2k}{K_1}$ and remembering that all the algebraic terms in A_{cl} and E are positive due to their physical interpretation. Recall that the state and disturbance vector is written

$$x(t) = [\eta_3 \;\; \eta_5 \;\; \dot{\eta}_3 \;\; \dot{\eta}_5 \;\; \mu_u]^T_, \qquad v(t) = \left[F_3^e \;\; F_5^e \;\; \dot{V}_0\right]^T. \tag{B.4}$$

We know that $V > 0$ since $P > 0$. What remains to be shown is that $\dot{V} < 0 \quad \forall x$ given some criteria on the disturbance vector v.

To show this, we go through the three terms in (B.3) to make sure they are all, individually, strictly negative given a restriction on v.

For the first term in (B.3), we require

$$\rho_{c0}\dot{V}_0\mu_u - K_3\mu_u^2 < 0 \quad \Rightarrow \quad \rho_{c0}\dot{V}_0\mu_u < K_3\mu_u^2 \tag{B.5}$$

By studying the left-hand side of the inequality (B.5) and using Hölders inequality we can write $\rho_{c0}\dot{V}_0\mu_u \leq \rho_{c0}|\dot{V}_0\mu_u| \leq \rho_{c0}|\dot{V}_0||\mu_u|$. By studying the right-hand side of (B.5) we write $K_3\mu_u^2 = K_3|\mu_u|^2$. Hence,

$$\begin{aligned} \rho_{c0}|\dot{V}_0||\mu_u| &< K_3|\mu_u|^2 \\ \rho_{c0}|\dot{V}_0| &< K_3|\mu_u| \\ &\Downarrow \\ |\dot{V}_0| &< \frac{K_3}{\rho_{c0}}|\mu_u| \end{aligned} \tag{B.6}$$

Using the same procedures for the two remaining terms in (B.3) we get:

$$|F_3^e| < B_{33}|\dot{\eta}_3|, \quad |F_5^e| < B_{55}|\dot{\eta}_5| \tag{B.7}$$

By using the superposition principle, we can combine the inequalities from (B.6) and (B.7) and write:

$$|F_3^e| + |F_5^e| + |\dot{V}_0| < B_{33}|\dot{\eta}_3| + B_{55}|\dot{\eta}_5| + \frac{K_3}{\rho_{c0}}|\mu_u| \tag{B.8}$$

Using the $||x||_1$ norm we can write this on vector form:

$$||v|| < ||Tx|| \tag{B.9}$$

where $T = \begin{bmatrix} 0 & 0 & B_{33} & 0 & 0 \\ 0 & 0 & 0 & B_{55} & 0 \\ 0 & 0 & 0 & 0 & \frac{K_3}{\rho_{c0}} \end{bmatrix}$

Also note that by increasing the controller gain k in (B.3), we increase the system damping by making $\dot{V}$ even more negative, given the restriction on $||v||$ in (B.9). Finally, if the disturbance vector v is restricted according to equation B.9, then the equilibrium x_0 is GES.

References

[1] Iso 2631-1:1997 mechanical vibration and shock evaluation of human exposure to whole body vibration. International Standards Organization, Switzerland, 1997.

[2] Carbon trust's offshore wind accelerator (owa) access competition - overview and technical specification, 2010. URL http://www.engr.mun.ca/~bveitch/courses/IntroNavArch/Assignments/SOR%20-%20OWA.pdf.

[3] Carbon trust's offshore wind accelerator access competition - short-listed designs, 2015. URL https://www.carbontrust.com/media/105306/owa-access-innovators.pdf.

[4] Carbon trust's offshore wind accelerator program, 2015. URL http://www.carbontrust.com/our-clients/o/offshore-wind-accelerator/.

[5] J. D. Adams, A. W. Ernest, and J. Lewis. *Design, Development and Testing of a Ride Control System for the XR-ID Surface Effect Ship; Part I - Classical Control*. Report No. MD-AR-1180-1. Maritime Dynamics, Inc., Tacoma, Washington, 98422., 1983.

[6] Ø. Auestad. Heave control system for a surface effect ship: Disturbance damping of wave induced motion at zero vessel speed. Master's thesis, Department of Engineering Cybernetics, NTNU, 2012.

[7] Ø. F. Auestad, J. T. Gravdahl, and T. I. Fossen. Heave motion estimation on a craft using a strapdown inertial measurement unit. In *Proceedings of the 9th IFAC Conference on Control Applications in Marine System*, Osaka, Japan, September 17-20, 2013.

[8] Ø. F. Auestad, J. T. Gravdahl, A. J. Sørensen, and T. H. Espeland. Simulator and control system design for a free floating surface effect ship at zero vessel speed. In *Proceedings of the 8th IFAC Symposium on Intelligent Autonomous Vehicle*, Gold Coast, Australia, 26-28 June, 2013.

[9] Ø. F. Auestad, J. T. Gravdahl, A. J. Sørensen, and T. H. Espeland. Motion compensation system for a free floating surface effect ship. In *Proceedings of the 19th World Congress of the International Federation of Automatic Control, IFAC*, Cape Town, South Africa, August 24-29, 2014.

[10] Ø. F. Auestad, J. T. Gravdahl, T. Perez, A. J. Sørensen, and T. H. Espeland. Boarding control system - for improved accessibility to offshore wind turbines: Full-scale testing. *Accepted in Control Engineering Practise*, 2015.

[11] Ø. F. Auestad, B. McFann, and J. T. Gravdahl. Full-scale performance of the ses motion control system. In *Proceedings of the 13th International Conference on Fast Sea Transportation (FAST)*, Washington, USA, September 1-4, 2015.

[12] Ø. F. Auestad, T. Perez, J. T. Gravdahl, A. J. Sørensen, and T. H. Espeland. Boarding control system - for improved accessibility to offshore wind turbines. In *Proceedings of the 10th IFAC Conference on Manoeuvring and Control of Marine Craft (MCMC), IFAC*, Copenhagen, Denmark, August 24-26, 2015.

[13] H. I. Basturk and M. Krstic. Adaptive wave cancelation by acceleration feedback for ramp-connected air cushion-actuated surface effect ships. *Automatica*, 49(9):2591–2602, 2013.

[14] D. Bertin, S. Bittanti, and S. M. Savaresi. Decoupled cushion control in ride control systems for air cushion catamarans. *Control Engineering Practice*, 8 (2):191–203, 2000.

[15] R. D. Blevins. *Applied Fluid Dynamics Handbook*. Krieger Publishing Company, 2003.

[16] E. A. Butler. The surface effect ship. *Naval Engineers Journal*, 97(2):200–258, February 1985.

[17] J. Chaplin. Bell halter surface effect ship development. In *Proceedings of the AIAA 6th Marine Systems Conference*, 1981.

[18] D. J. Clark, W. M. Ellsworth, and J. R. Meyer. The quest for speed at sea, April 2004. URL `http://www.foils.org/02_Papers%20dnloads/041115NSWCTD_QuestSpeed.pdf`.

[19] L. Doctors. Near-field hydrodynamics of a surface-effect ship. *Journal Of Ship Research*, 56(3):183–196, 2012.

[20] O. Egeland and J. T. Gravdahl. *Modeling and simulation for automatic control*. Marine Cybernetics, 2002.

[21] T. H. Espeland, N. Skomedal, J. Røyland, A. Pedersen, and E. Jullumstrø. Hinged ship to ship connection for at sea cargo transfer. In *Proceedings of the 11th International Conference on Fast Sea Transportation FAST*, Honolulu, Hawaii, USA, 2011.

[22] EWEA. The european offshore wind industry - key trends and statistics 2014. Technical report, European Wind Energy Association, January 2015.

[23] EWEA. The european offshore wind industry - key trends and statistics 1st half 2015. Technical report, European Wind Energy Association, July 2015.

[24] O. M. Faltinsen. *Hydrodynamics of high-speed marine vehicles, Ch. 5, p. 71-84*. Cambridge University Press, 2005.

[25] T. I. Fossen. *Handbook of Marine Craft Hydrodynamics and Motion Control*. John Wiley & Sons, Ltd, UK, 2011.

[26] P. Kaplan and S. Davies. System analysis techniques for designing ride control system for ses craft in waves. *5th Ship Contr. Syst. Symp. Annapolis, MD*, 1978.

[27] P. B. Kaplan, Bentson, and S. Davis. *Dynamics and Hydrodynamics of Surface Effect Ships*. SNAMET Transaction Volume 89, 1981.

[28] D. Lavis. Forty-plus years of hovercraft development. In *Proceedings of the 25th, Canadian Air Cushion Technology Society: CACTS '98*. Canadian Aeronautics and Space Institute, 1998.

[29] D. R. Lavis and K. B. Spaulding. Surface effect ship (ses) developments worldwid. *Naval Engineers Journal*, 103:39–83, 1991.

[30] L. Li and T. Thurner. Accurate modeling and identification of servo-hydraulic cylinder systems in multi-axial test applications. *Ventil*, 19(6):462–470, 2013.

[31] A. Malakhoff and S. Davis. Dynamics of the ses bow fingers. In *Proceedings of the AIAA 6th Marine Systems Conference*, September 1981.

[32] W. Musial and B. Ram. *Large-Scale Offshore Wind Power in the United States, p. 116-117*. National Renewable Energy Laboratory, 2010.

[33] Parker. Servo tuning. *6270 Motion Controller User Guide*, Revision B:29–56, 1995.

[34] A. J. Sørensen and O. Egeland. Design of ride control system for surface effect ships using dissipative control. *Automatica*, 31:183 – 199, 1995.

[35] A. J. Sørensen, S. Steen, and O. Faltinsen. Ses dynamics in the vertical plane. *Ship Technology Research, the Journal for Research in Shipbuilding and Related Subjects*, 40, 1993.

[36] P. S. Sodeland. Combined dynamic positioning and optimal motion damping on surface effect ship. Master's thesis, Department of Marine Technology, NTNU, 2015.

[37] S. Steen. *Cobblestone Effects on SES*. Ph.d. thesis at Dept. Marine Hydrodynamics, NTNU, 1993.

[38] R. van de Pieterman, H. Braam, T. Obdam, L. Rademakers, and T. van der Zee. Optimisation of maintenance strategies for offshore wind farms. In *Proceedings of The Offshore 2011 conference*, Amsterdam, The Netherlands, 29 November - 1 December, 2011.